Hybrid Solar Cells

Dissertation

zur Erlangung des akademischen Grades

doctor rerum naturalium (Dr. rer. nat.)

vorgelegt dem Rat der Physikalisch-Astronomischen Fakultät

der Friedrich-Schiller-Universität Jena

seit 1558

von Dipl.-Phys. Michael Kozlik

geboren am 10. August 1984 in Gera

Abstract

Solar cells "as an alternative energy source" are, more than ever, the focus of research and development. Currently, all commercial modules are based on classical semiconductor materials such as silicon. Silicon is available in very high purity and as single crystalline material, resulting in very good material properties. Extraction and purification are very cost-intensive and energy-consuming. In contrast, especially silicon, compared to organic dyes, features a very low absorption coefficient. Therefore, by the use of organic semiconductors, the thickness of solar cells can be drastically reduced. Besides thin films, simple deposition techniques are expected to significantly lower manufacturing costs. Due to other transport mechanisms (hopping transport) organic semiconductors show a significant lower charge carrier mobility compared to inorganic semiconductors (band transport). Moreover, after photon absorption in organic solar cells, separation of the still bound charge carriers (excitons) is needed.

The combination of organic and inorganic semiconductors in photovoltaics is called hybrid solar cells. This is done to make use of the high absorption coefficient of the organic material and good transport properties of the inorganic counterpart. So far, mainly polymers are used. Little experience exists in the combination of inorganic semiconductors and small molecules with aromatic rings. Latter show good optical properties. This was demonstrated in the present work using zinc(II)-phthalocyanine (ZnPc). Optical spectroscopy was used to determine the optical constants, film thickness, and roughness of the layers simultaneously.

An organic-inorganic interface within a hybrid solar cell was fabricated and characterized using ZnPc and zinc oxide. The band structure within the device was derived from photoelectron spectroscopy. Hereby, the open circuit voltage was estimated and compared to current-voltage characteristics. The curves exhibit a very low photocurrent. The reason seems to be an insufficient exciton dissociation. For this purpose two improvements were implemented. On the one hand, the band structure was modified by doping to increase the energy which is provided to overcome the binding of the excitons. On the other hand, nanowires were integrated to decrease the distance to the p-n-junction which causes the dissociation. Using spectrally resolved photocurrent measurements the exciton diffusion length could be determined to be 16 nm. However, an increase in efficiency could not be achieved.

Kurzfassung

Solarzellen sind als "alternative Energiequelle" mehr denn je im Fokus von Forschung und Entwicklung. Derzeit basieren praktisch alle kommerziell erhältlichen Module auf klassischen Halbleitermaterialien wie Silizium. Dieses ist in sehr hoher Reinheit und einkristallin verfügbar, woraus sehr gute Materialeigenschaften resultieren. Gewinnung und Reinigung sind allerdings sehr kostenintensiv und energieaufwendig. Insbesondere weist Silizium, im Vergleich zu Farbstoffmolekülen, einen sehr geringen Absorptionskoeffizienten auf. Durch Verwendung von organischen Halbleitern kann daher u.a. die Schichtdicke von Solarzellen drastisch reduziert werden. Neben dünnen Schichten verspricht man sich von günstiger Prozessierung erheblich niedrigere Herstellungskosten. Aufgrund anderer Transportmechanismen (Hopping-Transport) zeigen organische Halbleiter eine erheblich niedrigere Ladungsträgermobilität als anorganische Halbleiter (Bandtransport). Zudem ist in organischen Solarzellen nach der Photonenabsorption eine Trennung der noch gebundenen Ladungträger (Exzitonen) nötig.

Die Kombination aus organischen und anorganischen Halbleitern für die Photovoltaik wird Hybrid-Solarzellen genannt. Hiervon verspricht man sich die Nutzung der hohen Absorbanz des organischen Materials und der guten Transporteigenschaften der verwendeten anorganischen Halbleiter. Bislang kamen hauptsächlich Polymere zum Einsatz. Wenig Erfahrung gibt es hingegen in der Kombination von anorganischen Halbleitern und kleinen Molekülen mit aromatischen Ringen. Diese zeigen gute optische Eigenschaften. Dies wurde in der vorliegenden Arbeit am Beispiel von Zink(II)-Phthalocyanin (ZnPc) nachgewiesen. Optische Spektroskopie wurde verwendet, um die optischen Konstanten, Schichtdicke und Rauigkeit der Schichten simultan zu bestimmen.

Eine organisch-anorganische Grenzfläche innerhalb einer Hybrid-Solarzelle wurde aus ZnPc und Zinkoxid hergestellt und charakterisiert. Hierfür wurde mittels Photelektronenspektroskopie der Verlauf der Bandstruktur innerhalb des Bauelemtes nachvollzogen. Mit Hilfe dieser Methode wurden Abschätzungen für die Leerlaufspannung getroffen und anhand von Strom-Spannungs-Kennlinien überprüft. Die Kennlinien weisen einen sehr geringen Photostrom auf. Die Ursache dafür scheint eine schlechte Exzitonendissoziation zu sein. Hierfür wurden zwei Verbesserungsansätze gewählt. Zum einen wurde die Bandstruktur mittels Dotierung modifiziert, um die Energie zu erhöhen, welche für die Exzitonentrennung zur Verfügung steht. Zum anderen sollte durch Nanodrähte die Distanz zum dissoziationsverursachenden p-n-Übergang verringert werden, um so in die Reichweite der Exzitonen zu gelangen. Anhand von spektral aufgelösten Photostrommessungen konnte die Exzitonendiffusionslänge auf 16 nm bestimmt werden. Eine Steigerung der Effizienz wurde leider nicht erzielt.

CONTENTS

Chapter 1

INTRODUCTION AND MOTIVATION

The origin of solar cells goes back to the photoelectric effect. It was discovered in 1839 by Alexandre Edmond Becquerel. The explanation was developed much later. It starts in 1904 with the explanation of the photovoltaic effect by Philipp Lenard and was extended by Albert Einstein in 1905 with the photoelectric effect. The first solar cell was made of selenium at the end of the 19th century [1]. After discovering the p-n-junction [2] the first common inorganic solar cells were developed at Bell Labs. In 1953 arsenide doped silicon solar cells made by Daryl Chapin, Calvin Souther Fuller, and Gerald Pearson reached an efficiency of 4%. Comparable to the current situation, the economic development led to shortages in energetic supply in 1974. Because of the huge increase of the oil price, U. S. president R. Nixon rose a research project concerning renewable energies. The efficiency could be raised via higher purity and better doping possibilities. For this reason also the costs increased. This was the beginning of the second generation of solar cells, whose aim was to improve the price-performance ratio. This could be achieved by a smaller amount of material which was realized by the so called thin film solar cells. Possible candidates were cadmium sulfide or telluride, copper indium diselenide and amorphous or thin-film silicon [3]. The new problem was that not only the costs but also the performance dropped down. Single crystal silicon solar cell performance is well known to be limited by the Shockley-Queisser-limit of around 30% [4]. Hence the third generation emerged, with the aim to have a low price but a similar high performance. Concentrators, tandem, stacked organic, and even the so-called hybrid solar cells are counted to this new generation photovoltaics. "Hybrid" usually refers to the combination of different material classes with the goal to use the advantages of both and to reduce the negative aspects. In this thesis hybrid solar cells are made of organic and inorganic compounds to use the high absorption of organic molecules and the high conductivity of inorganic semiconductors. This spin off topic is represented by various fields (e.g., Grätzel cells, bulk heterojunction). The outline of this thesis follows the physical

processes of a solar cell step by step, starting from the incoming light to the final charge carriers giving rise to the photocurrent.

- After the first introduction chapter, in the second chapter some fundamental terms will be explained like the electronic structure along with associated physical parameters, interface effects, and also the "particle" exciton will be introduced. The main parameters of a solar cell are presented together with their role in I-V-characteristics. In the third chapter experimental details are provided.

- In the fourth chapter the absorption of visible light is investigated in detail. Different phases of the organic molecule are characterized by optical spectroscopy. Reflectance and transmittance are used to determine fundamental parameters like optical constants, layer thickness, and roughness.

- In the fifth chapter excitons which were generated by the absorption of the photons are analyzed. Hence, the spectral photocurrent is used. The location of exciton generation, the length of diffusion, and the dissociation are basic parameters influencing the solar cell performance. A way of extraction of these parameters from the spectral photocurrent is presented.

- The dissociation of excitons, linked with the electronic structure, and the resulting free charge carriers, linked to the photocurrent, will be characterized in chapter six and seven, respectively. A prediction of the potential of the free charge carriers which can be correlated with the open circuit voltage will be given and compared to the measured one.

To this effect this thesis should not be seen as driven by efficiency improving but more by a general understanding of the processes in the device and at organic-inorganic semiconductor interfaces which still lack a profound comprehension.

Chapter 2

BASICS

The aim of this chapter is to define a uniform vocabulary for parameters which are used in this thesis. Fundamental models will also be introduced. Especially the interfaces of different classes of solids shall be attended to, and a general overview of solar cells and their characteristics will be given motivating this study.

2.1 Electronic Structure

Contrary to the origin of the word, atoms (Greek: *atomos*; "indivisible") can be broken down into several components. In the inner core, which in the following plays a subordinate role, there are protons and neutrons, and in the outer shells are electrons. In solid states many atoms are packed closely together which lead to interaction of the electronic states. The allowed states are expressed in terms of energy and called electronic structure.

2.1.1 General Models and Nomenclature

Electronic states E_n of atoms can be calculated in first approximation by the hydrogen model.

$$E_n = \frac{m_0 e^4}{8\varepsilon_0^2 h^2} \frac{Z^2}{n^2} = -13.6 eV \cdot \frac{Z^2}{n^2} \tag{2.1-i}$$

In this simplification, the energy of state n depends on a few constants (mass m_0, elementary charge e, atomic number Z, dielectric constant ε_0, and Planck's constant h). Higher accuracy is not needed in this work, because of the energetic resolution of approx. $100\,\text{meV}$ of the experimental setup.

In inorganic solids many atoms are close together and the interaction and overlap of the electron wave functions have a long range. Thus the states are not finite anymore and broad bands are formed. This leads to more delocalized states.
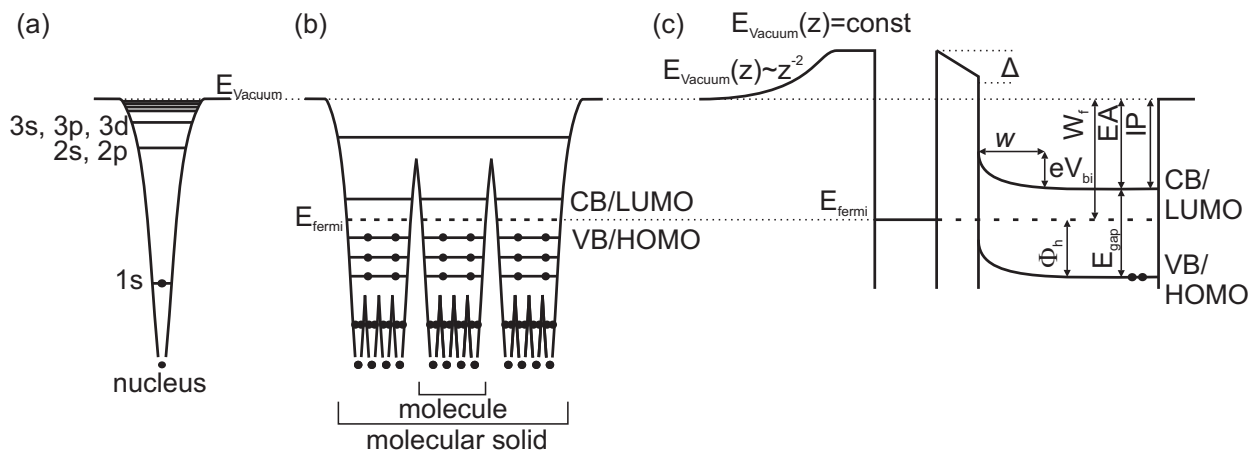
Fig. 2.1: *(a) A single atom with one proton, making up the nucleus (i.e., hydrogen), gives the possibility to calculate the energetic states. (b) A single molecule consists of a few atoms. In organic bulk materials the molecules are still separated and the orbitals are more localized and less interacting compared to inorganic bulk materials. (c) The connection of a metal and a semiconductor can lead to an interface dipole (Δ), band bending with the built-in potential (eV_{bi}), and the width (w). (adapted from [5])*

In the ground state, the bands are filled after each other depending on the total energy beginning with the lowest quantum number and according to Hund's rules. The last filled state is called valence band (VB). The lowest unoccupied state in inorganic solids is called conduction band (CB). The energy needed to extract an electron from the VB into vacuum or inject from vacuum into the CB is called ionization potential (IP) or electron affinity (EA), respectively. The energy difference is called energy gap E_{gap} (see Fig. 2.1).

Organic solids contain carbon which forms hybrid orbitals, a mixture of the 2s and the 2p atomic orbitals. The C-atom can be bond to two (sp), three (sp^2), or four (sp^3) other atoms. As sp^2-hybridization is the only relevant bonding in the molecules regarded in this thesis, sp- and sp^3-hybridization are not discussed further. The orbital formed by the sp^2 electrons are aligned in one plane and called σ-orbital. The remaining p-orbital is perpendicular to this plane and called p_z-orbital. In combination with adjacent sp^2-hybridized atoms, the p_z-orbital may be delocalized and overlap. Thus it is called π-orbital.

The calculation of molecular orbitals (MO) Ψ^{mol} can be done by a linear combination of atomic orbitals Φ^{atom} (LCAO) with the coefficients c_{ij}.

$$\Psi_i^{mol} = \sum c_{ij} \Phi_j^{atom} \qquad\qquad LCAO \qquad\qquad (2.1\text{-ii})$$

This leads to a simplification of the otherwise under-determined Schrödinger equation, whereby the coefficients can be optimized using numerical methods. This can be done by means of Hartree-Fock method, the results are symmetric and antisymmetric wavefunctions, called bonding (σ, π) and antibonding ($\sigma^\star$, $\pi^\star$), respectively. The electronic interaction is not considered in the Hartree-Fock approach [6]. Therefore, density functional theory (DFT) is applied which was introduced by Hohenberg [7] and Kohn [8].

Similar to inorganic solids the orbitals are filled depending on the total energy. The energy gap is formed between the highest occupied molecular orbital ($HOMO$) and the lowest unoccupied molecular orbital ($LUMO$). Applying Koopman's theorem [9], the energy of a single particle wavefunction (E_{HOMO}) equates approximately the negative ionization potential (IP) of a many-body system. Contrary to the inorganic bulk material the orbitals of organic bulk materials are localized to the single molecules. Hence no broad bands are formed. This leads to low charge carrier mobilities and a different transport mechanism. Charge transport in rubrene (organic material with highest mobility) can still be described by band transport, as it is done in inorganic materials, while hopping transport is the dominant regime in all other organic materials [10].

For conductivity the density of charge carriers plays an important role, besides mobility. In classical semiconductors it can be calculated from Fermi-Dirac statistics. In undoped semiconductors the Fermi energy (E_{Fermi}) can be calculated from the effective number of states N of the respective band and is located in the energy gap $E_{gap}^{transport}$ for semiconductors.

$$E_{Fermi} = \frac{E_{CB} - E_{VB}}{2} + \frac{kT}{2} \cdot ln\left(\frac{N_{VB}}{N_{CB}}\right) \qquad (2.1\text{-iii})$$

$$E_{gap}^{transport} = E_{CB} - E_{VB} \qquad (2.1\text{-iv})$$

For the energy gap one has to discriminate between transport gap ($E_{gap}^{transport}$) and optical gap (E_{gap}^{opt}) [11]. While $E_{gap}^{transport}$, also called fundamental gap, is really the separation of the electronic states $CB/LUMO$ and $VB/HOMO$, the $E_{gap}^{optical}$ gap is lowered by the value of the exciton binding energy ($E_{bind}^{exciton}$). In inorganic materials the latter is in the order of the thermal energy and therefore it is quite often neglected. In organic semiconductors not only the exciton binding energy is much larger. Another difference can be observed comparing single molecules (e.g., in the gas phase) and bulk materials as polarization effects (P) and disorder lead to a broadening of the orbital states (see Fig. 2.2 b). Both, exciton binding

energy and polarization result in a reduced energy gap. Another effect for lowering the gap is the molecular size, as more atomic orbitals are involved in the molecular orbitals (see Fig. 2.2 d).
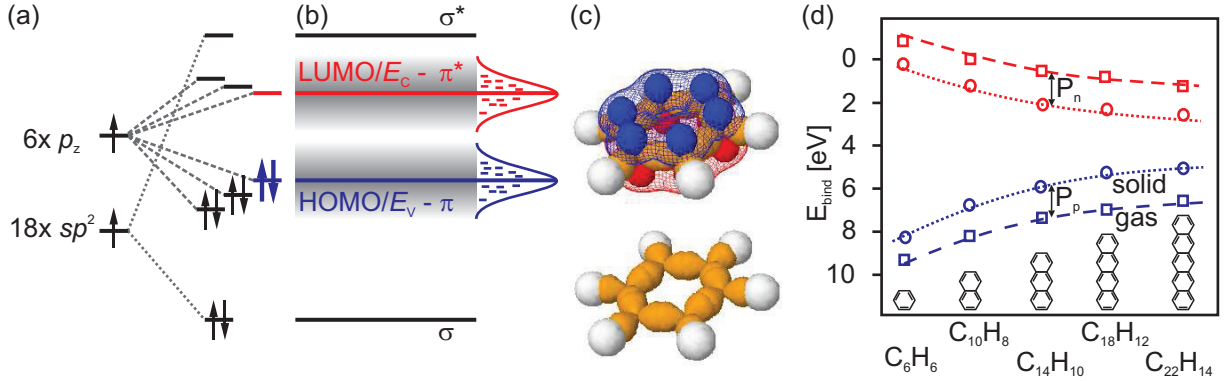

Fig. 2.2: *Forming benzene from carbon leads to splitting of the p_z and sp^2 orbitals (a), forming the π- (blue and red region in c) and σ- (yellow region in c) orbitals respectively (adapted from [12]). The states are filled up to the binding π-orbital which is located at the valence energy E_V and called HOMO, whereas the antibinding $\pi^\star$-orbital which is called LUMO is empty. Because of disorder and polarization effects, the orbitals becomes broadened in bulk material (b). The bandgap is formed by the delocalized π- and $\pi^\star$-orbital. If the molecule size increases and so the delocalization, the bandgap decreases (d adapted from [13]). The difference in gap energy between single molecules in the gas phase and molecules with polarization P in solids can also be observed.*

Since a fixed energy position for absolute determination is missing, only energy differences can be measured. Close to the energy gap most energies are given with the Fermi energy as reference point, as it will be used as underlying alignment rule (see following section). The important values in this thesis are the hole injection barrier (Φ_{hole}) and the workfunction (W_f), specifying the energy difference of the E_{Fermi} to the $VB/HOMO$ and to the E_{vacuum}, respectively (see Fig. 2.1 c). E_{vacuum} also depends on the properties and spatial distance from the surface. Quite close to the surface a constant value can be assumed. This value of free electrons close to a material surface differs from that of really free electrons (see $E_{vacuum}(z)$ in Fig. 2.1 c). Close to the surface a dipole is assumed which increases the E_{vacuum}. At larger distances the surface dipole can be regarded as point source [5] and the value of free electrons will be approached asymptotically. The workfunction can also be decreased by adsorbates [14]. The energy difference between the electronic states can

Fig. 2.3: *(a) Absorption of the material can be linked to the transition from a ground state (S_0) to an excited state (S_1). After relaxation the recombination process to the ground singlet state S_0 from the excited singlet state S_1 or after spin flipping from the triplet state T_1 can be observed as fluorescence or phosphorescence, respectively. (b) The transition energies can be plotted in a spectrally resolved graph. Due to the lower energy of the triplet states, the phosphorescence graph (green) is shifted compared to the fluorescence graph (blue). In the luminescence spectra of bulk material (not shown here) additional features may occur compared to the spectra of single molecules. The absorption of single molecules (thick red line) shows sharp features, while the absorption of bulk material (thin dotted dashed red line) shows broadening (because of transition dipole interaction) and often additional features (e.g., CT states). Peak maxima can also be shifted by different dielectric background.*

be observed by means of optical spectroscopy in form of electron transitions. Absorption leads to occupation of an excited state, and the absorbed photon energy corresponds to the energy difference of the involved states. The sharp features are lost when investigating bulk material, because interaction leads to broadening [15]. In the case of luminescence, the emitted photon energy also corresponds to transition energy (see Fig. 2.3).

2.1.2   Interfaces and Band Alignment

The understanding of bulk material consisting of many atoms and the vacuum interface is quite complicated. Moreover, typical devices consist of a number of different layers and accordingly of different interfaces. Hence, it is necessary to investigate even more complex interfaces consisting of different materials. In general, different materials are characterized

by different workfunctions [14]. This leads to a potential difference at the interface and an electric field, which affects the charge carriers. Depending on the charge carrier concentration and mobility in the materials different models are used. Considering only metals, Fermi-level alignment is assumed, as the charge carriers are mobile and can move in the direction of the electric field. The other extreme case are insulators with almost no free mobile charge carriers. Here vacuum-level alignment is assumed, also called Schottky-Mott-Rule. Yet the material variety between both extreme cases is quite large. Investigating the interface of semiconductors, local changes of the concentration of charge carriers can be observed which leads to band bending. The complete width w of the band bending depends on the dopant concentration N and is pronounced in respective larger depth d in the material with lower concentration. At a p-n-junction, the difference of the workfunctions W_f results in the built-in potential $e \cdot V_{bi}$.

$$e \cdot V_{bi} = {}^n W_f - {}^p W_f = \frac{e}{2 \cdot \varepsilon} \cdot (N_A \cdot d_p^2 + N_D \cdot d_n^2) \tag{2.1-v}$$

$$d_p = \sqrt{\frac{2 \cdot \varepsilon \cdot U_{bi}}{e}} \sqrt{\frac{N_D}{N_A \cdot (N_A + N_D)}} \tag{2.1-vi}$$

$$d_n = \sqrt{\frac{2 \cdot \varepsilon \cdot U_{bi}}{e}} \sqrt{\frac{N_A}{N_D \cdot (N_A + N_D)}} \tag{2.1-vii}$$

$$w = d_n + d_p = \sqrt{\frac{2 \cdot \varepsilon \cdot U_{bi}}{e}} \sqrt{\frac{N_A + N_D}{(N_D \cdot N_A)}} \tag{2.1-viii}$$

Depending on the relation of the position of the bandgaps of two semiconductors forming an interface, one distinguishes three types of band discontinuities: type I is the "struggling gap", meaning one gap is completely within the other one; type II is the "staggered gap", meaning there is an overlap of the gaps; type III is the "broken gap", meaning there is no overlap at all. To avoid recombination effects, the staggered gap is desired in solar cell devices, if a homojunction is out of question.

Besides the classical known inorganic semiconductors, the field of organic semiconductor emerged in the last decades [16]. In the early years of research on organic semiconductors, the Schottky-Mott-Rule was predicted to be valid [17]. After discovering the formation of dipoles at the interface new models [5, 18–24] were established including the interface dipole (Δ). The explanations of the origin of the dipole are manifold. As mentioned above, the workfunction can be decreased by adsorbates [14]. This is called "pillow-effect" (Δ_{pillow}).

Using organic molecules, permanent molecular dipoles (Δ_{mol}) are observed. Both effects are surface related and lead to an abrupt change of the workfunction [19]. Another feature, which is classically seen in terms of band bending is the "induced density of interface states" (IDIS), which is formed at materials with different workfunctions [21]. The influence of the single parts can be described by the shielding factor S.

$$\begin{aligned}
\Delta &= \Delta_{pillow} + \Delta_{mol} + \Delta_{IDIS} \\
&= \Delta_{pillow} + \Delta_{mol} + (1 - S) \cdot \left({}^A W_f - \Delta_{pillow} - \Delta_{mol} - {}^B W_f\right) \\
&= (1 - S) \cdot \left({}^A W_f - {}^B W_f\right) - S \cdot \left(\Delta_{pillow} + \Delta_{mol}\right)
\end{aligned} \qquad (2.1\text{-ix})$$

High shielding ($S = 1$) leads to a pronounced appearance of the pillow-effect and the molecular dipole, whereas in the case of $S = 0$ the dipole results from pinning of the Fermi level to the so-called charge neutrality level (CNL) [22].

2.1.3   Hybrid Concept – Inorganic and Organic Solids

A hybrid concept stands for the combination of the properties of the constituents. In the present case, it is desired to combine the good electric properties of inorganic materials with the good optical properties of organic molecules (see Tab. 2.1). Inorganic semiconductors are well-known, which is why this thesis focuses more on the organic part. ZnO was extensively
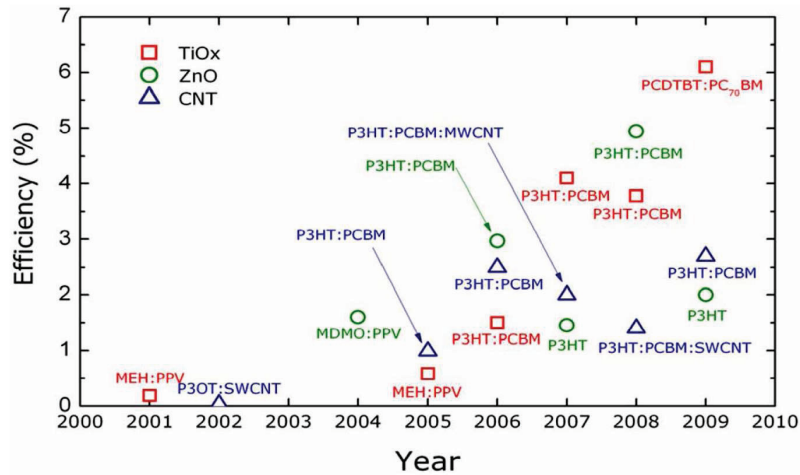

Fig. 2.4: *Progress of hybrid solar cells until 2010. (Graph was taken from [25])*

studied and showed suitable properties, such as: high thermal conductivity, light stability, high carrier concentration and mobility. Besides this II-VI-semiconductor, CdS is also used

Tab. 2.1: *Selected parameters of several inorganic and organic semiconductors used in photovoltaics. The mobility represents the good electric properties of inorganic materials. Extremely small data are neglected (dash).*

	electr.	hole	reference	absorption	reference
	mobility μ			coefficient α	
	$[^{cm^2}/_{Vs}]$			$[^1/_{cm^1}]$	
Si	1350	480	[26]	10^2 (above $1.2\,eV$)	[27]
ZnO	200	180	[28]	10^7 (above $3.4\,eV$)	by M. Grünewald
CdS	340	50	[28]	10^7 (above $2.6\,eV$)	[29]
PEDOT	–	20	[30]	10^5 (above $5.3\,eV$)	[31]
C_{60}	≤ 4.9	–	[32]	10^4 (above $3\,eV$)	[33]
P3HT	0.01	–	[34]	10^5 ($2\,eV$ - $3\,eV$)	[33]
ZnPc	–	0.005	[35]	10^7 ($1.5\,eV$ - $2.5\,eV$)	[36]

for comparison. On the other hand also organic materials are well suited for solar cells. First experiments were done in 1992 [37] while device measurements started in the year 2001 (see Fig. 2.4). In the beginning TiO_2 was applied as electrode. The idea of improvements via nanostructures, e.g., CNT, comes quite fast and also other metal oxides like ZnO were used. The organic component in the first hybrid solar cells was dominated by conducting polymers. Focusing on pure organic solar cells mainly small molecules are used i.e., C60, pentacene, ZnPc. The latter one will also be used in this thesis. The advantages of small molecules are manifold. High and spectrally selective light absorption and emission is combined with simple layer deposition techniques and a large material variety. In combination with ZnO, inverted structures (i.e., transparent contact as electron collector) seems to be the best performing hybrid solar cell [25]. For this reason the inverted cell structure was implemented in this work.

2.2 Characteristics of Solar Cells

Power conversion efficiency η is one of the most important values in photovoltaics along with manufacturing costs and lifetime. It is the extractable electric power $P_{electric}$ with respect to the power of the incident light P_{light}.

$$\eta = \frac{P_{electric}}{P_{light}} \tag{2.2-i}$$

The extractable power results from the current (density)-voltage characteristic of the device (see Fig. 2.5). In this chapter, current I and current density j are dealt with equivalently due to the lack of qualitative differences. The latter is just a normalization to an equal area
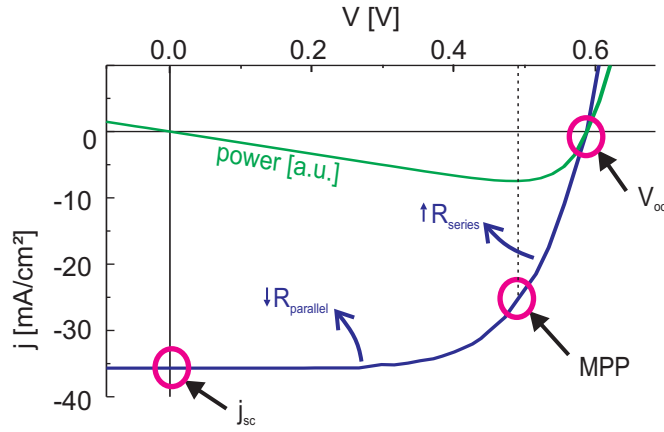
Fig. 2.5: *Example of a current (density)-voltage characteristic of a solar cell with an efficiency of $\approx 12\%$. The three red circles mark the important factors influencing the efficiency: short circuit current density (j_{sc}), open circuit voltage (V_{oc}), and maximum power point (MPP). The blue arrows indicate the influence of a lower parallel resistance ($R_{parallel}$) and an higher series resistance (R_{series}).*

which has little impact (see section 2.2.3).

In the idealized case it is an exponential function.

$$I_{ideal}(V) = I_s \cdot e^{\frac{e \cdot V}{n \cdot k \cdot T}} - I_{photo} \tag{2.2-ii}$$

A common descriptive model takes a diode-like behavior as basis with the saturation current I_s, the ideality factor n and an offset I_{photo}, which results from the photogenerated charge carriers. The exponent is the quotient of electric energy (voltage V, elementary charge e) and the thermal energy (Boltzmann's constant k, temperature T). The derivation of this

equation can be found at the end of section 2.2.1. The working point, formally known as maximum power point (MPP), defines the highest fill factor (FF), the ratio of the product of voltage V_{MPP} and the corresponding current $I_{MPP}(V_{MPP})$ and the product of open circuit voltage V_{oc} and short circuit current I_{sc}.

$$FF = \frac{I_{MPP} \cdot V_{MPP}}{I_{sc} \cdot V_{oc}} = \frac{P_{electric}}{I_{sc} \cdot V_{oc}} \tag{2.2-iii}$$

$$\eta = \frac{I_{MPP} \cdot V_{MPP}}{P_{light}} = \frac{I_{sc} \cdot V_{oc} \cdot FF}{P_{light}} \tag{2.2-iv}$$

Thus the three parameters FF, I_{sc}, and V_{oc} are the main factors of influence on the efficiency of a solar cell.

2.2.1 Open Circuit Voltage (V_{oc})

The open circuit voltage is defined as the potential difference which has to be applied across the device, so that no current flows. In detail, this means that all currents compensate. These include diffusion currents and drift currents. Diffusion (D_n, D_p) arises through the gradient of concentration differences (n, p) of the single charges (q). Drift sets in by the mobility μ of the single charge carriers in an electric field $\vec{E}$.

$$\sum I = \int \vec{j} d\vec{A} = \int \vec{j}_{diff} d\vec{A} + \int \vec{j}_{drift} d\vec{A} = 0 \Leftrightarrow V = V_{oc} \tag{2.2-v}$$

$$\vec{j}_{diff} = \vec{j}_{diff,n} + \vec{j}_{diff,p} = q \cdot (D_n \cdot \vec{\nabla} n + D_p \cdot \vec{\nabla} p) \tag{2.2-vi}$$

$$\vec{j}_{drift} = \vec{j}_{drift,n} + \vec{j}_{drift,p} = q \cdot (\mu_n \cdot \vec{E} + \mu_p \cdot \vec{E}) \tag{2.2-vii}$$

By applying an outer voltage an electrical field $\vec{E}$ is produced, which causes a shift of the equilibrium. This varies the number of charge carriers which overcome the barrier, resulting among other things from the built-in potential (eV_{bi}). This number, in which the current results, depends exponentially on the external voltage (V).

$$I \propto e^{-\frac{eV_{bi} - eV}{k \cdot T}} \tag{2.2-viii}$$

With knowledge of the material parameters, one finds the typical diode current-voltage relationship [2, 38].

$$I_{diode} = I_s \cdot \left[e^{-\frac{eV}{k \cdot T}} - 1 \right] \tag{2.2-ix}$$

$$I_s = q \cdot \left(\frac{D_p}{L_p} \cdot p_n + \frac{D_n}{L_n} \cdot n_p \right) \approx q \cdot n_i^2 \cdot \left(\frac{D_p}{N_D \cdot L_p} + \frac{D_n}{N_A \cdot L_n} \right) \tag{2.2-x}$$

Under illumination additional charge carriers are generated. These particles create the photocurrent I_{photo}. Assuming current compensation under illumination conditions (i.e., $I_{diode} = I_{photo}$) the open-circuit voltage can be calculated.

$$0 = I_s \cdot \left[e^{-\frac{eV_{oc}}{k \cdot T}} - 1 \right] - I_{photo}$$

$$V_{oc} = \frac{k \cdot T}{e} + ln\left(1 - \frac{I_{photo}}{I_s} \right) \approx \frac{k \cdot T}{e} + ln\frac{I_{photo}}{I_s} \tag{2.2-xi}$$

The origin of the open-circuit voltage of hybrid as well as organic solar cells is not yet fully understood. In chapter 6.2 it is shown that there is a connection to the electronic structure.

2.2.2 Short Circuit Current (I_{sc})

The photocurrent leads to a negative offset in the current-voltage characteristic which is dubbed short-circuit current (I_{sc}).

$$I_{sc} := I_{photo}(0V)$$

$$I(V) = I_s \cdot [e^{-\frac{eV}{k \cdot T}} - 1] - I_{sc} \tag{2.2-xii}$$

The short-circuit current results from the number N_{cc} of generated and collected charge carriers.

$$I_{sc} = \frac{\partial Q}{\partial t} \tag{2.2-xiii}$$

$$Q = \sum q = N_{cc} \cdot e \tag{2.2-xiv}$$

$$N_{cc} = \eta_{total} \cdot N_{photon} \tag{2.2-xv}$$

$$\eta_{total} = \eta_{photon}^{abs} \cdot \eta_{exc}^{diff} \cdot \eta_{exc}^{diss} \cdot \eta_{e-h}^{coll} \tag{2.2-xvi}$$

Current is defined as time dependent change of the charge $\frac{\partial Q}{\partial t}$. The charge consists of both holes and electrons, whose sum N_{cc} results from the conversion of photons via excitons. The efficiencies of this process η_{total} can be expressed as the product of the efficiencies of the individual steps (see 2.2-xvi). Incoming photons are partially reflected and absorbed in upper layers, so that only a portion of the radiation in the active layer, relevant for carrier generation, arrives (η_{photon}^{abs}). In the active layer the photons are absorbed and thereby decreased. This can be described in good approximation by the Lambert-Beer law.

$$\eta_{photon}^{abs} = 1 - e^{-d \cdot \alpha} \tag{2.2-xvii}$$

Neutral quasi particles called exciton, which can be regarded as electron-hole pairs, result from the absorption of photons. These pairs are bound by the Coulomb force ($F_{Coulomb} \propto \varepsilon^{-1}$). This attractive force is much larger in organic materials than in inorganic materials, because of a lower dielectric constant [39].

One distinguishes three main types of excitons: In inorganic semiconductors, the radii are large ($\approx 10\,\mathrm{nm}$), and the binding energies are rather small ($\approx 0,1\,\mathrm{eV}$). One speaks of Wannier-Mott excitons. In organic semiconductors, excitons are strongly bound to a molecule, which is why the radii are small ($\approx 1\,\mathrm{nm}$) and the binding energies are large ($\approx 1\,\mathrm{eV}$) [39]. An excited state, which is localized on one single molecule is called Frenkel exciton. If the electron and hole are localized on different molecules it is called charge-transfer exciton.

Due to the composition of an electron and a hole, excitons tend to recombine. In the organic material this recombination acts much faster due to the small exciton radius. Besides recombination, dissociation can take place (see chapter 6) and leads to free charge carriers. For the short-circuit current only the charge carriers reaching the contacts count (see chapter 5). Hence, the charge transport plays an important role. Short and crystalline pathways are preferred. Transport pathways may be affected by the integration of nanostructures. So it is possible to produce an enlarged absorption despite of short transport pathways.

2.2.3   Resistances and Fill Factor (FF)

The fill factor determines the operation point of the solar cell (see 2.2-iv). Graphically it is the ratio of the areas of the two rectangles with side lengths $I_{MPP} \cdot V_{MPP}$ and $I_{sc} \cdot V_{oc}$. In reality, the characteristic curve of the device is influenced by additional parameters. Two important features can be described by parallel resistance $R_{parallel}$ and series resistance R_{series} (see Fig. 2.5) [40].

$$I(V, R_{parallel}, R_{series}) = I_s \cdot e^{\frac{V - I \cdot R_{series}}{n \cdot k \cdot T}} + \frac{V - I \cdot R_{series}}{R_{parallel}} - I_{photo} \qquad \text{(2.2-xviii)}$$

The exponential behavior of the I-V-curve results by the p-n-junction. Because of cables, morphology of the layers, different material compositions, and resulting interfaces the voltage drops on the pathway of the charge carriers towards and away from the p-n-junction. This is represented by the series resistance which lowers the slope in forward direction. For

this reason the maximum power point is shifted to lower voltages. Furthermore shunts, represented by the parallel resistance, form bypasses of the p-n-junction. For this reason low parallel resistance annihilates the p-n-junction. The slope in reverse direction is increased, and the maximum power point is shifted to lower current.

Thus, studies of the morphology and appropriate contact choice are important for a high fill factor.

Chapter 3

EXPERIMENTAL DETAILS

In this chapter a brief overview of the materials used, the deposition processes applied, and the techniques which were used for characterization will be given.

3.1 Sample Preparation and Materials

The solar cells, which are considered in this work, consist of at least four layers on a substrate (see Fig. 3.1). The main part is formed by the p-n-junction, which consists of an n-type inorganic semiconductor and a p-type organic molecule. In this work mainly zinc oxide
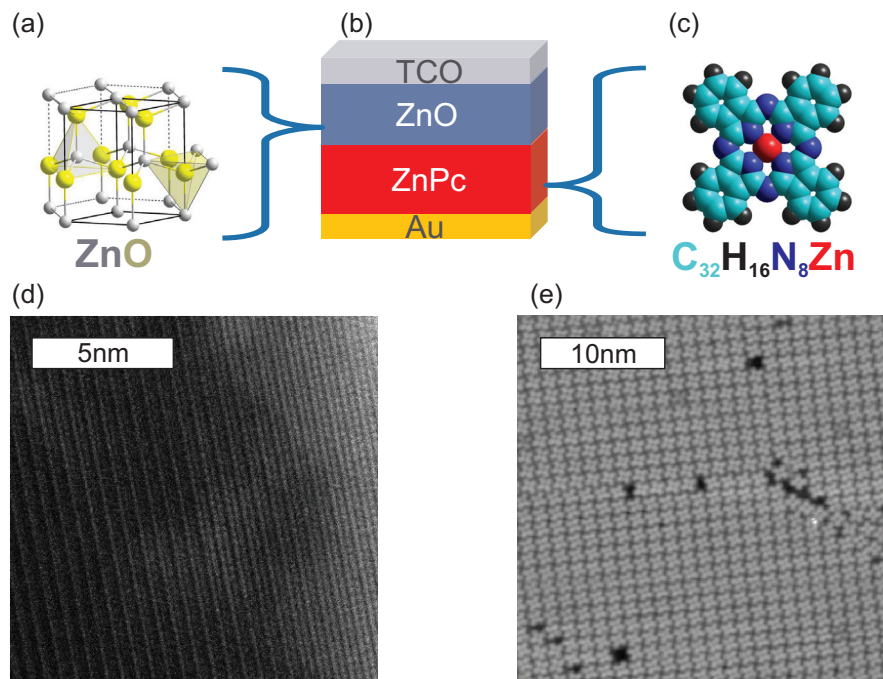
Fig. 3.1: *(a) Structural formula of zinc oxide (ZnO). (b) Sketch of the solar cells with the main components forming the important p-n-junction used in this work. (c) Structural formula of zinc phthalocyanine (ZnPc). (d) HR-TEM image of crystalline ZnO and (e) LT-STM image of a single layer of the similar CuPc molecules on a silver substrate (provided by M. Grünewald from IFK Jena).*

was used as inorganic component because it showed good performance in pure inorganic solar cells [41–43]. Likewise zinc phthalocyanine was employed based on the experiences in pure organic devices [44–46]. The inorganic-organic double layer is sandwiched between a transparent conducting oxide (TCO) on the glass side and a noble metal as second electrode. In further studies, an electron blocking layer (EBL) as well as a dopant are introduced, which will be discussed in detail later. The motivation for the choice and the preparation of the single layers is given below.

Substrates and Conductive Oxides

Different types of glasses were used as substrate material. Due to the well-known optical constants and thermal stability quartz glass was used for characterization experiments. Additionally 2 mm thick borosilicate prepared by float glass process coated with ITO delivered from Schott was used for the device setup. Indium doped tin oxide (ITO) or aluminum doped zinc oxide (AZO) were used as transparent conducting oxides (TCO). All substrates were polished with an optical tissue. Afterwards a cleaning in ultrasonic acetone bath was performed. Finally the substrates were rinsed with isopropyl alcohol and dried under flowing dry nitrogen.

Inorganic Component

The inorganic layer was prepared by sputter deposition. Intrinsic zinc oxide (ZnO) as well as cadmium sulfide (CdS) were used. Both materials are well known in inorganic thin film solar cells. It is also possible to synthesize nanostructures as well as layered structures from these materials. The latter are much better to investigate interface processes. Both inorganic semiconductors show a large energy gap compared to the organic material. This leads to absorption in different spectral regions. Hence, conclusions for the single material can be drawn while optical investigation of stacked layers.

Depending on the target material and the carrier gas, intrinsic zinc oxide (ZnO) or aluminum doped zinc oxide (AZO) can be deposited. The parameters used are an electrical power of 150 W or 200 W and a flow of argon or an argon mixed with 5 % oxygen at 6 sccm to produce ZnO or AZO layers, respectively. The pressure was kept at around $3\text{x}10^{-3}$ mbar and the thickness could be tuned by the sputtering time with a constant rate of 5 $^{\text{nm}}/_{\text{min}}$

or 17 $^{nm}/_{min}$ for ZnO or AZO, respectively. The additional oxygen during ZnO deposition avoids the creation of oxygen vacancies V_O, which would act as donor and increase the conductivity [47]. This is, in contrast to AZO, not desired in the pure ZnO layer.

An improvement of the solar cell efficiency can be achieved by introducing nanowires (NWs) [48, 49], which in case of ZnO can be synthesized by different techniques (e.g., MBE [50], MOVPE [51], solvent [52], vapor transport [53]). In this work the vapor liquid solid (VLS) method [54] was used. ZnO powder (Alfa Aesar: 99.99 %) as source material together with a stoichiometric amount of carbon (Alfa Aesar: 99.99 %) is placed in the center of a horizontal tube furnace at a temperature of 1050 °C. Due to the low thermal stability of the glass substrates the sublimation temperature can be decreased by using the carbon assisted growth [55]. The growth time was in the order of 30 min at a pressure of 7 mbar and a gas flow of approx. 20 sccm (10 sccm argon + 10 sccm oxygen). ZnO is a high conductive semiconductor with a band gap of approx. 3.4 eV [47]. This makes it a proper candidate for solar cells.

The CdS layers used were prepared by the photovoltaic group of the Institute of Solid State Physics. On top of 2.2 mm *Tec*7 glass with a fluorine doped tin oxide (FTO) layer CdS was deposited at a temperature of 700 °C with a deposition rate of 150 $^{nm}/_{min}$.

Organic Layer

Small organic molecules show a high absorbance in the visible spectral region, especially zinc phthalocyanine (ZnPc, CAS: 14320-04-8), which is frequently used in organic light emitting devices (OLED) or organic solar cells. In this work ZnPc powder (Sigma Aldrich: 97 %) was sublimated with a rate monitored by a oscillating quartz of 0.1 $^{nm}/_s$ at a pressure of 5×10^{-6} mbar and a temperature of around 400 °C. In this work 2,3,5,6-tetrafluoro-7,7,8,8-tetracyanoquinodimethane (F_4TCNQ, CAS: 29261-33-4) was used as acceptor molecule by co-evaporation at a pressure of 5×10^{-6} mbar and a temperature of around 110 °C.

Electron Blocking Layer

Most highly efficient solar cells contain additional layers like anti reflectance coatings, spacer or electron and hole blocking layers to avoid charge carriers coming to the wrong electrode leading to recombination. In this thesis poly(3,4)-ethylenedioxythiophene (PEDOT) doped

with polystyrenesulfonate (PSS) and mixed with a surfactant made of 5-chlor-2-methyl-2H-isothiazol-3-on and 2-methyl-2H-isothiazol-3-on (3:1) was used. PEDOT:PSS (CAS: 155090-83-8) is a well known electron blocking (EBL) and hole injection/transport layer[56–58]. It is used to protect the organic layer from the metal cathode while coating because metal atoms can penetrate the organics or even lead to chemical reaction [5]. As PEDOT:PSS was delivered as solution (1.3 wt % dispersion in H_2O from Sigma Aldrich) it was deposited by spin coating. After an initial ramp to 500 rpm for 10 s the spinning takes place at 2500 rpm for 30 s. Before stopping a final acceleration to 5000 rpm for 5 s was done. The surfactant was used with the aim especially to infiltrate the pores in the nanostructured devices (see Fig. 7.7).

Top Contact

The top electrode was made by gold as it is noble and therefore less susceptible to oxidation and degradation. Deposition was done by thermal evaporation at a pressure of around 10^{-6} mbar from a tungsten crucible or by sputter deposition at around $8\text{x}10^{-2}$ mbar under argon atmosphere with a plasma current of 20 mA.

3.2 Characterization Methods

Scanning Electron Microscopy

Scanning electron microscopy (SEM) [59] was performed with JEOL JSME-6490 and FEI NanoLab Helios 600i. The JEOL system works with a LaB6 cathode at acceleration voltages of $10\,\text{kV}$ to $20\,\text{kV}$ and has the advantage of a mounted energy dispersive x-ray detector (EDX) which is evaluated with the software EDAX GENESIS [59, 60]. The FEI system is operated at lower energies ($0.5\,\text{keV}$), but gives a higher resolution due to electrons generated by field emission instead of bare thermal emission. An additional Ge-ion gun gives the possibility of in-situ manipulation and measurements (e.g., cross section).

Scanning Tunneling Microscope (STM)

The *UHV STM* 1 developed by *Omicron* was used for scanning tunneling microscopy (STM) [61, 62]. Besides the tip-sample-distance, the tunneling current I_{tunnel} depends on the density of states (DOS) ρ and the workfunction W_f.

$$
\begin{aligned}
I_{tunnel} = & A \frac{2\pi e}{\hbar} \frac{\hbar^2}{2m} \int \rho_{sample}\left(E\right) \rho_{tip}\left(E - eV\right) \\
& exp\left[-2\left(z + R\right) \sqrt{\frac{2m}{\hbar^2}\left(W_f + \frac{eV}{2} - E\right)}\right] dE
\end{aligned}
\tag{3.2-i}
$$

Detecting the current while driving the bias with constant height at a single position allows to get the local DOS of the sample ρ_{sample}, which is proportional to the deviation $\frac{dI}{dV}$ assuming a constant DOS of the tip ρ_{tip}. The basic assumption is that deeper states show a lower detection probability [63, 64]. On the other hand by driving the distance at constant bias, the workfunction can be calculated from the deviation of $ln(\frac{dI}{dz})$. These methods can be used to derive the electronic structure locally. For the evaluation it is common to average many spectra or to use lock-in techniques because the very low current is easily influenced by noise.

Atomic Force Microscope (AFM)

The organic layers were scanned with an atomic force microscope (AFM) [61, 65] under atmospheric conditions. This was done with the *Easyscan* 2 *AFM* by *nanoScience*.

Photoelectron Spectroscopy (PES)

Photoelectron Spectroscopy (PES) [66] was performed with an hemispherical energy analyzer
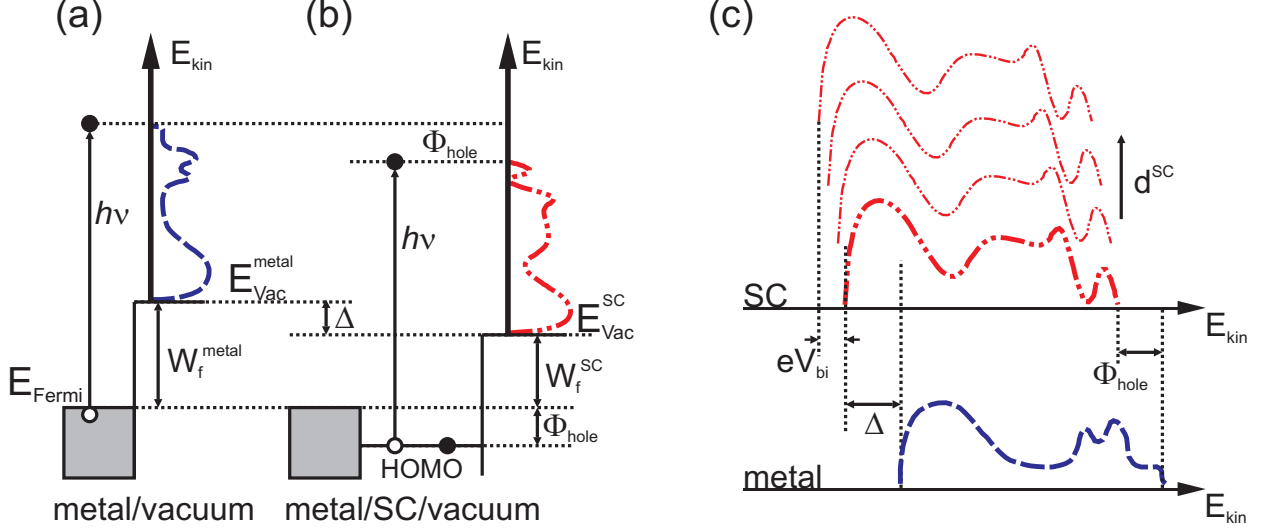EA 200 by $SPECS$ and two different photon sources.

Fig. 3.2: *A photon source (HeI or Al K) with the energy $h\nu$ (21.2 eV or 1486.6 eV) illu-
minates the sample. Electrons below (a) the Fermi energy or (b) the valence
structure are emitted from the metal or a semiconductor (SC), respectively.
Depending on the parameters of the detector (e.g., pass energy, aperture) a
spectrum is plotted as intensity (counts per second) versus energy channel. (c)
The features and the shape of the spectrum can be used to determine the work-
function W_f, the interface dipole Δ, the hole injection barrier Φ_{hole} and the
built-in potential eV_{bi} in respect to the thickness d which are needed to derive
the electronic structure (adapted from [5]).*

X-rays were generated using an Al cathode (AlK_α, 1486.6 eV) to excite core levels (XPS).
The XPS peak energy and intensity give information on the chemical environment and
stoichiometry, respectively.

By using a helium gas lamp one can excite the sample with ultraviolet light (UPS). In
this work the lamp was optimized for HeI (21.2 eV) to measure the valence structure with
an energy step size of 0.03 eV. The secondary electron background was increased by applying
bias voltage to the sample of approx. 9 V. This also increases the kinetic energy and gives
the possibility to measure the work function (see appendix A.1) which in some cases can be
lower than the detector work function.

The samples were analyzed at a pressure of 3x10^{-9} mbar. The aperture used gave an

acceptance angle of $8°$ while investigating the electrons perpendicular to the sample surface with an intensity of a few $100\,$kcps.

Optical Spectroscopy

Transmission and reflection can be examined by means of a Varian Cary 5000 UV-Vis spectrophotometer. The transmission measurements have been done using a light beam perpendicular to the sample surface, while the angle of incidence is $12°$ in reflection geometry. In both cases unpolarized light was used. The spectrophotometer was operated in a dual-
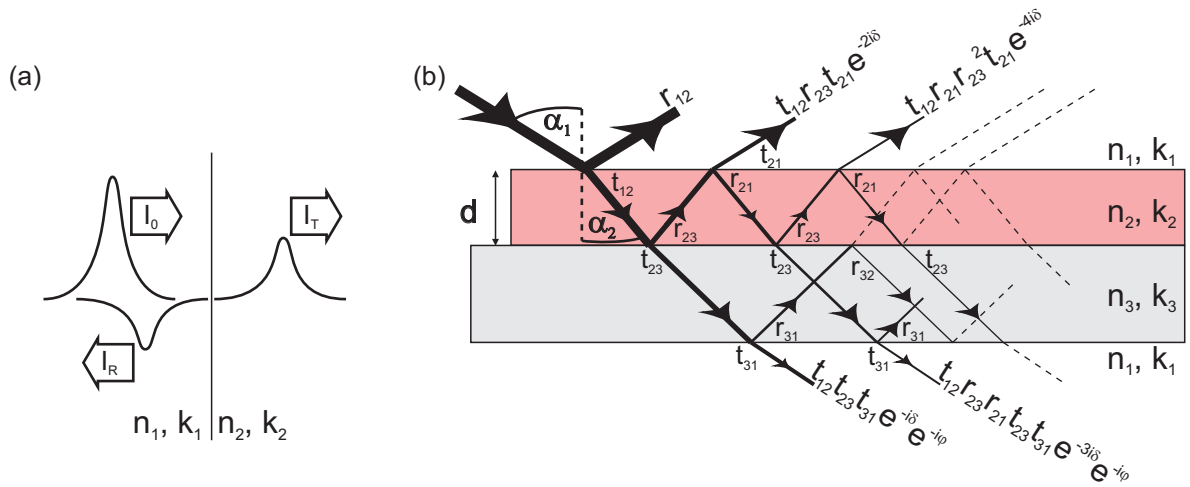
Fig. 3.3: *Illumination of a sample leads to reflection, transmission, scattering and absorption. (a) The impinging intensity (I_0) is separated in the reflected (I_R) and transmitted intensities (I_T) and can be calculated, knowing the optical constants n and k and the thickness d. (b) The Fresnel coefficients (t, r) and the phase terms (δ, φ) can be used to determine the detectable light including multi scattering.*

channel mode which enhances the long term (several hours) stability significantly. The scanning velocity was set to $300\,$nm/min (averaging time: $0.2\,$s) in the NIR-region and $120\,$nm/min (averaging time: $0.5\,$s) in the UV-Vis region with a fixed spectral bandwidth of $5\,$nm and $4\,$nm, respectively. The resulting resolution is by far sufficient for the typical line widths of organic thin films at room temperature.

Light is regarded as electromagnetic wave with the wave vector $\vec{k}_e$, the frequency $\vec{\omega}$, and the phase shift δ. The intensity I of the electric field vector $\vec{E}$ can be calculated by the

absolute square value.

$$\vec{E}\left(\vec{r}, t\right) = \vec{E}_0 \cdot exp\left\{-i\left(\vec{k}_e\vec{r} - \omega t + \delta\right)\right\} \tag{3.2-ii}$$

$$I = \left|\vec{E}_0\right|^2 \tag{3.2-iii}$$

In combination with the Helmholtz equation it can be shown, that the wave vector is correlated to the optical constants n (the refractive index indicating the phase velocity) and k (the extinction coefficient).

$$\left|\vec{k}_e\right| = \omega\sqrt{\varepsilon_0\widehat{\varepsilon}\mu_0\mu_r} = \frac{\omega}{c}\sqrt{\widehat{\varepsilon}\mu_r} \overset{\mu_r=1}{=} \frac{2\pi}{\lambda}\widehat{n} \tag{3.2-iv}$$

$$\widehat{n} = n - ik \tag{3.2-v}$$

If the light meets an interface of two materials with different optical constants, partial transmission $(T = \frac{I_T}{I_0})$ and reflection $(R = \frac{I_R}{I_0})$ takes place. As far as the material is not transparent even absorption (A) takes place. If scattering and fluorescence is neglected the total intensity stays constant and can be described using Fresnel equations.

$$1 = T + R + A \tag{3.2-vi}$$

$$\widehat{t}_{12} = \left(\frac{E_{0T}}{E_{00}}\right) = \frac{2\widehat{n}_1 cos\widehat{\alpha}_1}{\widehat{n}_1 cos\widehat{\alpha}_1 + \widehat{n}_2 cos\widehat{\alpha}_2} \tag{3.2-vii}$$

$$\widehat{r}_{12} = \left(\frac{E_{0R}}{E_{00}}\right) = \frac{\widehat{n}_1 cos\widehat{\alpha}_1 - \widehat{n}_2 cos\widehat{\alpha}_2}{\widehat{n}_1 cos\widehat{\alpha}_1 + \widehat{n}_2 cos\widehat{\alpha}_2} \tag{3.2-viii}$$

The reflected beam I_R conserves the angle of incidence $\widehat{\alpha}_1$, while the angle $\widehat{\alpha}_2$ of the transmitted beam I_T is changed described by Snell's law. The complete process can be describe via superposition of all components.

Current Voltage Characteristics

The I-V-characteristics were measured and visualized with a LabView-controlled *Keithley* Model 2420 High-Current Source-Meter. Standard solar energy (AM1.5G) was simulated by the $WXS - 90S - 5$ by $WACOM\ ELECTRIC$ for sample illumination.

Quantum Efficiency

The spectral photocurrent can be detected depending on the incident photon energy by the usage of a monochromator. The resulting spectra is called external quantum efficiency

(EQE), or internal quantum efficiency (IQE), if the light intensity with reflection losses is regarded. Additionally a broadband halogen lamp can be used for bias light to increase the charge carrier density and the signal-to-noise ratio [67]. All EQE spectra were recorded using the lock-in technique and a chopper with a frequency of 137 Hz between the Xe light source and the monochromator. This was necessary to reduce noise and because of the bias light. Therefore the bias light does not influence the EQE spectra drastically [68]. The EQE spectra were taken with a step width of 1 nm, averaging 10 spectral points with a recording time of 200 ms each and calibrated with a silicon solar cell, certified by *Frauenhofer ISE* (see 5.1).

Chapter 4

EXCITON GENERATION

In this chapter the absorption of light in organic molecules will be discussed. At the beginning a comparison between single molecules in solution and bulk behavior in the solid states is given. After the optical investigation of the transition between two crystallographic phases the spectra are used to determine the layer thickness, the layer roughness, and the optical constants. Finally the relevance for solar cells is demonstrated.

4.1 Molecules in Solution

One of the most important processes in solar cells is the absorption of light as the absorbed photons can generate charge carriers. To understand the behavior of the complex structure it is useful to begin with a single building block. In the present case this is the absorption of a single molecule also called monomer. This can be measured in gas phase or in solvents. Due to a much easier setup the molecules were investigated in solutions. High solubility can be achieved using suitable solvents or modified molecules with side chains [69]. The latter lowers the conductivity because the separation between the single molecules is increased. To find a proper solvent a series of different saturated solutions (see Fig. 4.1 b) was performed to find a suitable one. Dimethylformamide (DMF) turned out to be a good candidate. With respect to the gas phase spectra, the solvent causes a spectral shift of the absorption because of the different dielectric environment [70] (see Fig. 4.1 a). A sharp peak, the so-called Q-band, at around 1.85 eV corresponds to the optical band gap which is linked to the HOMO-LUMO-transition (π to π^*) as described in chapter 6. In spite of the widely characterized phthalocyanines, the origin of the additional features at around 2.0 eV are still not completely understood. Possible explanations are aggregation [71], charge transfer, vibronic modes [72], or Davidov splitting [73]. Absorption at higher energy is not discussed further because it takes place in the UV region [74] (B-band ≈ 3.70 eV, N-band ≈ 5.69 eV,

C-band $\approx 5.74\,\mathrm{eV}$) which is less relevant for the optical spectrum of solar cells.
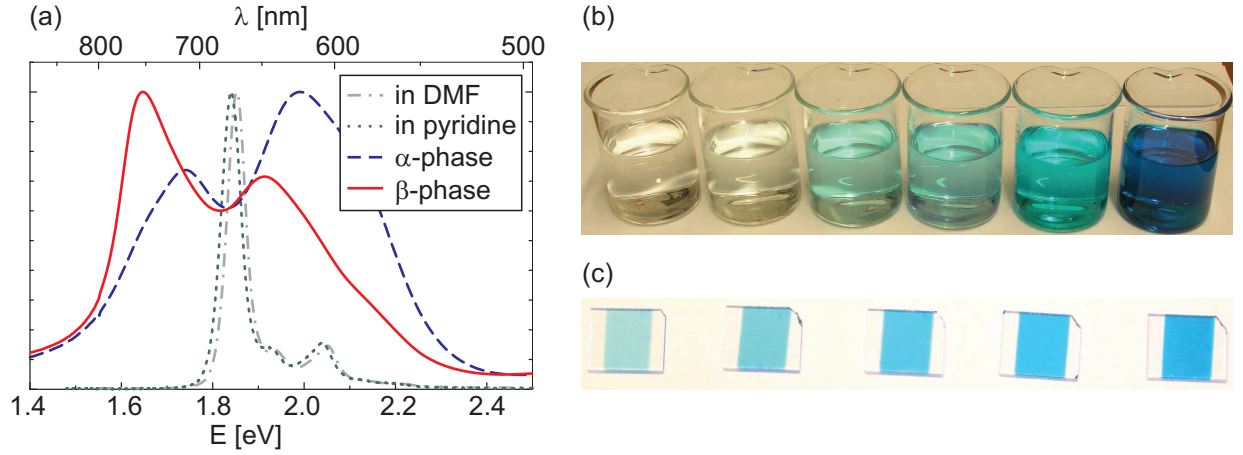
Fig. 4.1: *(a) Normalized absorbance spectra of ZnPc in two different solvents (DMF: grey dash-dotted line; pyridine: green dotted line) as well as two different phases of the bulk material (α-phase: blue dashed line; β-phase: red solid line). The sharp peak in the solution spectra stems from the monomer and the slight shift between both spectra results from the dielectric environment in different solvents. The so-called Q-band at around 1.85 eV is split in the bulk spectra compared to the solution spectra because of the interaction between the molecules. Different alignment of the molecules also results in different shapes of the Q-band. (b) Photograph of ZnPc in different solvents (water: H_2O, methanol: CH_3OH, ethanol: CH_3CH_2OH, isopropyl alcohol: $(CH_3)_2CHOH$, acetone: $(CH_3)_2CO$, dimethylformamide: $(CH_3)_2NC(O)H$) with increasing solubility. (c) Evaporated layers of the α-phase with different thicknesses ($\approx$ 30 nm, 60 nm, 90 nm, 120 nm and 150 nm).*

4.2 Common Crystal Phases and Transition

ZnPc bulk structures exist mainly either in the metastable α-phase or the stable β-phase. While α-ZnPc provides a higher conductivity [76] β-ZnPc is easily produced from solution
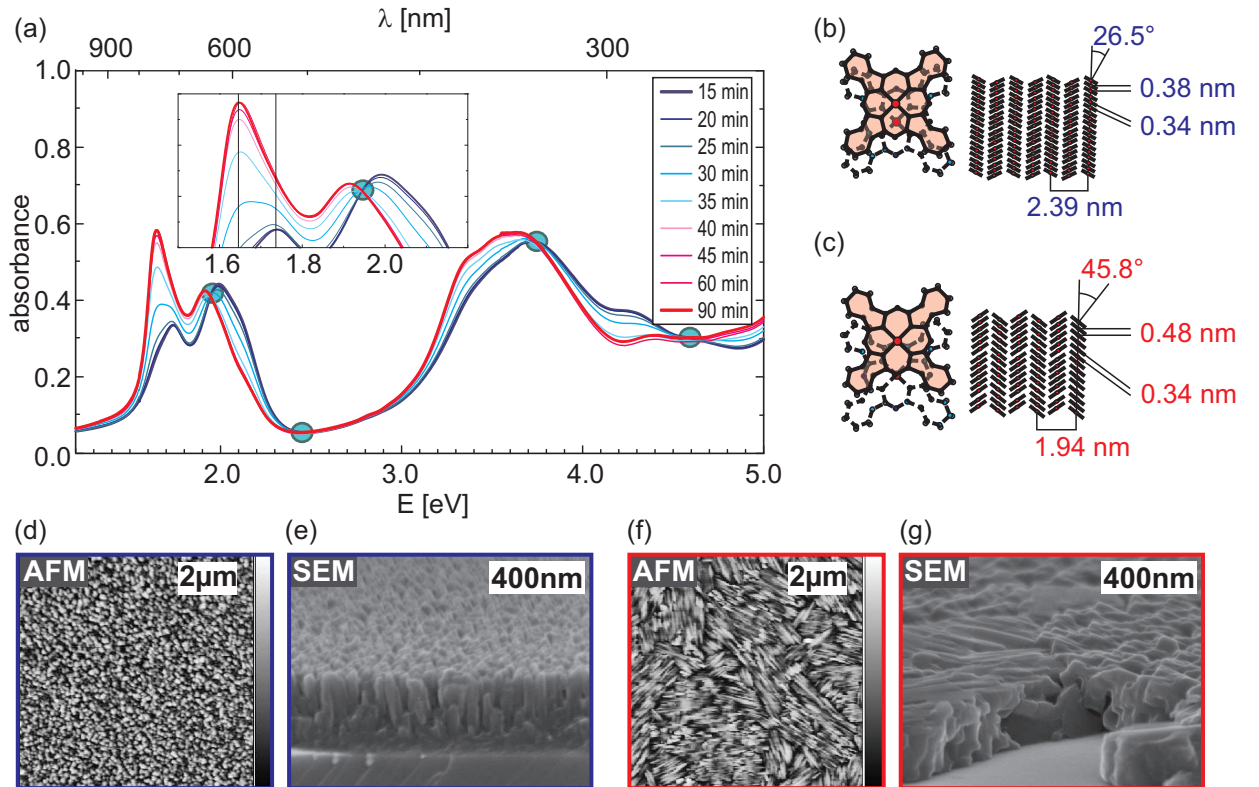
Fig. 4.2: *(a) Absorption spectra of ZnPc after annealing at 240°C at different times. The change illustrates the transition between two crystallographic phases upon annealing. Isosbestic points (marked by circles) are observed. The crystal structures of (b) α-ZnPc and (c) β-ZnPc are depicted on the right hand side [75]. AFM and SEM images of (d, e) α-ZnPc and (f, g) β-ZnPc are shown in the lower part, respectively.*

or by thermal treatment. As the α-phase is desired it is necessary to distinguish both phases which requires a thorough investigation of the structures and the transition from the α-phase to the β-phase. Obviously the lattice parameters differ. One way to discriminate both phases is to observe effects like different morphology, electric and optical behavior.

Here, the morphology was analyzed using SEM and AFM (see Fig. 4.2 d-g). α-ZnPc aggregates in clusters, whereas β-ZnPc forms a lamellar structure as already shown in [77]. The grain size of the ZnPc clusters ranges from 50 nm to 100 nm. The vertical surface

variation was calculated as root mean square roughness (R_{rms}). For the samples shown in Fig. 4.2 the R_{rms}-values are 8.5 nm and 1.2 nm for 50 nm α-ZnPc and 30 nm β-ZnPc, respectively.

The electric characteristic can mainly be seen in conductivity measurements. Thereby the orientation and distance between the molecules plays a major role [78]. Because of a closer stacking distance (α: 0.38 nm, β: 0.48 nm) α-ZnPc conducts much better [76].

The optical behavior is analyzed in terms of absorbance spectra. Compared to monomers in the gas phase or in solution, the molecules in the bulk material are much closer and so interaction of the transition dipole moments can be observed. The Q-band is split. The peak at around 1.9 eV contributes to the HOMO-LUMO (π-$\pi^\star$) transition [74]. The origin of the peak at around 1.7 eV may either contribute to an excitonic transition [79] or a vibrational interval [80]. The spectral positions of the absorbance peaks depend on the orientation and angle in between the transition dipole moments [15]. The optical behavior can be described by optical constants. Once the optical constants are known, they can be used for modeling layer systems or even photovoltaic devices, or vice versa for a non-destructive method of optical analysis of the crystallinity of ZnPc layers.

Structural analysis of α- and β-ZnPc phases and detailed information about the phase transition are needed to set suitable constraints for a numerical model to determine the optical constants of both phases. For this reason the transition is investigated in the following part. α-ZnPc samples were deposited onto substrates kept at room temperature [81]. Absorbance spectra were taken from the as deposited samples and after heating at several temperatures for various periods of time. No change in the spectra was observable at temperatures of up to 220 °C even for long term annealing (i.e., 3 h). This leads to the conclusion that the α-phase of ZnPc is stable up to ca. 220 °C. At 240 °C the crystalline transition takes place and is not instantaneous but a process of some 30 min (see Fig. 4.2 a). The annealing times were increased stepwise until the spectra remained unchanged. This could be observed after 120 min and even if the annealing time is increased to 3 h or the temperature is raised up to 300 °C no further change takes place. A coexistence of the two crystalline phases in an equilibrium, which would be temperature-dependent, can be excluded. Therefore the completeness of β-ZnPc after annealing is proven. Furthermore isosbestic points can be observed. The mere existence of those indicates that the transition

directly occurs between the two components α-ZnPc and β-ZnPc, that the total quantity of material remains constant [82], and that no third ZnPc-phase is involved.

4.3 Optical Constants and Sample Properties

Samples used for determination of optical constants were ZnPc-films of both phases with different thicknesses from 30 nm up to 150 nm. The α-ZnPc phase was obtained from deposition on substrates kept at room temperature [81] while the stable β-ZnPc phase was obtained from the metastable α-ZnPc samples via annealing under ambient conditions for 3 h at 260 °C. The films were examined with a non-contact atomic force microscope (nc-AFM) and an UV-vis spectrophotometer. The angles of incidence in the transmittance and reflectance experiments are 0 ° and 12 °, respectively. Those values are fully considered in our angle-dependent modeling. Further, the calculations were performed assuming non-polarized light, using the average from the s- and p-polarized reflectance (R) components. The measured optical spectra were analyzed by a numerical algorithm developed further and implemented by Marco Grünewald (IFK Jena) in Wolfram Mathematica 8® in order to extract the complex refractive index $\hat{n}(E) = n(E) - ik(E)$ of the thin film [83], where $n(E)$ and $k(E)$ denote the photon energy dependent refractive index and extinction coefficient, respectively. As optical model for the layer system ZnPc-quartz glass substrate the model of homogeneous layers with plane-parallel interfaces was used, however extended by an approximate consideration of the surface roughness of the ZnPc-air interface, as outlined in [84]. The determination of the optical constants is possible through a combination of transmission (T) and reflectance (R) spectra. However, here the reflectance data were replaced by differential reflectance spectra (DRS) [85–87]. Thereby, the need for a calibrated mirror can be avoided. In order to interpret the measured optical spectra of ZnPc thin films the numerical treatment is based on a layer model, consisting of the substrate (treated coherently) and the organic thin film (treated coherently) as well. We used the generalized matrix formalism based on the Fresnel formulas for mixed coherent and incoherent layers as outlined in Ref. [88]. In order to improve the layer model roughness was also considered. The interfaces were analyzed by non-contact atomic force microscopy (nc-AFM) [36]. Accordingly, the root-mean-square roughness (R_{rms}) of as-deposited as well as annealed films of ZnPc was found to be small but not insignificant with respect to the film thickness d_j ($R_{rms}/d_j < 20\%$ for α-ZnPc and $R_{rms}/d_j < 5\%$ for β-ZnPc). Hence, for an accurate determination of the optical constants the values obtained for the surface roughness at the

air-to-ZnPc interface have to be taken into account. This was done by modified Fresnel co-
efficients considering only partial coherence due to phase differences of the transmitted and
reflected beams by Gaussian distributed irregularities as outlined in Ref. [84]. Because of
the evenly distributed azimuthal orientation of the grains or needles the in-plane component
of the optical anisotropy can be neglected. The substrate was treated as incoherent due to
its rather large thickness (0.63 mm) with respect to the coherence length of the light. This
means that we indeed account for multiple reflections at both substrate interfaces but in-
ternal interference effects do not contribute to the signal. An optical characterization of the
quartz glass substrate used was done by transmission measurements in the UV, visual, and
near infrared spectral region in order to extract the refractive index individually assuming
negligible absorption ($k = 0$). As a matter of fact no dispersion model for ZnPc is required.
Accordingly, the algorithm starts with a set of optical constants, i.e., the refractive index
$n(E_1, ..., E_i, ..., E_N)$ and the extinction coefficient $k(E_1, ..., E_i, ..., E_N)$, each consisting of N
points to be fitted to the experimental data. In this work, the energy interval from 1.2 eV
to 5.0 eV with a step size of 0.01 eV results in an N of 381. If only one pair of transmis-
sion and differential reflectance spectra is used for the extraction of the optical constants n
and k, then the film thickness needs to be specified precisely to prevent the algorithm to
produce large errors in the optical constants or even to get stuck in a non-physical solu-
tion. To overcome this issue, the optical data of several samples are analyzed in parallel, as
suggested in [89]. Consequently, five samples with estimated thicknesses of 30 nm, 60 nm,
90 nm, 120 nm and 150 nm, respectively, were measured (estimated thicknesses determined
with a quartz crystal microbalance). Now, the numerical fit is carried out simultaneously
over five pairs of DRS and T spectra, with the constraint of using the same values for the
extinction coefficient $k(E_i)$ and refractive index $n(E_i)$ for all spectra.

$$\sum_j \sum_{i=1}^{N} A(E_i, d_j) \left\{ DRS_{\text{th}}(n(E_i), k(E_i), d_j, R_{rms}) - DRS_{\exp}(E_i, d_j) \right\}^2$$

$$+ \sum_j \sum_{i=1}^{N} A(E_i, d_j) \left\{ T_{\text{th}}(n(E_i), k(E_i), d_j, R_{rms}) - T_{\exp}(E_i, d_j) \right\}^2$$

$$\xrightarrow{n,k,d,R_{rms} \text{ variation}} \min \qquad (4.3\text{-i})$$

T_{th} and DRS_{th} denotes the calculated quantity to be fitted to the experimental data $T_{\exp}$
and $DRS_{\exp}$, respectively. The index j is used to distinguish between the different samples

with different thicknesses. Each signal of T and DRS was weighted by a factor $A\left(E_i, d_j\right)$ as described in [90] in order to equalize the information from all spectra, having originally different magnitudes. $A\left(E_i, d_j\right)$ is calculated from the minimal ($n = 1$, $k = 0$) and maximal ($n = 3$, $k = 1$) values of the refractive index and extinction coefficient expected for phthalo-cyanine thin films [89]. Due to the mathematical over-determinateness of the system, the layer thicknesses d_j can be optimized as well, using the estimated thicknesses as starting values. Likewise, the R_{rms}-values were treated as fitting parameters (results are shown in Tab. 4.1). The fit itself was carried out by means of a Levenberg-Marquardt-algorithm, which is known to be rather robust against different starting values.

Tab. 4.1: *Nominal and optimized values of film thickness and rms-values of the samples used for the determination of optical constants. The errors given are statistical errors from the fitting procedure.*

	α-ZnPc		β-ZnPc	
estimated thickness	optimized thickness	R_{rms}	optimized thickness	R_{rms}
[nm]	[nm]	[nm]	[nm]	[nm]
30	36.95±0.03	1.1±0.3	36.15±0.05	-
60	65.30±0.04	3.1±0.2	61.90±0.07	5.4±0.2
90	96.63±0.04	7.7±0.1	94.65±0.08	4.5±0.1
120	132.15±0.05	10.6±0.1	129.09±0.07	5.9±0.1
150	168.90±0.07	13.2±0.1	167.88±0.07	5.6±0.1

Next, we want to discuss the results of the fitting procedure. As apparent from Tab. 4.1, the numerically determined thickness values are somewhat higher than the estimated ones for each sample. A possible reason for this deviation may be found in the calibration (incorrect tooling factor) as well as thermal drift of the quartz oscillator. However, the reliability of the numerical thickness values is emphasized because the small difference between α- and β-phase of the same sample is systematic and can be explained by changes in the material density (1.60 $\mathrm{g/cm^3}$ versus 1.62 $\mathrm{g/cm^3}$ [91]). The fitted R_{rms}-values of α-ZnPc samples increase with film thickness. In contrast, all the samples of β-ZnPc show a uniform R_{rms}-value of about 5 nm. This seems characteristic for an annealed β-ZnPc surface. The numerically calculated R_{rms}-values are in very good agreement with those from our own nc-AFM images (see Fig. 4.2) and those presented in [91]. In Fig. 4.4 the resulting spectra of the optical
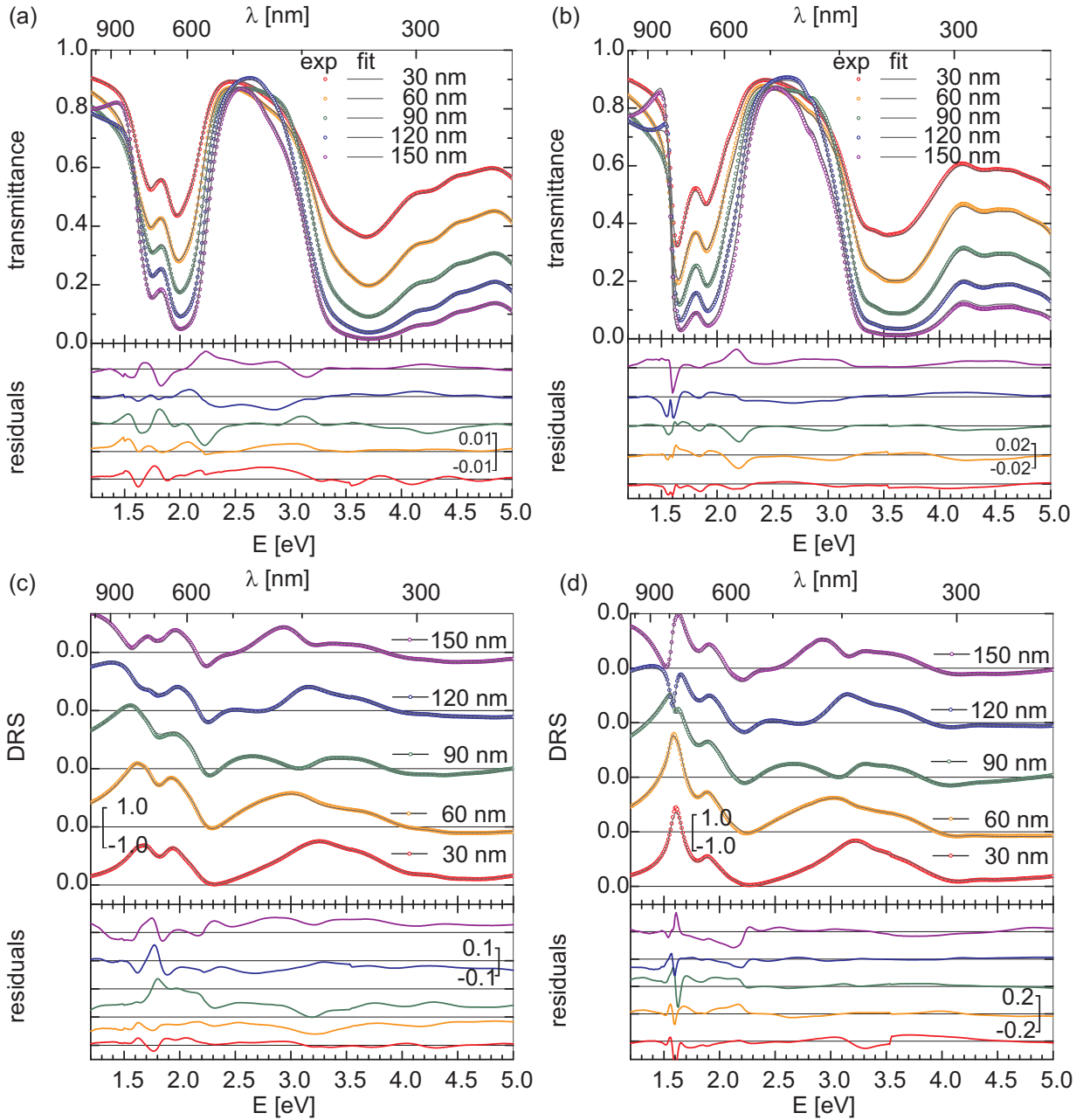
Fig. 4.3: *Experimental dataset (open symbols) consisting of five samples of α-ZnPc (a, c) and five samples of β-ZnPc (b, d) with various estimated thicknesses (given in the graphs), characterized by one transmittance curve (a, b) and one DRS (c, d) each, and the curves which where fitted with a single set of optical constants used for all layer thicknesses (solid line). In the lower part the residuals (difference of experimental and simulated value) of the fitting process are shown. For the sake of clarity subsequent residual spectra and DRS are displayed with a vertical offset. The insets show the respective scale bars.*
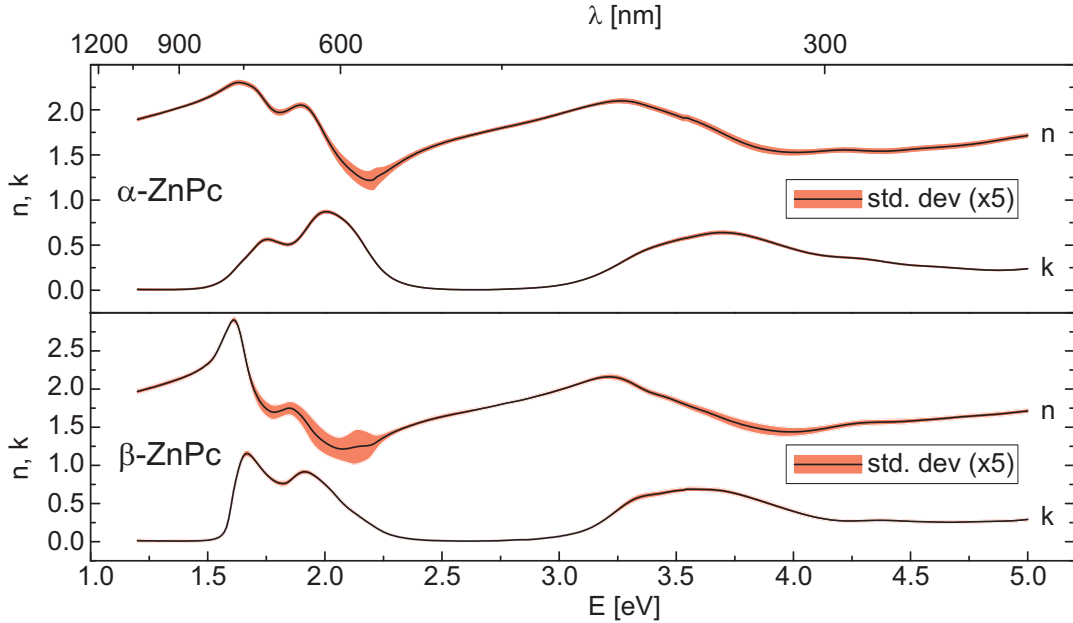
Fig. 4.4: *Spectra of refractive index n and extinction coefficient k of α- (top) and β- (bottom) ZnPc, respectively. The standard deviation (statistical errors from the fitting procedure, magnified by a factor of 5) is indicated by the reddish error margin.*

constants for α-ZnPc and β-ZnPc are shown. As one can see, the residuals are very small compared to the transmission data. The edge at $350\,\mathrm{nm}$ ($3.54\,\mathrm{eV}$) is caused by the internal light source changeover of the spectrophotometer used but is smaller than the mean residuals and therefore has no significant influence. During calculation no constraint was set for the Kramers-Kronig relation but model-free Kramers-Kronig consistence in a restricted spectral region covering $1.2\,\mathrm{eV}$ to $2.6\,\mathrm{eV}$ (by splitting the respective integral as outlined by Nitsche *et al.* [92]) was confirmed afterwards as an independent verification of reliability of the optical constants. It should be noted that by this set of optical constants the measured optical spectra can be reproduced very nicely (see fig. Fig. 4.3). If the surface roughness is neglected, slightly different optical constants, especially in the ultraviolet spectral region, are obtained, which results in a less suitable fit of the optical data.

Some reports on the optical constants of ZnPc already exist [74, 79, 93]. Those results conflict with each other. In general, it has to be pointed out that the data presented in the three papers mentioned are apparently not Kramers-Kronig consistent between refractive index n and extinction coefficient k, and can therefore not be regarded as reliable sets of optical data for zinc(II)-phthalocyanine. In contrast, the data presented here of α-ZnPc were

compared with those of the almost identical molecule copper(II)-phthalocyanine (CuPc, α-phase) from [89, 94] and are in good agreement.

4.4 Enhanced Photon Absorption by Nanowires

Nanowires of the size of the wavelength of the absorbed light lead to scattering effects which can be seen in an increased featureless background in the optical spectra. This leads to a longer pathway of the photons inside the device. Nanowires also allow to increase the light absorption length (parallel to the nanowires) while keeping the thickness of the device interface (perpendicular to the nanowire) constant. The advantage for solar cells will be discussed in section 7.4.

Chapter 5

EXCITON DIFFUSION

After the generation by light absorption the exciton can diffuse before it recombines or dissociates. By investigating the photocurrent with spectral resolution the diffusion length and also the generation position can be determined, which is described in this chapter.

5.1 Quantum Efficiency Spectra

Light absorption in organic molecules leads to exciton generation as described in the previous chapter. In contrast to inorganic semiconductors, excitons have a quite high binding energy which is why they do not readily dissociate even at elevated temperatures. A high electric field which has to drop off over a very short range because of the small binding radius has to be applied. These conditions can be found only at an abrupt interface. For this reason, excitons, generated in organic materials at a certain distance from the interface, will have to diffuse. The length at which the exciton concentration is dropped down to $^1/_e$ due to recombination, is called exciton diffusion length (L_{diff}^{exc}). If they reach the desired p-n-junction within the diffusion length, which is regarded as energy independent in this chapter, the excitons dissociate into free charge carriers which can be measured as photocurrent. This can also be done depending on the energy of the impinging photon. Normalized to the amount of photons this is called the external quantum efficiency (EQE). The setup with a Xe-lamp was calibrated using a silicon solar cell characterized independently by the Fraunhofer Institute for Solar Energy Systems ISE (see Fig. 5.1 center). The EQE measurements were performed with devices consisting of a p-n-junction while the p-type material was ZnPc and the n-type semiconductor the inorganic ZnO or CdS. ZnPc is known to be p-type under atmospheric treatment by simple oxygen intercalation [96]. ZnO is used because of the natural affinity to be n-type because of oxygen vacancies and zinc interstitials [97]. It also possesses a quite high exciton binding energy compared to other inorganic materials such
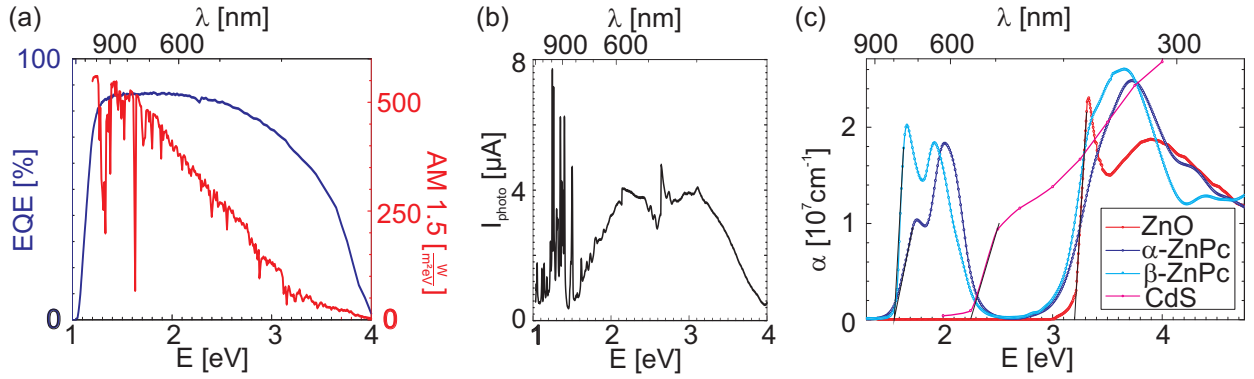
Fig. 5.1: *(a) EQE of a calibrated Si solar cell (blue) and the spectrum of the sun (red) also known as AM1.5 [95]. (b) The spectrum of the EQE light source is measured in terms of photocurrent with the Si solar cell. (c) Absorbances of the inorganic (reddish) and organic (blueish) components. It can be clearly seen that optical gap of ZnPc is smaller than the gap of ZnO as well as that of CdS.*

as CdS [97]. For comparison CdS was used whose bandgap is lower than that of ZnO but still larger than ZnPc (see Fig. 5.1 c: CdS: 2.4 eV, ZnO: 3.2 eV, ZnPc: $\approx$1.6 eV). This allows to use photons with higher energy for charge generation. ZnO and CdS are already used in photovoltaics and it is possible to grow nanowires from these materials which may enhance the performance.

The EQE of ZnO-ZnPc hybrid solar cells (see Fig. 5.2 a) has a spectral shape similar to the absorbance spectrum of α-ZnPc (see Fig. 5.1 c). Especially the features in the range between 1.55 eV and 2.25 eV can be linked to the organic part. It is not clear whether the current generated in the UV region is correlated to the energy gap of ZnO or the B-band of ZnPc. Samples with an increased ZnO layer thickness (not shown here) show a higher EQE signal in the UV region. Hence, it is assumed, that high energetic photons generate charge carriers in ZnO. However, since the solar intensity decreases rapidly in this region, these charge carriers play a minor role in the photocurrent (see Tab. 5.1). Taking a closer look at the shape of the EQE within the ZnPc region, i.e., 1.55 eV to 2.25 eV, one can observe a slight decrease of the photocurrent with increasing ZnPc layer thickness. This may be the case if the ZnPc-ZnO interface is the exciton dissociation area as assumed. Due to the fact that organic materials typically exhibit an inferior cunductivity [98] as compared to inorganic materials, the distance to the collecting electrode increases with increasing ZnPc layer thickness. A very thin Au cathode was used to give the ability to illuminate the cell
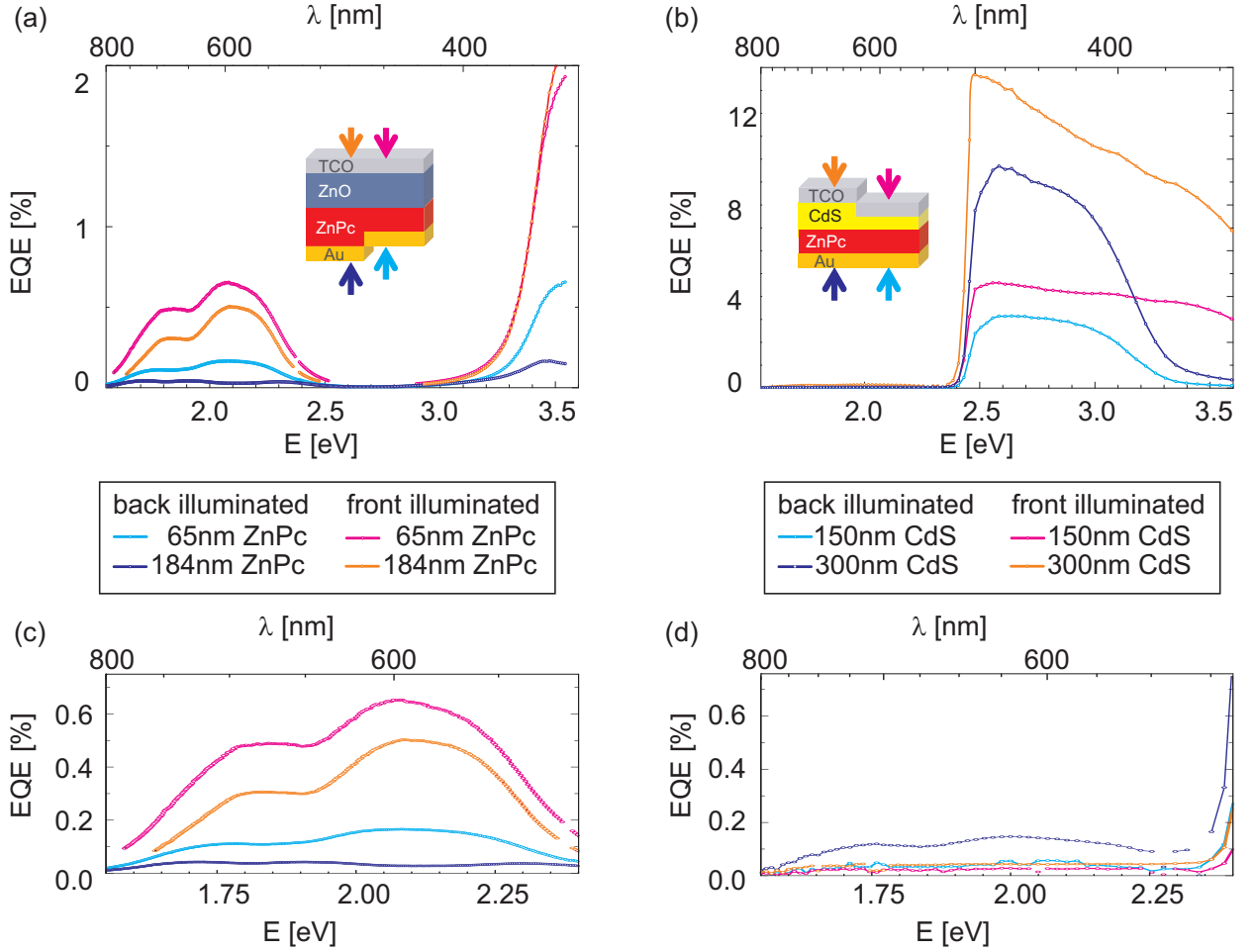
Fig. 5.2: *EQE spectra of hybrid solar cells (a, c) with 50 nm ZnO and different ZnPc thicknesses and (b, d) 150 nm ZnPc with different CdS thicknesses. The samples were illuminated from the front (as designed through the TCO) and from the back (through the cathode) side, which results in the internal filter effect. The illumination direction is shown in the insets by arrows of corresponding color.*

from the "back" side, i.e., through the Au layer. A drastic decrease can be observed which can be explained by the lower transmission of Au. Another explanation for this phenomena is the absorption of photons, i.e., generation of excitons, far away from the separating interface. In other words, the excitons have to be generated close to the separating ZnO-ZnPc interface which would be the case by illumination from the TCO-ZnO side or by illumination through Au and a very thin ZnPc layer. The effect of photon absorption and recombination of the generated excitons before dissociation is called internal filter effect [99]. The corresponding photon is lost without contributing to the photocurrent. This can be seen in the curves because at the position of absorbance maxima (1.8 eV and 2.1 eV) local minima can be

Tab. 5.1: *Photocurrent of different device setups containing ZnO derived from EQE spectra. The photocurrent is spectrally divided into the region 1.55-2.25 eV which is mainly influenced by ZnPc, and 2.25-3.54 eV which also shows the contribution of the inorganic compound because of the band gap (ZnO: 3.4 eV). The arrows mark the direction in which the photons pass the layers. P symbolizes an additional spin coated PEDOT layer.*

thickness [nm]			photocurrent $\left[\frac{mA}{cm^2}\right]$		
ZnO		ZnPc	j (1.55-2.25 eV)	j (2.25-3.54 eV)	j (1.55-3.54 eV)
50	$\rightarrow$	56	0.076	0.024	0.100
50	$\leftarrow$	56	0.030	0.010	0.040
50	$\rightarrow$	62	0.075	0.021	0.096
50	$\leftarrow$	62	0.024	0.008	0.032
50	$\rightarrow$	65	0.088	0.024	0.112
50	$\leftarrow$	65	0.026	0.008	0.034
50	$\rightarrow$	157	0.041	0.076	0.117
50	$\leftarrow$	157	0.007	0.016	0.023
50	$\rightarrow$	184	0.072	0.022	0.094
50	$\leftarrow$	184	0.010	0.004	0.014
50	$\leftarrow$	50+P	0.062	0.088	0.150
silicon solar cell			15.27	7.41	22.68

observed in the EQE. This effect is thickness dependent and appears just for thick layers. As the entire spectral shape of the EQE depends only on the optical constants, the thickness, and the exciton diffusion length, the last parameter can be determined (see section 5.2) as the first two are already known from the previous chapter. An additional layer of PEDOT which will be important for nanostructures (see section 7.4) shows no influence in the ZnPc region but an increase in the photocurrent in the UV range, which can be explained because of the absorption of PEDOT itself.

In contrast to hybrid solar cells with ZnO, the shape of the EQE of cells with CdS are mainly determined by the shape of the absorption of CdS (see Fig. 5.2 b). Ont the one hand the absolute values are larger, but even if the ZnPc region is scaled to match the ZnO devices (see Fig. 5.2 d) the contribution of the α-ZnPc is very weak. By illumination from the back side, i.e., through Au and ZnPc, a decrease in the EQE signal in the UV range can be observed, which could be caused by the B-band absorption of ZnPc. This leads to the

assumption that photons are absorbed within the ZnPc layer but the generated excitons do not dissociate and contribute to the photocurrent. The results can also be seen in Tab. 5.2. A possible explanation for the photocurrent in the higher energetic region would be that there is a band bending in the CdS layer which leads to the photocurrent coming from the inorganic CdS, while in ZnO the band bending is much weaker. This is confirmed by hybrid

Tab. 5.2: *Photocurrent of different device setups containing CdS derived from EQE spectra. The photocurrent is spectrally divided into the region 1.55-2.25 eV which is mainly influenced by ZnPc, and 2.25-3.54 eV which is mainly influenced by the inorganic compound because of the band gap (CdS: 2.4 eV). The arrows mark the direction in which the photons pass the layers. P symbolizes an additional spin coated PEDOT layer.*

| thickness [nm] | | | photocurrent $[\frac{mA}{cm^2}]$ | | |
CdS		ZnPc	j (1.55-2.25 eV)	j (2.25-3.54 eV)	j (1.55-3.54 eV)
150	$\rightarrow$	54	0.019	1.109	1.128
150	$\rightarrow$	71	0.038	2.110	2.148
150	$\rightarrow$	142	0.054	3.202	3.256
300	$\rightarrow$	38	0.006	0.538	0.544
300	$\leftarrow$	38	0.004	0.514	0.518
300	$\rightarrow$	72	0.019	1.242	1.261
300	$\leftarrow$	72	0.003	0.863	0.866
300	$\rightarrow$	129	0.019	0.788	0.807
300	$\leftarrow$	129	0.006	0.498	0.504
300	$\rightarrow$	129+P	0.019	1.995	2.014
300	$\leftarrow$	129+P	0.011	1.559	1.570
silicon solar cell			15.27	7.41	22.68

solar cells with larger CdS layer thickness which do not reach a similarly high photocurrent as for cells with thinner CdS layers. If the layer thickness is much larger than the width of the band bending, no preferred charge transport direction is formed. Another reason could be the higher exciton binding energy of ZnO (60 meV) which effectively reduces the number of free charge carriers. Similar to the ZnO devices the PEDOT layer just improves the performance in the UV region.

5.2 Exciton Diffusion Length

As mentioned in section 2.2.2 the exciton diffusion efficiency η_{diff}^{exc} plays a crucial role. It depends on the layer thickness d and the exciton diffusion length L_{diff}^{exc}.

$$\eta_{diff}^{exc} = e^{-d/L_{diff}^{exc}} \tag{5.2-i}$$

$$L_{diff}^{exc} = \sqrt{D^{exc}\tau^{exc}} \tag{5.2-ii}$$

The thinner the absorbing layer (small d) the higher the number of excitons reaching the separating p-n-junction. This is in contrast to the light absorption which is increased for thick layers. The exciton diffusion length is determined by the diffusion constant D^{exc} and the lifetime τ^{exc}. Therefore it can be regarded as material constant but can be influenced by the sample properties such as grain boundaries. Close to the p-n-junction there is an electric field which can break the exciton in locally separated charges under proper conditions (see section 6.3) with the efficiency η_{diss}^{exc}. Thus the amount of excitons can be calculated from the single processes using Fick's second law of diffusion [100]:

$$\frac{\partial N^{exc}}{\partial t} = \underbrace{D^{exc} \cdot \frac{\partial^2 N^{exc}}{\partial z^2}}_{\text{diffusion}} - \underbrace{\frac{N^{exc}}{\tau^{exc}}}_{\text{recombination}} + \underbrace{\eta \cdot \phi_0 \cdot e^{-\alpha \cdot z}}_{\text{generation}} \tag{5.2-iii}$$

In principle this describes the change of the local exciton density N^{exc} with time t as combination of excitons moving away (diffusion), excitons terminated (recombination) and excitons which are created (generation). The generation is done by photon absorption and can be described in good approximation by Lambert-Beer law with a photon intensity ϕ_0, photon absorption efficiency η, and the absorption coefficient α. Under steady state conditions and the boundary conditions (BC) of eliminated excitons at the border of the active layer with the thickness d, it leads to:

$$\frac{\partial N^{exc}}{\partial t} = 0 \qquad\qquad\qquad steady\ state \tag{5.2-iv}$$

$$N^{exc} = 0 \qquad\qquad\qquad BC: z = 0 \cup z = d \tag{5.2-v}$$

$$D^{exc} \cdot \frac{\partial^2 N^{exc}}{\partial z^2} = \frac{N^{exc}}{\tau^{exc}} - \eta \cdot \phi_0 \cdot e^{-\alpha \cdot z} \tag{5.2-vi}$$

The interfaces are also regarded to be smooth. The solution of this second order differential equation with $\beta = 1/L_{diff}^{exc}$ (for simpler formulas) yields:

$$N^{exc}(z) = \frac{\alpha \cdot \phi_0 \cdot \eta}{D^{exc} \cdot (\beta^2 - \alpha^2)} \cdot \left\{ \frac{(e^{\beta d} - e^{-\alpha d})e^{-\beta z} - (e^{-\beta d} - e^{-\alpha d})e^{\beta z}}{e^{-\beta d} - e^{\beta d}} + e^{-\alpha z} \right\} \tag{5.2-vii}$$
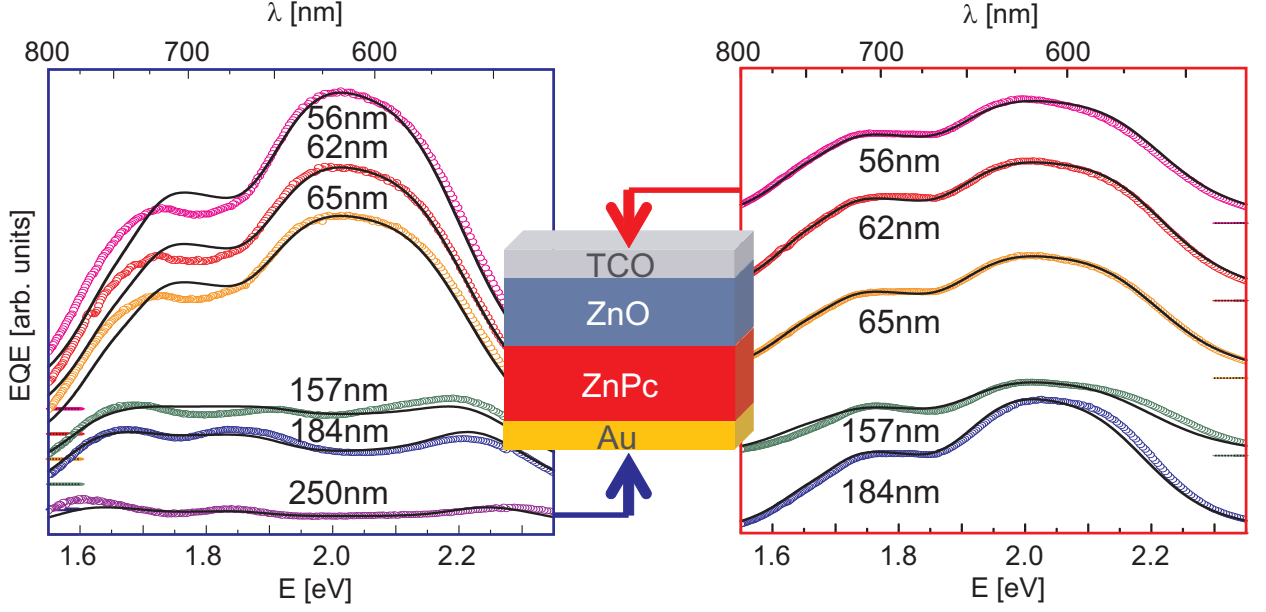
Fig. 5.3: *Experimental (open symbols) and simulated (solid lines) external quantum effi-
ciencies (EQE) in the visible spectral region. The curves are vertically shifted
(offset indicated by short horizontal lines). For back illumination (left) minima
occur which are correlated to the internal filter effect. For front illumination
(right) the shape is similar to the Q-band of the absorption spectra of ZnPc.
The color of the graph represents different thickness of the ZnPc layer while
keeping the other layers constant (Au: 10 nm, ZnO: 200 nm, ITO: as delivered).*

Considering the exciton current (I^{exc}), derived by Fick's first law, to be proportional to the
photocurrent leading to the EQE, the shape of the EQE can be simulated depending on the
thickness d, the absorbance α and the exciton diffusion length L_{diff}^{exc}.

$$EQE\left(\alpha\left(E_i\right), \beta_j, d_j\right) \propto I^{exc} = -D \cdot \frac{dN(z)}{dz} \tag{5.2-viii}$$

Hence, six samples with different ZnPc thicknesses (56 nm, 62 nm, 65 nm, 157 nm, 184 nm,
250 nm) were prepared and the EQE spectra from both illumination directions were recorded
(see Fig. 5.3). The substrate was borosilicate glass with ITO as delivered with a 50 nm ZnO
layer and a 10 nm Au back electrode. Similar to the determination of the optical constants
the minimum of the squared differences of the experimental and the theoretical EQE is fitted
for all samples simultaneously.

$$\sum_j \sum_{i=1}^{N} \left\{A\left(d_j\right) \cdot EQE_{\text{th}}\left(\alpha\left(E_i\right), \beta_j, d_j\right) - EQE_{\text{exp}}\left(E_i, d_j\right)\right\}^2 \xrightarrow{\text{vary } A, \beta_j} \min \tag{5.2-ix}$$

The factor $A\left(d_j\right)$ plays a minor role, as it just normalizes the intensity and contains no information on the shape of the EQE. The intensity is influenced by the real active area, the conversion efficiency of photon-to-exciton and exciton-to-charge carrier, defects which leads to losses of the current, and the illumination intensity. Knowing d and α from optical experiments (see section 4.3) the only missing parameter is the exciton diffusion length. The best result for the curves Fig. 5.3 in section 5.1 are obtained for an exciton diffusion length of 16 nm (statistical error less than 0.1 nm). This is in good agreement with estimations for ZnPc of other groups (e.g., 15 nm [101], 10 nm [102], 7 ± 3 nm [103]) and typical exciton diffusion length of other organic materials [104]. The shape including the minima from the internal filter effect can be reproduced very well. Thin layers show a small difference for back illumination between the simulated and the measured curve. Possible reasons can be the neglect of roughness, exciton reflection or dissociation at the ZnPc-Au interface.

Chapter 6

EXCITON DISSOCIATION

The exciton dissociation is caused by the electronic structure which is expressed in terms of internal fields and band bending at the interface. Hence, at the beginning of this chapter the electronic structure is derived from UPS. The resulting band structure is discussed in the view of solar cell performance, and characteristic parameters for photovoltaics are estimated.

6.1 Band Structure of the Device

The exciton dissociation at the interface was confirmed by the EQE spectra. However, it is necessary to investigate the electronic band structure to understand the driving forces for exciton dissociation and charge transport. Possible methods are scanning tunneling spectroscopy (STS), capacitance-voltage measurements (CV), and ultra-violet photoelectron spectroscopy (UPS), for example. STS is laterally resolved and gives the local density of states (LDOS) close to the Fermi energy [105]. Using CV the space charge region is changed by the applied voltage and can be used to calculate the band bending via carrier concentration [106–108]. UPS gives information on occupied states only, i.e., below the Fermi energy, and is limited to photoelectrons stemming from the proximity of the surface due to their mean free path of typically a few nanometers. This leads to a crucial influence of surface contamination [14, 109]. On the other hand, it is possible to investigate the development of the valence structure and the vacuum level with respect to the Fermi energy through a whole device by building it up layer by layer with measurements after each single step. In this work this was performed by UPS analyses. Besides the surface contamination, the interaction between adjacent layers also has to be taken into account. Intercalation, chemical reaction and dipole generation can occur [24]. Intercalation of metal atoms into organic films has been observed quite frequently [110–112]. Therefore, all samples investigated by means of UPS were produced by depositing the organic material onto inorganic substrates and

not vice versa. Gold (Au) is a widely characterized metal. For this reason it was used as reference sample as well as cathode material as it exhibits a quite high workfunction. Neglecting dipoles, the interface to a lower workfunction material leads to downward band bending (assuming Fermi level alignment), i.e., electrons would drift away from the Au while holes tend to drift towards the Au.

While exciting the sample with HeI (21.2 eV) as well as HeII (40.8 eV) it is possible to calibrate all spectra with the Fermi edge of Au as it was placed on the sample holder for each measurement. The multi channel analyzer was calibrated with the 21.2 eV and 40.8 eV UV excitations for the highest kinetic energy E_{kin} of the electrons. An energy step size of 30 meV was set, which is sufficient as the UV light source gives a spectral resolution of 130 meV only.

The UPS measurements can be divided into three regions. The low kinetic energy region between 2 eV and 6 eV (see Fig. 6.1 a) can be used to determine the workfunction. All UPS spectra show a background created by secondary electrons which were inelastically scattered in the sample material. Hence the background increases towards lower kinetic energy until it drops down abruptly. This low kinetic energy cut off (LKEC) is caused by the workfunction either of the sample or the detector, because the electrons do not have enough energy to reach the vacuum level or to overcome the barrier from the vacuum level to the detector. As a bias potential is applied which is much larger than the detector's workfunction, the LKEC can be correlated to the workfunction of the sample. In the present case the workfunction is 4.2 eV. In the literature Au shows a much higher value (≈ 5.2 eV) depending on crystallinity and orientation [113]. The difference can be explained by contamination [14] when taking the sample to atmosphere during the transfer between the different coating systems. The two high kinetic energy regions between 12 eV and 22 eV (see Fig. 6.1 b) and between 30 eV and 41 eV (see Fig. 6.1 c) correspond to the low binding energy region for HeI and HeII, respectively. Similar to literature results well pronounced $5d$ and weak $6s$ features of Au can be seen.

By evaporating ZnPc onto Au a small and continuous downwards shift can be observed for the workfunction (see Fig. 6.1 a). A jump from Au to the first ZnPc layer could be observed by other groups which was linked to surface dipoles [114, 115]. The absence in the spectra discussed here can be explained by the possible contamination of Au which
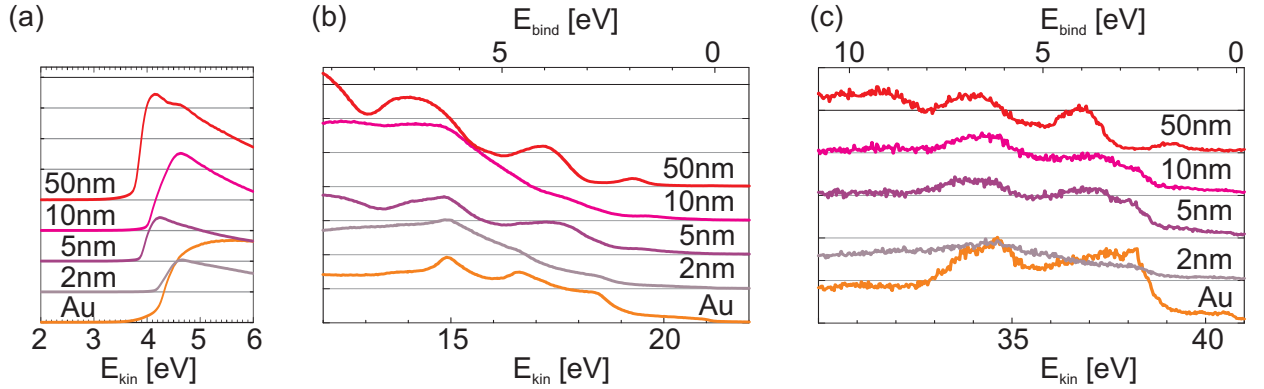
Fig. 6.1: *(a) The low energy cutoff of the UPS is shifted continuously to lower energies on Au substrates which can be correlated to a decrease of the workfunction. Au as metal shows occupied states up to the Fermi energy ($E_{bind} = 0eV$) which mark the position of the photon energy of the excitation and were used to calibrate the energy scale. In (b) the HeI and (c) the HeII region, the HOMO of ZnPc can be observed at a binding energy of 1.4 eV (upper scale) and shifts to a value of 1.6 eV which is typical for bulk ZnPc. The HeII intensity is much weaker compared to the HeI for which reason the signal-to-noise ratio is smaller.*

were already mentioned for the Au spectrum. At low binding energy (see Fig. 6.1 b and c) new features arise which belong to ZnPc. The HOMO is located at 1.4 eV for thin layers and shifts to 1.6 eV for thick layers which is in good agreement with bulk ZnPc [115]. The downward shift of the HOMO and vacuum level are good conditions for electron injection in or hole extraction from ZnPc to Au. The intensity of the gold and the HOMO-1 compared to the HOMO is stronger in the HeII signal because the higher energy of HeII excites states correlated to heavier elements. The HOMO is generated by the π-orbital of the aromatic framework with influence of the nitrogen while the central Zn-atom also influences the HOMO-1 [116].

In the device also PEDOT is used, which fulfills different purposes. It is spin coated on ZnPc to reduce metal intercalation while depositing Au. By solution processing it decreases the roughness and fills the pores in nanostructured samples. Furthermore, PEDOT is used as an electron blocking layer (EBL) between ZnPc and Au because of the high workfunction and electron affinity. In the UPS spectrum the workfunction shows a step structure (see Fig. 6.2 a). This could be caused by PEDOT which partially covers the Au layer in a way that the workfunction of Au (4.2 eV) is measured in addition to the workfunction of PEDOT (4.6 eV). Therefore the LKEC is the summation of both features. With reference
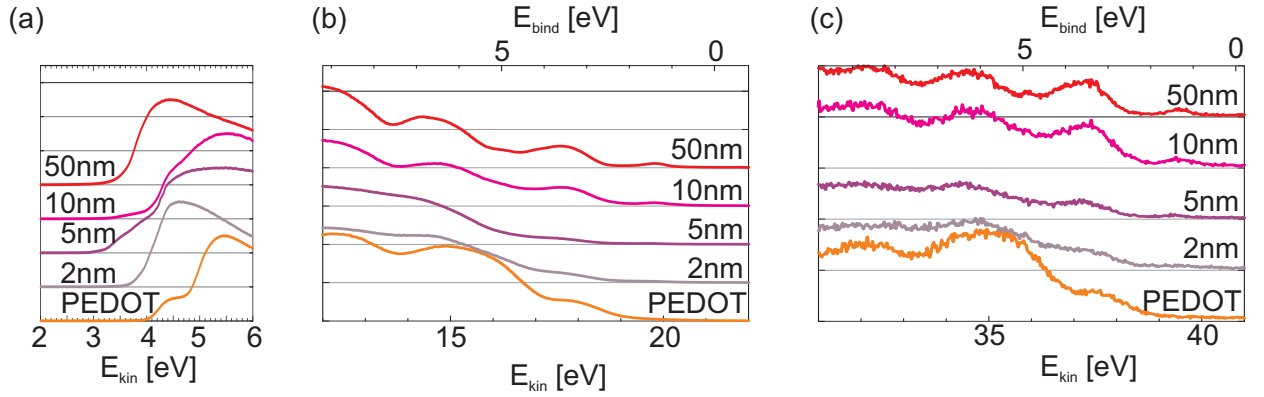
Fig. 6.2: *(a) The cutoff at low kinetic energy in the PEDOT spectrum shows a step which could be caused by a partial coverage of the Au sublayer. The shift to lower energies can be correlated to a decrease of the workfunction. (b, c) The HOMO of ZnPc can be observed at 1.6 eV.*

to this lower energetic data point the workfunction of the ZnPc layers are shift downwards. Assuming the higher value for PEDOT an interface dipole could be developed. The fixed HOMO position at 1.6 eV also confirms this effect (see Fig. 6.2 b and c). Nevertheless the direction of the dipole as well as the direction of band bending would promote the desired electron injection or hole extraction.
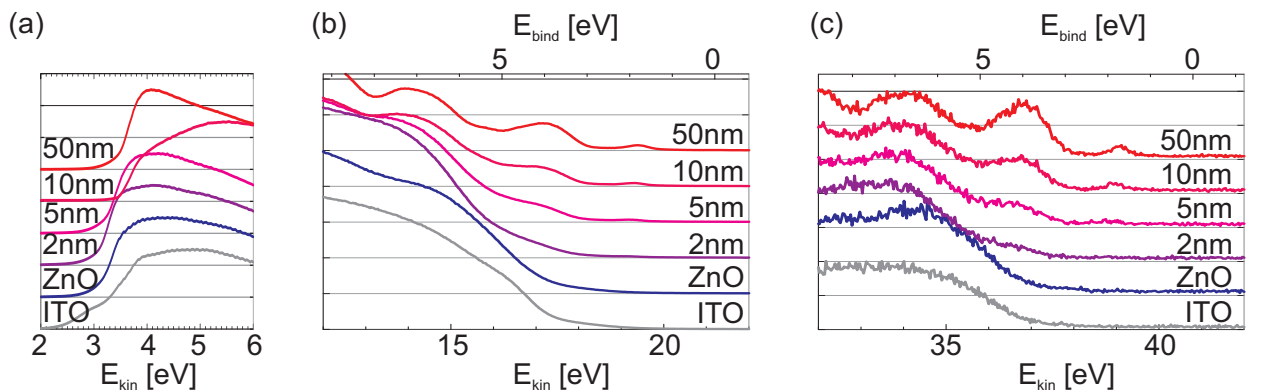
Fig. 6.3: *(a) In the low kinetic energy region a continuous shift of the secondary electron cutoff towards higher energy can be observed with increasing ZnPc thickness. This can be correlated to an increase of the work function. In the (b) HeI and (c) HeII region the HOMO of ZnPc can be observed at a binding energy of 1.8 eV (upper scale) and shifts to a value of 1.6 eV which is typical for bulk ZnPc.*

Building up the sample from the other side starting with borosilicate glass covered with as-delivered ITO shows a much lower workfunction (around 3.1 eV see Fig. 6.3 a). The workfunction of ITO can cover a wide energy range depending on the treatment. The LKEC

is quite broad and shows no sharp edge, which can be caused by a variety of workfunctions. A possible reason can be the surface roughness. ITO is well known to exhibit needle structures on the surface. Such sharp features tend to emit electrons much easier than valleys for example, where electrons with low energy are reabsorbed. Easier emission can be detected as lower workfunction. On top of the ITO, ZnO layers with various thicknesses (50 nm,
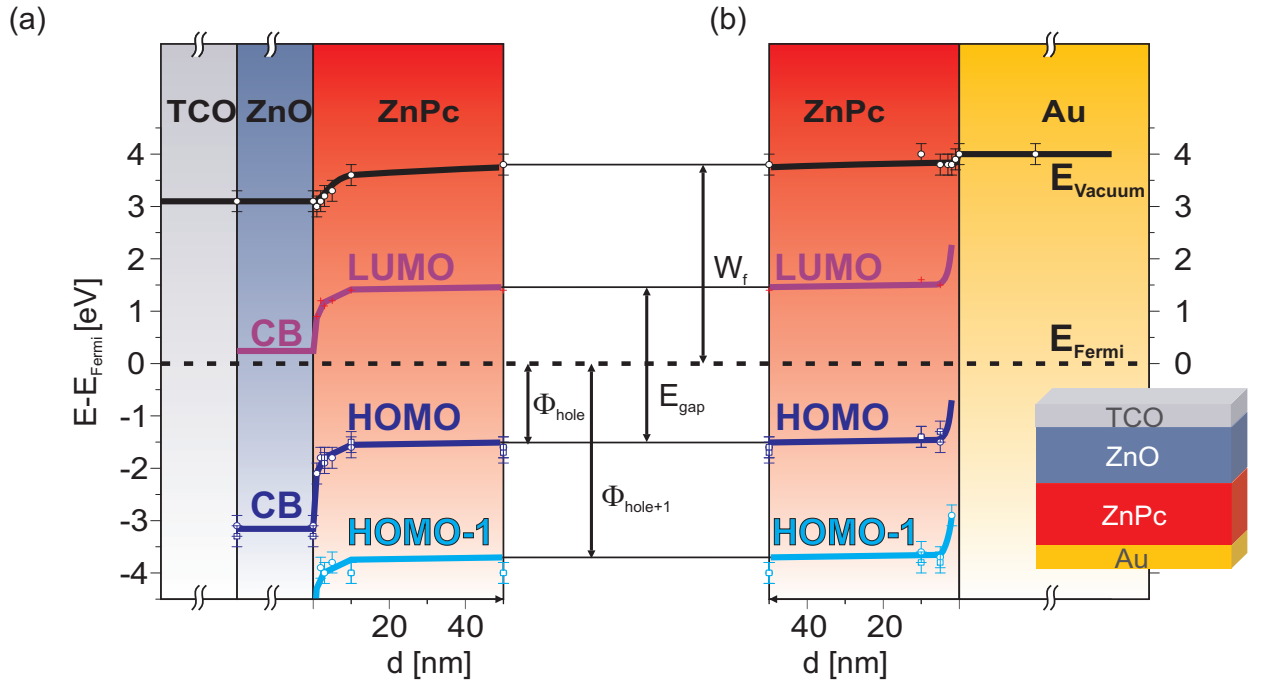
Fig. 6.4: *The band structure of the device derived by UPS. Fermi level alignment is assumed and the vacuum level is derived from the work function. The VB and HOMO were derived from the hole injection barrier while the LUMO and CB are shifted by the band gap value which were taken from UV-Vis spectra and literature data [115] for ZnO and ZnPc, respectively. A continuous increase from left to the right can be seen.*

100 nm, and 200 nm) were prepared and no difference can be observed (not shown here). The sharper LKEC, compared to ITO, suggests a smoother surface. The energetic position stays almost constant, in other words the band structure is rather constant. This leads to the desired ohmic behavior. In the valence region the $O2p$-peak at around 5 eV can be seen with a drop down at around 3.2 eV. No higher features can be observed because of the band gap of the semiconductor. Considering a typical band gap of 3.4 eV for ZnO this confirms a strong n-type behavior. The next feature ($Zn3d$-peak) appears at around 11 eV kinetic energy (not shown here). Because of the broad bands of inorganic semiconductors,

no sharp peaks are observed. Evaporating ZnPc leads to a peak within the previous gap region. It is the HOMO of ZnPc which is located at $1.8\,\text{eV}$ in thin layers and shifts to the bulk value of $1.6\,\text{eV}$. The shift takes place in the first few nanometers which correspond to a sharp p-n-junction. This short ranged cleft leads to exciton dissociation. Apparently, no dipole is developed at the interface. Fig. 6.4 shows the electronic band structure derived by UPS. The work function decreases through the device from the Au cathode towards the TCO anode. This leads to a desired potential drop forcing electrons to the anode and holes to the cathode thus increasing the drift current (see 2.2-vii). Abrupt jumps of the work function which are explained by static dipoles could not be observed. The HOMO of ZnPc bends towards the valence band of ZnO and towards the Fermi energy of Au at the interface, respectively. This bending should also improve the performance and increase the diffusion current (see 2.2-vi).

6.2 Theory of Open Circuit Voltage

At the open circuit voltage V_{oc} all currents are neglected. In other words, the external electric field counteracts the diffusion of charge carriers, caused by concentration imbalance. Under illumination in classical inorganic devices the charge density (n, p) is changed by photogenerated charge carriers.

$$\delta n = \delta p = \tau \cdot \frac{\alpha I}{h\nu} \tag{6.2-i}$$

With a typical intensity of I, absorption α and lifetime τ, this leads to a drastic change
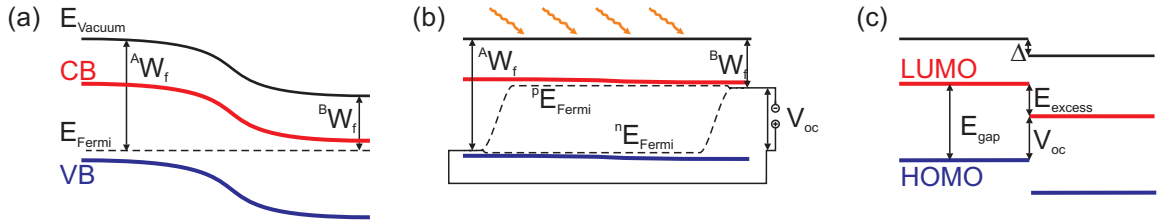
Fig. 6.5: *Sketch of an inorganic p-n-junction (p-type material A with workfunction $^{A}W_f$ on the left and n-type material B with workfunction $^{B}W_f$ on the right) under (a) steady state condition and under (b) illumination with applied V_{oc}. The photogenerated charge carriers lead to splitting of the Fermi energy. The quasi Fermi energy of the minority in the p-type becomes the majority in the n-type ($^{n}E_{Fermi}$) and vice versa ($^{p}E_{Fermi}$). (c) In organic solar cells the energy of the gap E_{gap} of the absorber material is split into the potential of the open circuit voltage V_{oc} and the excess energy E_{excess} (see 6.3). In contrast to inorganic interfaces, dipoles Δ play a crucial role.*

for the minority charge carriers (n in p-type, p in n-type) and only slight change of the majorities. Hence the Fermi energy can be assumed as split into the energy of majorities, which almost stays at the former position and the energy of the minorities, which moves to the other band edge in the band gap. In order to align the energies of the respective charge carriers through the interface, an electric field $\vec{E}$ has to be applied. For the homojunction of p-n-silicon this leads to an alignment of the vacuum energy and the open circuit voltage can be derived from the built-in potential V_{bi}. This can be determined by the difference of

the workfunctions W_f.

$$W_f := \Phi = \int \vec{E}\ d\vec{x} = \int\int \rho\ d^2\vec{x} \tag{6.2-ii}$$

$$^{A}W_f - {}^{B}W_f = eV_{bi} \approx eV_{oc} \tag{6.2-iii}$$

In organic models the workfunction at the interface refers to the charge neutrality level (CNL) instead of the Fermi energy, including dipoles (Δ) as introduced in 2.1-ix [22].

$$^{A-B}\Delta = (1-S)\cdot({}^{A}W_f - {}^{B}W_f) - S\cdot(\Delta_{pillow} + \Delta_{mol}) \tag{6.2-iv}$$

The screening factor S is correlated to Fermi level pinning. The built-in potential disappears completely, if screening $S = 1$. As this is the case in many organic solar cells [24], another source of the open circuit voltage has to be found.

Newer models assume that the open circuit voltage is linked to the energy difference of the LUMO of the acceptor and the HOMO of the donor in undoped organic solar cells.

$$V_{oc} = LUMO_{acceptor} + HOMO_{donor} - \sigma_{energy}$$
$$\approx CB_n + HOMO_p - \sigma_{energy} \tag{6.2-v}$$

The offset depends on the energetic disorder σ_{energy} and on the energetic width of the molecular orbitals [117] amongst other things. As the interface is abrupt and organic molecules are used as absorber material, this theory will be also applied here. Depending on the offset a maximum open circuit voltage close to the hole injection barrier of ZnPc is possible, because the position of CB of ZnO close to the Fermi energy:

$$eV_{oc} \approx CB_{ZnO} + HOMO_{ZnPc}$$
$$\approx \left(E_{gap,ZnO}^{transport} - \Phi_{hole,ZnO}\right) + \Phi_{hole,ZnPc}$$
$$\approx (3.4\,\text{eV} - 3.2\,\text{eV}) + 1.4\,\text{eV} = 1.6\,\text{eV} \tag{6.2-vi}$$

In I-V-characteristic this value will not be reached, because broadening of the molecular orbital and a non zero offset have to be taken into account along with other losses.

6.3 Tuning Excess Energy by Doping

Exciton dissociation is caused by an electric field. This is realized at the interface, where the energetic positions of the electronic states change. The energy difference is the so-called excess energy E_{excess}. The excess energy is in good approximation the difference of the energy gap of the light absorbing material and the open circuit voltage, as defined in the previous section (see Fig. 6.5) [118]. In other words, the excess energy is used to overcome
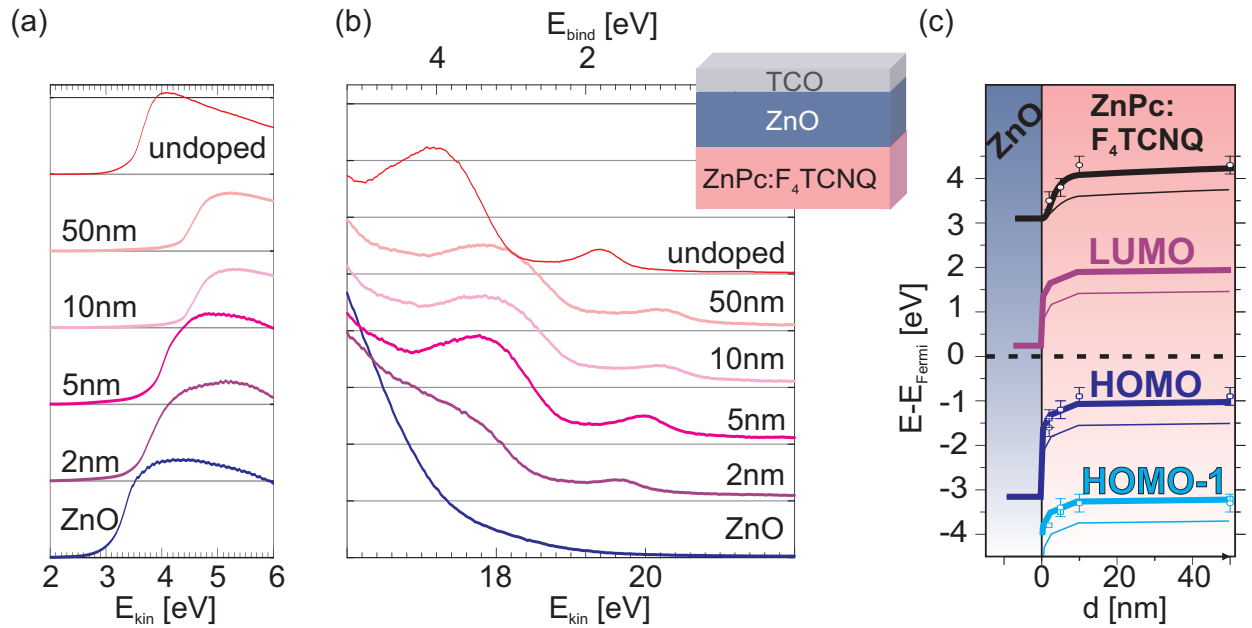
Fig. 6.6: *UPS measurements of ZnPc strongly doped by F_4TCNQ with different thicknesses on ZnO substrates. The spectrum of the substrate (ZnO) and the spectrum of 50 nm pure ZnPc (undoped) are also plotted for comparison. (a) In the low kinetic energy region a continuous shift towards higher energy can be observed with increasing ZnPc thickness, which leads to an increase of the work function. (b) In the HeI region the HOMO of ZnPc can be observed at a binding energy of 1.6 eV and shifts to a value of 1.0 eV which differs by 0.6 eV from pure bulk ZnPc. (c) The electronic structure from the doped setup (thick lines) is plotted together with the band structure of the undoped device (thin lines).*

the exciton binding energy. The remaining energy of the exciton contributes to the voltage of the device. Although the dissociation process is not yet understood and a topic of recent research [119–125], it is assumed that a high excess energy is needed for exciton dissociation. This will decrease the open circuit voltage. On the other hand, if the excess energy is too low, the excitons will not dissociate into free charge carriers and no short circuit current
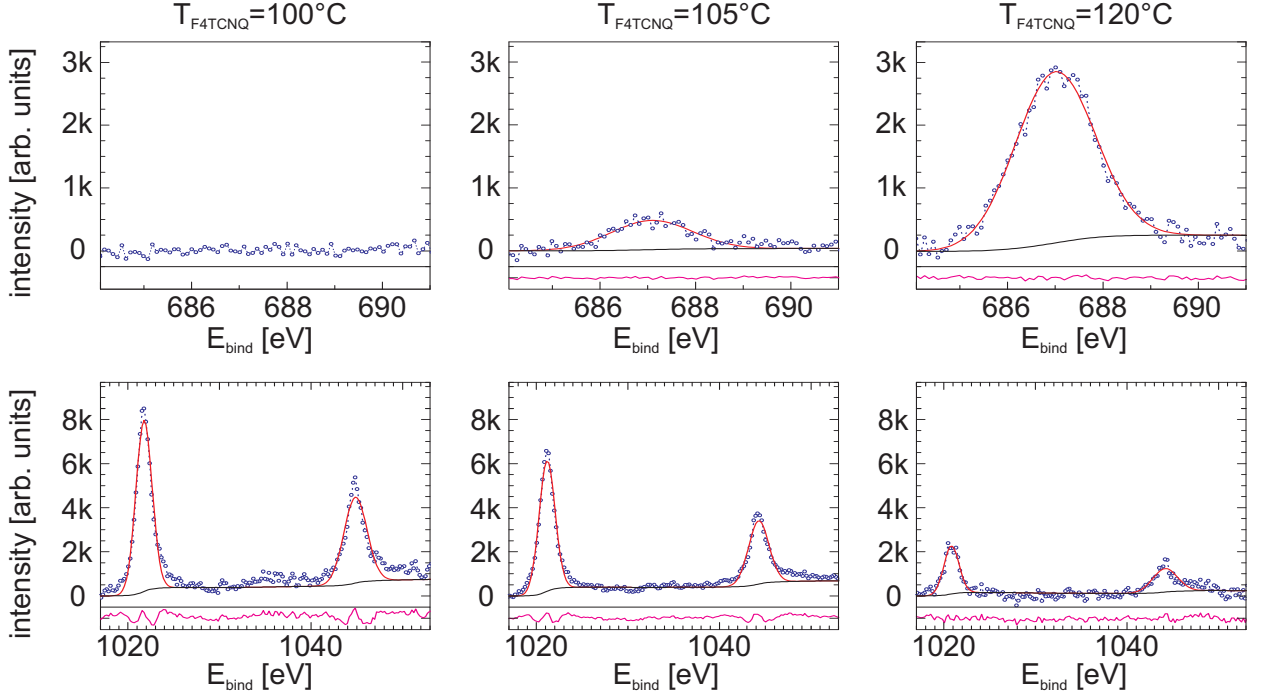
Fig. 6.7: *XPS signal of the F1s (top) and Zn2p (bottom) peaks of F_4TCNQ doped ZnPc samples prepared by different sublimation temperatures of the dopant (indicated above). The two spectra of each column belong to the same sample. The F1s increases in intensity while the Zn2p decreases. This illustrates an increase of the F_4TCNQ content. All graphs are fitted by Gaussian peaks with additional Shirley background. The residuals (magenta) are plotted in a range of 0 ± 1000 counts (box height) below each graph. The minimum value of the background is subtracted for better comparison.*

in terms of photocurrent is produced, which again leads to a low open circuit voltage. This hypothesis can be proven by tuning the excess energy. As the open circuit voltage is the difference between the CB of the n-type semiconductor and the HOMO of the p-type semiconductor, the excess energy can be derived as difference of the CB of the n-type and the LUMO of the p-type material.

$$E_{excess} = E_{gap}^{transport} - V_{oc} = \left(E_{gap}^{optical} + E_{bind}^{exciton} \right) - V_{oc}$$
$$= (LUMO_p + HOMO_p) - (CB_n + HOMO_p)$$
$$= LUMO_p - CB_n \tag{6.3-i}$$

Therefore, the only way to increase the excess energy is to raise the LUMO of ZnPc, as the CB of ZnO is already close to the Fermi energy (E_{gap}=3.4 eV, Φ_{hole}=3.2 eV) and can not be driven lower without charging. The shift of molecular orbitals can be done by dop-

ing. The desired p-doping of ZnPc is already known and can be done by co-evaporation of F_4TCNQ [126, 127]. This is also applied here, and the effect is investigated by UPS (see Fig. 6.6). Compared to the spectra of undoped layers all features are shifted upwards by 0.6 eV. This confirms a successful doping. Also I-V measurements were performed to investigate the conductivity by the increased amount of charge carriers due to doping by an acceptor molecule. For this purpose samples with different F_4TCNQ content were prepared. The sublimation temperature was determined by UV-Vis spectra of F_4TCNQ on pure quartz and no features were observed up to $100\,°C$. Different doping ratios were achieved by a constant ZnPc source temperature and various source temperatures of F_4TCNQ. The evaporation rate was almost constant at around $0.1\,nm/s$ which was mainly caused by the constant ZnPc rate. In other words, the rate of F_4TCNQ is much weaker and could not be monitored by the oscillating quartz. Samples prepared at $120\,°C$ source temperature show nearly ohmic behavior with no photocurrent while samples with temperatures between 100-$110\,°C$ show no significant change with respect to undoped devices (see section 7.3). UV-Vis spectra of the doped layers could neither be described by α-ZnPc nor by β-ZnPc. This is already known for high doping ratios [126]. XPS measurements were performed to check the doping ratio (see Fig. 6.7). The $F1s$ and $Zn2p$ XPS peaks are used as they just appear in F_4TCNQ and ZnPc, respectively. $F1s$ corresponding to dopant increases with temperature

Tab. 6.1: *Summary of the main information of Fig. 6.7. The area A of the F1s and Zn2p XPS peaks are calculated by a fitted Gaussian peak after subtracting the Shirley background [128]. The four samples prepared under identical conditions except for the increasing F_4TCNQ sublimation temperature (T) show an increasing dopant content.*

T [°C]	100	105	110	120
A(F1s)	0	992	2847	5701
A(Zn2p$_{3/2}$)	17226	12969	6004	4525
F_4TCNQ-content	0 %	9 %	38 %	62 %

while $Zn2p$ corresponding to ZnPc decreases. As assumed the doping ratio changes with sublimation temperature but absolute values can not be used to compare peaks from different samples because different measurements could also have different conditions. Therefor the Zn signal was compared to the F signal of the same sample. After subtracting the Shirley

background [128] the peak area (A) was fitted (see Tab. 6.1). Including the weighting factor (S_x) the doping ratio c can be calculated [129]:

$$c(F1s) = \frac{A(F1s)/S_x(F1s)}{A(Zn2p)/S_x(Zn2p) + A(F1s)/S_x(F1s)} \qquad \text{(6.3-ii)}$$

To account for the respective stoichiometry, a factor of $^1/_4$ has to be included for F. The results show a quite high doping (9 %) already at a sublimation temperature of 105 °C. The doping ratio can be decreased using higher ZnPc sublimation temperatures. This was not performed because no stable evaporation rate was reached. Hence F_4TCNQ sublimation temperatures of around 102 °C were adjusted.

CHARGE TRANSPORT

In this chapter the collection of charge carriers at the electrodes is elaborated. For this reason the conductivity of the single layers is discussed. Also the I-V-performance of the device is analyzed and the influence of nanostructures investigated.

7.1 Conductivity

In this work borosilicate glass was used as substrate because it is transparent. The insulating material can not be used to collect charge carriers. For this reason a transparent conducting oxide (TCO), like ITO or AZO is used. To find a proper transparent substrate with electrode material, several current-voltage measurements were performed, using different glass-TCO
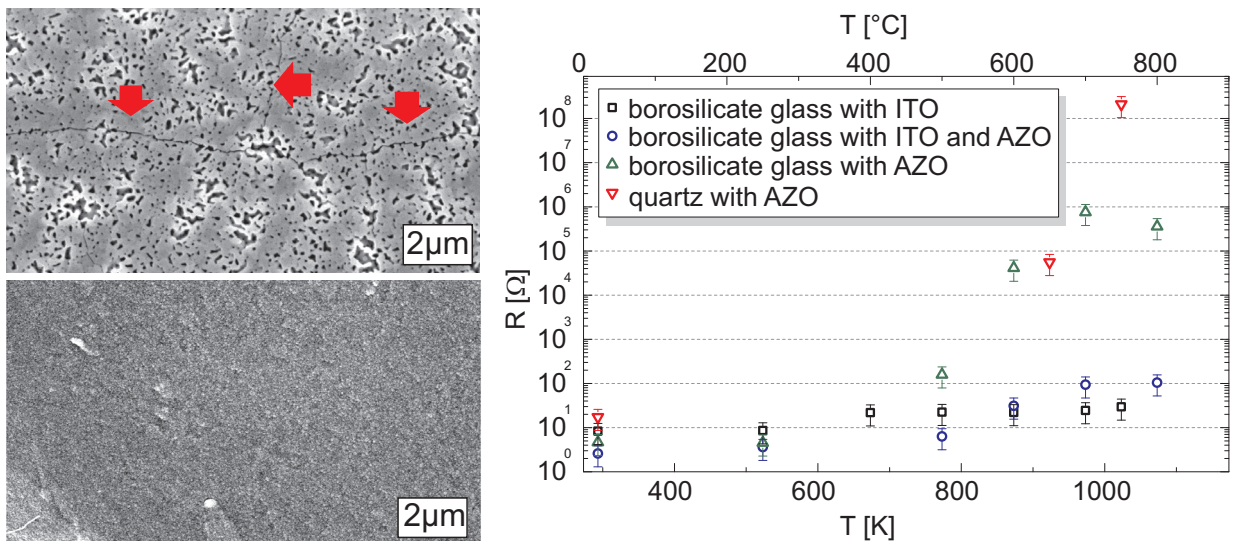
Fig. 7.1: *SEM images of AZO on quartz (top left) and ITO on borosilicate glass (bottom left). The red arrows mark cracks which lead to lower conductivity. This can also be seen in the graph to the right, where AZO on quartz glass has the highest resistance at higher annealing temperatures compared to the other materials. This effect is due to different thermal expansion coefficients which lead to cracks in the layer.*

combinations. Low resistivity will lead to high charge carrier collection. The resistivity ρ of these and other layers were extracted from the slope of ohmic I-V-characteristics with given thickness and area.

The electrode material shows a high conductivity as desired. Au, which was used as cathode material, is known to have a quite low resistivity. A few hundreds of $m\Omega\frac{mm^2}{m}$ could be measured. All TCOs used on glass substrates show a resistivity of a few $\Omega\frac{mm^2}{m}$. Coating the TCO layer with the less conductive ZnO semiconductor material leads to an increase of the value. Samples with $50\,\mathrm{nm}$ to $200\,\mathrm{nm}$ ZnO show a resistivity of some $G\Omega\frac{mm^2}{m}$. Thus, the measured resistances are comparable to reference data [130, 131].

The TCO was also heated while synthesizing nanowires. Hence the development of the resistance by thermal treatment was investigated (see Fig. 7.1). Borosilicate glasses with as-delivered ITO show just a slight increase in resistance. AZO layers, especially on quartz glass, lead to a significant increase of the resistance. By investigating the samples using SEM cracks can be found in the AZO layer on quartz, which will prevent high conductivity, while the ITO layer stays closed. One reason can be found in the thermal expansion coefficient. ITO ($3.5\mathrm{x}10^{-6}\ ^1\!/_\mathrm{K}$) is quite close to the value of the glass substrate ($3.3\mathrm{x}10^{-6}\ ^1\!/_\mathrm{K}$), but quartz glass ($5.4\mathrm{x}10^{-6}\ ^1\!/_\mathrm{K}$) differs from AZO ($6.5\mathrm{x}10^{-6}\ ^1\!/_\mathrm{K}$).

7.2   Simulation of Characteristics

The I-V-characteristic depends on many parameters as introduced in section 2.2. Consequently a quite complicated model is needed to describe the characteristics. Including only diodes (with ideality factor n), parallel resistances ($R_{parallel}$), series resistances (R_{series}), and a photodriven current source (I_{photo}) leads already to an implicit function (see 2.2-xviii). The parallel resistances represents shunts, while series resistances stem from wires and bad contacts. Extracting these parameters assists in understanding the influence of each one on the performance of the device. The equation was implemented in mathematica and sim-
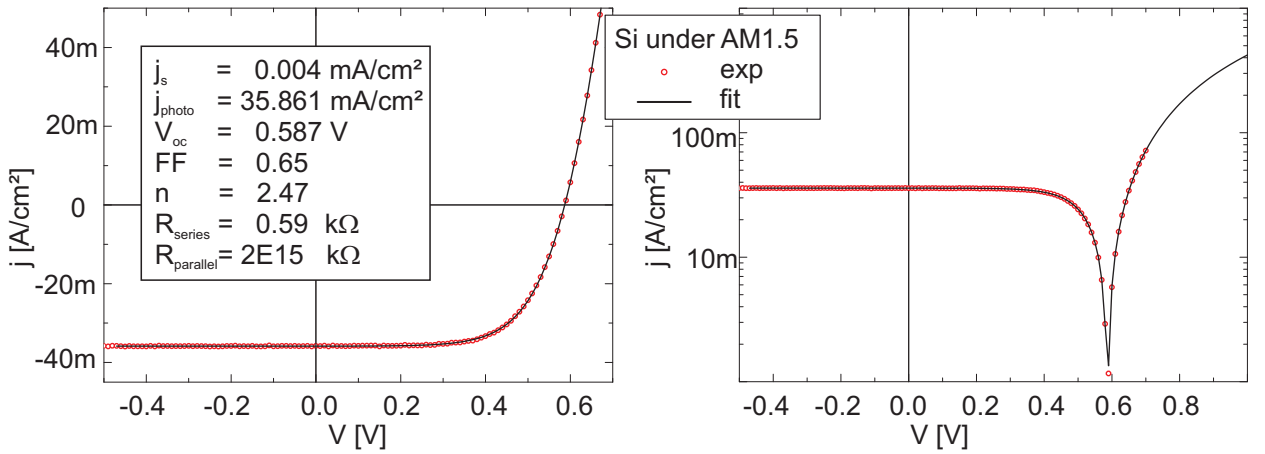
Fig. 7.2: *Measured (red dots) and fitted (black solid line) j-V-curve of a silicon solar cell. The fitted parameters are shown in the legend. The plot on a linear scale (left) shows the ohmic contribution much better, while the semilogarithmic plot (right) is better suited to compare V_{oc} and j_{photo}.*

plified. Using the Lambert W function mathematica forms an explicit equation to fit the current-volatage characteristic.

$$
I = \frac{n \cdot kT(R_{parallel} + R_{series})}{e \cdot R_{series} \cdot (R_{parallel} + R_{series})} \cdot W + \frac{e \cdot R_{series} \cdot (V - I_{photo}R_{parallel})}{e \cdot R_{series} \cdot (R_{parallel} + R_{series})} \tag{7.2-i}
$$

$$
W = W\left(e \cdot I_{sc} \cdot R_{parallel} \cdot R_{series} \cdot exp\left\{ \frac{e \cdot I_{photo} \cdot R_{parallel} \cdot R_{series} + e \cdot R_{parallel} \cdot V}{R_{parallel} \cdot n \cdot kT + R_{series} \cdot n \cdot kT} \right\} \right.
$$
$$
\left. \cdot \frac{1}{(R_{parallel} + R_{series}) \cdot n \cdot kT} \right)
$$

The equation was used to get further information on the hybrid solar cells built in this thesis. Nevertheless, the fit and the experimental data have to be compared, since the explicit form is not bijective.

As a proof of concept the fit function was first tested using the I-V-curve of a silicon solar cell (see Fig. 7.2). Proper parameters like V_{oc}, j_{photo}, FF, and R_{series} could be extracted. Especially, $R_{parallel}$ seems quite high because of the almost straight horizontal line in the negative bias region. This is not expected for thin hybrid solar cells, as shunts are more likely compared to thick silicon cells. So equation 7.2-i is applied in the following sections.

7.3   Performance of the Devices

The first hybrid solar cells were built by using ITO, ZnO, ZnPc and Au on glass only. Thin ZnPc layers (i.e., below 70 nm) show an ohmic behavior, which can be seen in terms of a constant slope in the linear I-V-plot (see Fig. 7.3). This effect can be explained by shunts, caused by penetration of the cathode material through the organic semiconductor while coating, which is already known. To overcome this effect, thicker layers or a PEDOT EBL were used. Both results in Schottky like curves. The series resistances of all devices are
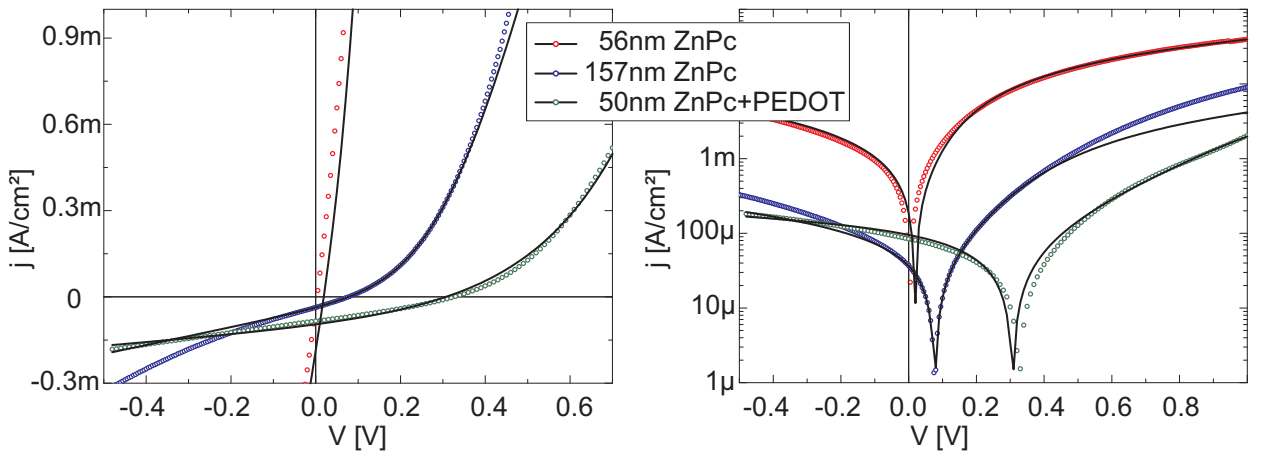
Fig. 7.3: *Current density-voltage-characteristic of selected ZnO-ZnPc-stacked hybrid solar cells under AM1.5 illumination with an area of $0.25\,cm^2$. The trend of the red dots, representing a thin ZnPc layer, show nearly ohmic behavior with a quite low resistance. The other devices show Schottky-like behavior whereby the thinner device containing PEDOT (P) gives a better performance. The black solid line corresponds to the fitted curves.*

in the order of that of the ZnO layer. Shunts in the ZnPc layer may be a possible reason. The parallel resistance increases by one order of magnitude for the device with thicker ZnPc layer as well as for the device containing PEDOT.

In general, the solar performance ($\eta < 0.1\%$) is weak compared to silicon or other solar cells. The sample with PEDOT shows an appropriate open circuit voltage ($V_{oc} \approx 0.3\,V$) for first experiments, but this is still a low value. The extremely low photocurrent ($j_{sc} < 1\,\frac{mA}{cm^2}$) is a more serious problem. This also influences the low V_{oc} as the kink in the curve takes place at bias larger than the V_{oc}. As mentioned in the previous chapter, the exciton dissociation, which is correlated to the photocurrent, may be related to the excess energy. For this reason
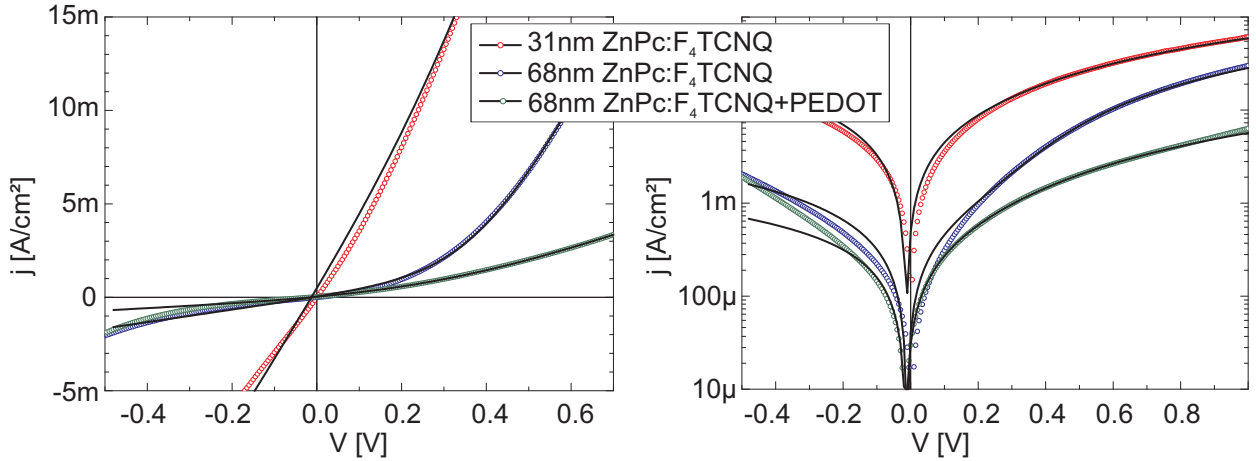
Fig. 7.4: *Current density-voltage-characteristic of selected hybrid solar cells consisting of F_4TCNQ doped ZnPc and ZnO layers under AM1.5 illumination with an area of $0.2\,cm^2$. The device with a thin organic layer (red) shows nearly ohmic behavior which becomes Schottky-like with increasing layer thickness (blue), but adding PEDOT (green) leads again to an ohmic behavior with higher resistance. The current density is larger than for the undoped devices, which is caused by the increase of charge carrier concentration. Nevertheless, no photogenerated carriers could be detected. The black solid line corresponds to the fitted curves.*

hybrid solar cells with stronger p-doped ZnPc layers were prepared. In section 6.3 the doping of ZnPc by F_4TCNQ was already introduced, and the best parameters were obtained for a sublimation temperature of $102\,°C$, as it was done in all devices presented in the following part. Compared to the undoped samples, all solar cells with F_4TCNQ showed slightly higher current density as can be seen in Fig. 7.4 compared to Fig. 7.3. The reason for the high current is the increased number of charge carriers by doping which leads to a proportional increase of the conductivity. Again, an ohmic behavior could be observed for thin layers, which may also correlate to penetration effects, while thicker layers tend to a Schottky-like shape. Also PEDOT was used as additional layer. In the present case the resistance of PEDOT seemed to be larger than that of the doped ZnPc layer, as the curve converted again back to an ohmic behavior but this time with a higher resistance. The photocurrent was not even detectable although an increased value had been predicted. This also led to a negligible open circuit voltage. Hence the doping, even if it led to higher conductivity, could not simply be used to increase the photocurrent by enlarging the excess energy. A possible reason could still be linked to the electronic structure. It was possible to investigate the bending in the organic semiconductor. Due to penetration effects, the development of the

Tab. 7.1: *The main solar cell parameters are determined from an I-V measurement under AM 1.5 condition. The integrated photocurrents from EQE spectra are added for comparison.*

thickness [nm]	V_{oc} [V]	j_{sc}	j_{EQE} $[\frac{mA}{cm^2}]$	$R_{parallel}$	R_{series} $[\Omega \cdot cm^2]$	η [%]
ZnO as inorganic component						
56	—	—	0.10	100		< 0.01
65	0.01	0.04	0.10	95	60	< 0.01
157	0.08	0.03	0.12	2500	161	< 0.01
50+P	0.33	0.11		2333	385	0.01
ZnO-NW as inorganic component						
(300+P)	0.10	0.23		1700	100	0.01
150 nm CdS as inorganic component						
54	0.49	1.22	1.13	1500	80	0.15
71	0.80	1.40	2.15	1400	300	0.30
142	0.76	1.90	3.26	2000	2000	0.76
Si reference solar cell						
no ZnPc	0.59	35.21	22.68	2×10^{18}	590	12

interface in the inorganic component was not possible to investigate. As higher doping of the organic material can lead to an extended bending width in the inorganic semiconductor (see 2.1-viii), the abrupt interface might be smoothed.

7.4   Nano Structure

Another way of increasing the photocurrent density is the introduction of nanostructures. Besides to bulk heterojunctions and introducing nanoclusters into solar cells, nanowires are very promising. After synthesis they are still in contact to the electrode material, and as they can be grown straight, the pathway of charge carriers in the collection process is quite short. Orientation, composition, and size can also be tuned. In this section single crystalline ZnO nanowires (ZnO-NW) for hybrid solar cells are investigated. The first experiments show the
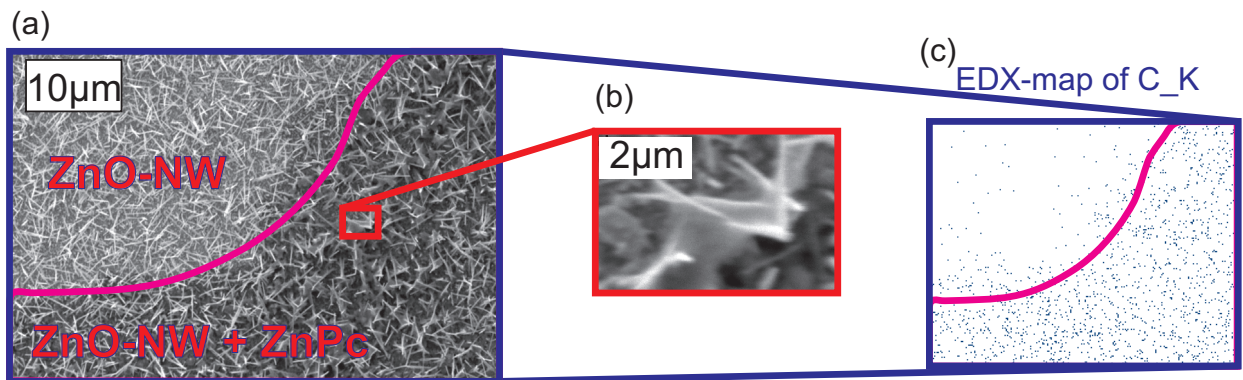
Fig. 7.5: *(a) The SEM image of ZnO-NW grown on Si coated with one droplet of ZnPc dissolved in DMF shows bright and dark regions which are caused by high and low conductivity, respectively. (b) Zoom in on the dark region, wetting of the ZnO-NW can be observed. (c) The distribution of carbon, taken by EDX of the carbon K-line, represents the organic molecules. A correlation of the dark region and ZnPc can be seen.*

contact and distribution of ZnPc on ZnO-NWs. Therefore a sample with randomly oriented ZnO-NW was coated with a droplet of ZnPc dissolved in DMF and analyzed by SEM and EDX (see Fig. 7.5). The SEM images show bright and darker regions which can be linked to the lower conductivity of ZnO-NW when covered with ZnPc. This could be confirmed by the distribution of carbon which corresponds to ZnPc, via an EDX mapping of the C-K_α-line. In the magnified image it can be seen that ZnPc cling to the NWs. The next step was to build a hybrid solar cell consisting of ITO, ZnO-NW, ZnPc, PEDOT, and Au (see Fig. 7.6). As the contact area is increased by the nanostructures, a larger amount of the organic material ZnPc is needed to cover the ZnO, compared to the layered device. Using the same amount ($\approx 50\,\text{nm}$), only small clusters at the NWs can be observed. A sufficient coverage of the
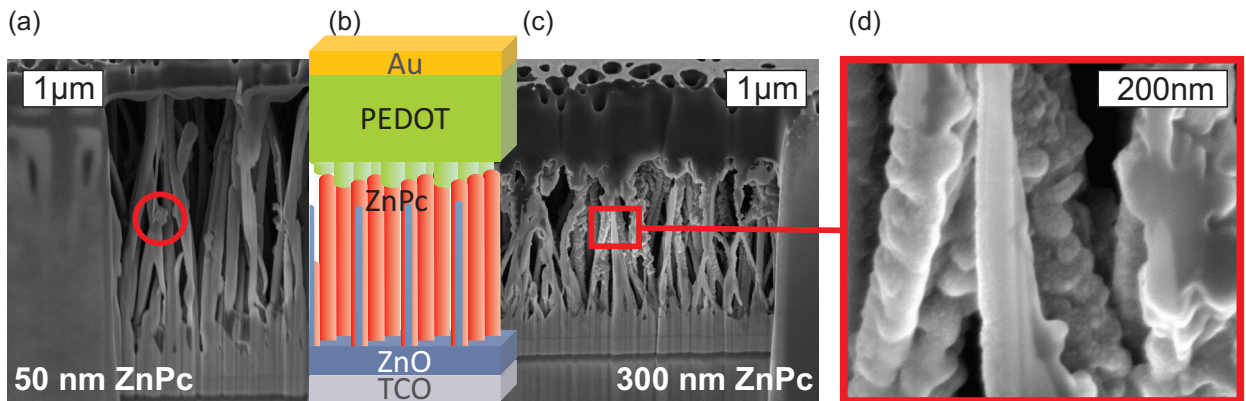
Fig. 7.6: *The SEM images of the cross section of a nanostructured hybrid solar cell device with (a) low and (b) high amount of evaporated ZnPc show that thick layers are needed to cover the nanowires (inset, d). Otherwise just small clusters are formed (circle in a). (b) The scheme serves as illustration of the device setup.*
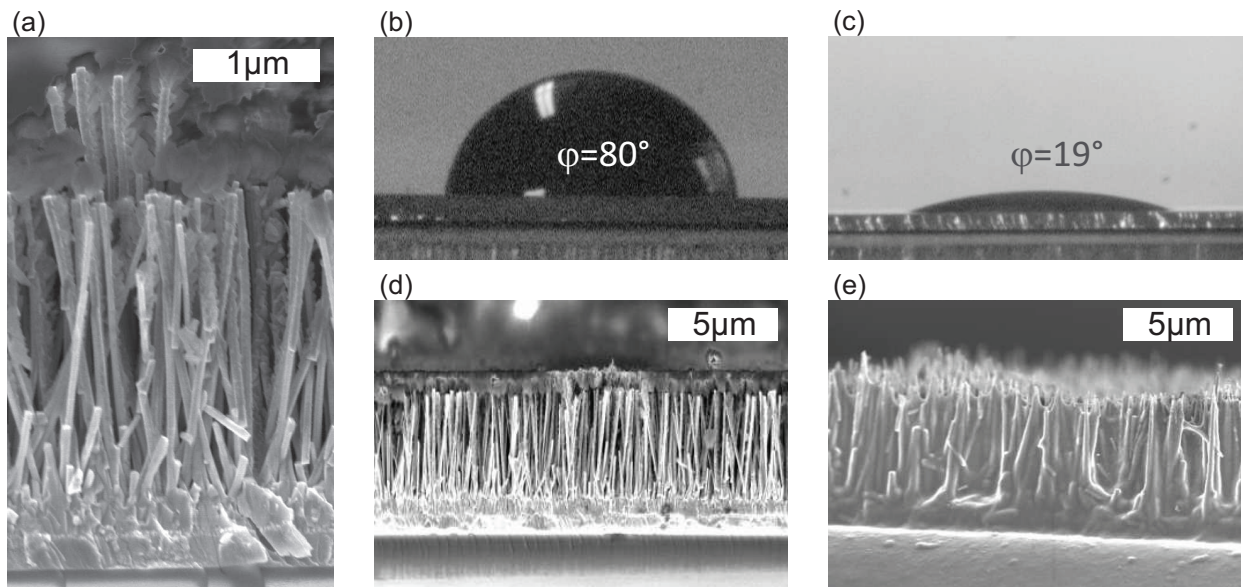
Fig. 7.7: *These images show certain problems of nanostructured devices. Different nanowire length can lead to short circuit, due to breakthrough of the cover layer (a). Bad wetting of the PEDOT, represented by a large contact angle (b), leads to an overlayer, which only contacts the nanowire tips (d). This problem can be overcome by the usage of a surfactant, which decreases the contact angle (c), and leads to infiltration (e).*

NWs can be achieved using six times the amount (i.e., 300 nm of ZnPc). Despite of the formation of small clusters, the ZnPc covers the ZnO-NWs nicely (see Fig. 7.6 d). Adding the PEDOT leads to voids in the device. The polymer forms a closed layer on top of the nanostructures and does no infiltrate the space in between the wires. For this reason the contact angle of PEDOT on ZnPc was investigated (see Fig. 7.7). The pure PEDOT as delivered showed a large contact angle ($\varphi \approx 80\,°$). In other words, the attraction between ZnPc and PEDOT is quite weak. The PEDOT was dissolved in water. Since the solvent is volatile and vaporizes, the contact angle decreases by time. The influence of the decreasing water-PEDOT ratio was minimized by time-dependent contact angle measurements (not shown here). The data $\varphi(t)$ were extrapolated to the initial contact angle $\varphi(0)$. The weak attraction can be linked to the solvent. ZnPc shows also bad solubility in water (see section 4.1). Using other solvents (e.g., acetone) can lead to polymerization of PEDOT, which is not desired. For this reason a surfactant was added. A drastic decrease of the contact angle ($\varphi \approx 19\,°$) could be achieved. This slightly changed PEDOT mix was used in all measurements presented. Also a better infiltration into the NW could be observed (see Fig. 7.7 e).

The performance of hybrid solar cells did not show the expected improvement via introducing ZnO-NW (see Fig. 7.8). Contrary to the simple assumption of an increased
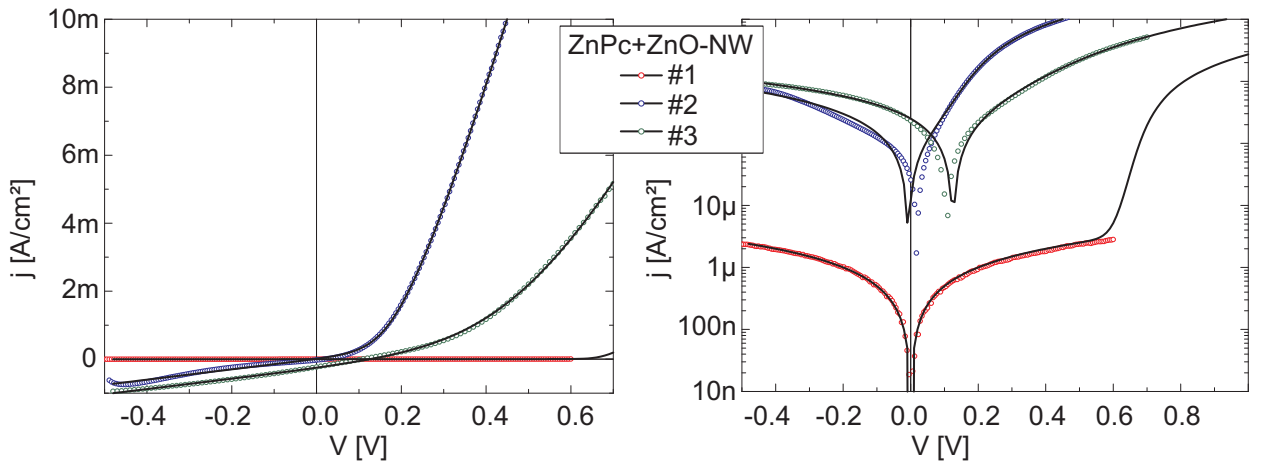
Fig. 7.8: *The graphs show current density-voltage-characteristics of selected hybrid solar cells with ZnO-NWs under AM1.5 illumination with an area of 0.2 cm^2. ZnO-NW (#1) with high NE density lead to scattering but also to a huge resistance and no detectable photocurrent. The black solid line corresponds to the fitted curves.*

photocurrent through the huge active area of high dense nanowires almost no current could be detected. The devices with dense nanostructures show only high resistance. A certain nanowire separation is needed for photovoltaics to make use of the whole nanowire length [132]. Decreasing the distance also correlates with photon absorption only on the top of the wires. Lower packed samples show at least a Schottky-like characteristic which in a few cases also generates a photocurrent ($^{NW}j_{photo} \approx 300 \, \frac{\mu A}{cm^2}$), which is larger compared to the layered device ($^{layer}j_{photo} \leq 110 \, \frac{\mu A}{cm^2}$). The series as well as the parallel resistances are slightly lower, but in the same order of magnitude compared to the layered device. Low parallel resistance which corresponds to undesired shunts can be linked to a incomplete coverage of the nanowires. On the other hand, a low series resistance is caused by good connection to the electrodes and correspond to good charge carrier extraction.

Chapter 8

SUMMARY AND OUTLOOK

In this thesis the concept of hybrid solar cells is explored. A promising material combination of a II-VI semiconductor and zinc(II)-phthalocyanine is introduced and motivated. Especially the organic component ZnPc was characterized. The whole device was built, and a photocurrent could be detected. By the investigation of the single solar cell processes, many insights were gained which shall be summarized here in brief:

Inside the absorber the photons create excitons. This process of light absorption is described by Fresnel equations for planar structures. The simulated curves are fitted to experimental data. Hence important parameters, i.e., the optical constants, the material thickness and roughness could be extracted. Via fitting five samples simultaneously, non-physical solutions could be safely avoided.

The excitons, generated by photon absorption, were recorded spectral sensitively. This was done by means of external quantum efficiency, which detects the normalized photocurrent with respect to the incident photon energy. Using this data the excitons were analyzed further. The origin of generation was determined to be the organic ZnPc layer, while the dissociation takes place at the ZnPc-ZnO interface. The exciton current drops down to $^1/_e$ at a distance of approx. 16 nm, as it was found to be the exciton diffusion length.

The electronic structure of the dissociation region, i.e., the ZnPc-ZnO interface, was investigated in detail. Valance structure, workfunction, and band bending were derived by UPS measurements. A promising band structure for the whole device could be determined. Furthermore, p-doping of the organic layer was realized with the acceptor molecule F_4TCNQ. By that, an energetic shift of up to 0.6 eV was achieved. Despite of this improvement it was not possible to reach the predicted high open circuit voltage of approx. 1.6 V.

Several current-voltage characteristics were recorded. The solar cell with best ZnPc performance was achieved in a stacked device in combination with ZnO and the electron blocking layer PEDOT. The values achieved ($V_{oc} \approx 330$ mV, $I_{sc} \approx 110 \frac{\mu A}{cm^2}$) could be beaten

by devices containing CdS ($V_{oc} \approx 760\,\mathrm{mV}$, $I_{sc} \approx 2\,\frac{mA}{cm^2}$). However, the charge carriers leading to this improved performance stem from the inorganic layer.

It is obvious that no economical yield could be achieved by the devices fabricated. Despite of numerous insights, gained in this work, further research is still needed to get a complete understanding. Some open problems are: The band structure was derived by UPS of evaporated organic layers on top of the inorganic components. Coating could lead to band bending within the inorganic material which is not detectable with the surface sensitive characterization method used. Excitation of the sample with higher energies (e.g., hard-x-rays) leads to larger penetration depth. For this reason the band structure within the bulk and deeper layers will be accessible. Experiences on this electronic structure may lead to explanations of lower open circuit voltage and charge carrier drift in the respective semiconductor.

Also, the driving force of exciton dissociation remains an open question. Likewise to pure organic solar cells, the roles of excess energy, disorder, hot and cold excitons, are still not completely understood.

Despite of incomplete knowledge, a few improvements are already possible: After preparing a single layer it was necessary to exposure the sample to air, because every layer is deposited in another coating tool. This leads to contamination of the respective surface and finally to adsorbates at the interfaces. Inline processing without breaking vacuum and final encapsulation could reduce undesired particles creating defect states.

Nanostructures were presented to improve the performance. The nanowire samples showed random parameters of density, length, and thickness. A template based synthesis would ensure a defined nanowire separation and density. After realizing this process, it will be possible to find the optimum arrangement and correlate it to theory. The nanowire length and thickness should be controlled via growth time and the size of the catalyst, respectively. Previous experiments could show that even more parameters (e.g., growth pressure, source-sample distance, gas flow) influence the nanowire shape. For this reason the investigation of nanowire growth is needed to optimize the nanostructure for the hybrid solar cell.

So far only semitransparent solar cells have been produced. The improvement of the cell preparation can enhance the efficiency in the visible red region. In combination with other

materials it will be possible to create tandem cells with higher efficiency. Especially green absorber materials will lead to a much larger power output because of the high intensity of the green light in the sun spectrum.

APPENDIX

A.1 Workfunction in Photoelectron Spectra

The determination of the workfunction via photoelectron spectroscopy demands a thorough treatment. At first one has to consider a kinetic energy larger than the detector's workfunction. Otherwise the cut-off observed correlates to the detector. For this reason an additional bias voltage is applied. The position of the workfunction was evaluated by fitting a straight line with the maximum slope of the LKEC. The energy value of the intersection of this line and the background was used as workfunction. If the sample was exposed to air, adsorbates lower the workfunction. This can be observed for UPS (see Fig. A.1). By sputtering a clean surface can be prepared, whose workfunction matches the literature values. Because of the sensitive organic layers no sputtering was used.
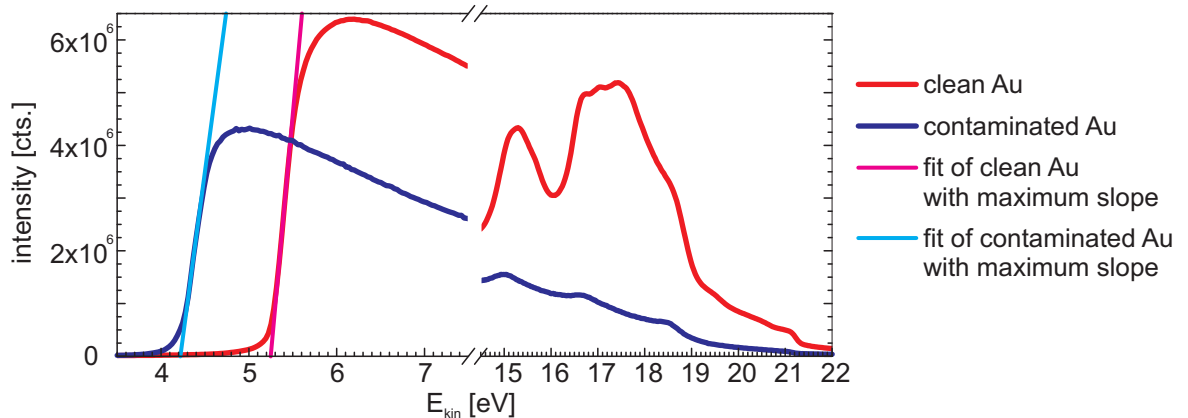
Fig. A.1: *UPS of gold. Contamination occurs via exposure to air. Clean gold was prepared by sputtering and show more pronounced features in the high kinetic energy region. The workfunction was determined by fitting the maximum slope of the LKEC. Adsorbades lead to a decreased workfunction on the contaminated sample.*

A.2 Tunneling Spectroscopy of ZnPc

Scanning tunneling spectroscopy can be used to derive the density of states, which is related to the band structure.

$$\left.\frac{\partial I_{tunnel}}{\partial V}\right|_{V_{tunnel}} \propto \rho_{sample}\left(eV_{tunnel}\right) \tag{A.2.i}$$

A ZnPc coated gold surface was scanned under UHV conditions at room temperature. Only a rough surface could be detected (similar to Fig. 4.2 d). On top of a single cluster STS was performed. Many spectra had to be disregarded because of thermal noise and instabilities. The remaining I-V curves were averaged and smoothed over 200 points (Savitzky-Golay method). The feature at 1.3 V can be linked to the LUMO of ZnPc. In combination with
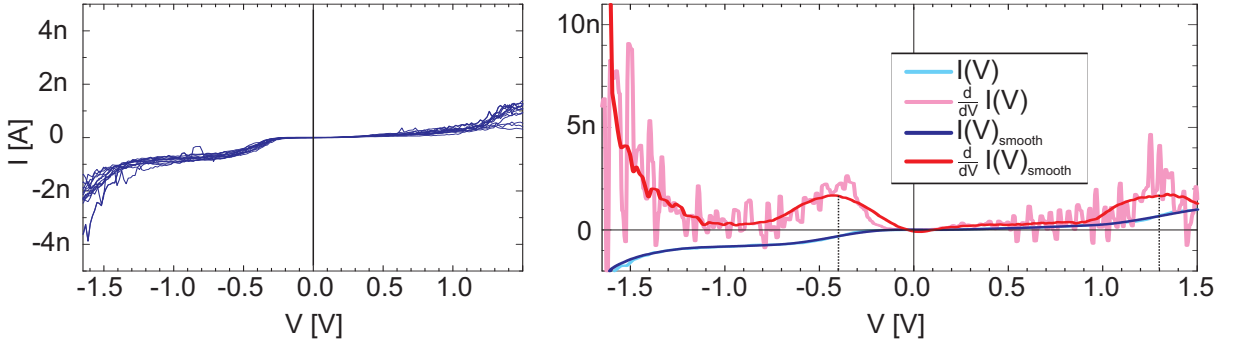
Fig. A.2: *I-V-spectroscopy (blue) and the derivation (red). To get the density of states, 14 spectra (left) were taken for ZnPc on Au at room temperature. To reduce the noise the spectra were averaged (cyan right) and smoothed over 200 points (blue right). The first derivative ${}^{dI}/_{dV}$ can be correlated to the density of states.*

the HOMO of -1.6 eV this gives an transport energy gap of 2.9 eV which is in good agreement with literature data. The HOMO could not be measured explicitly but a slope at -1.6 V is observed. The origin of the feature at -0.4 V is not clear. Possible origins can be the Shockley state, the surface state of gold, which is implausible, because of the rather thick ZnPc layer of a few tens of nanometers. Another reason can be inner gap states of ZnPc caused by defects or also surface states of ZnPc.

A.3 Alternative Thickness Determination

There are many methods to derive film thicknesses. Before using the very accurate optical method (see section 4.3), step profiles and SEM cross sections were analyzed (see Fig. A.3). The profile was detected by a Dektak 3030 scanning an approx. 50 nm thick ZnPc film. The step was generated by covering the sample with a thin wire during the evaporation process. The accuracy is in the same order as the film thickness. Molecules are soft matter compared to the hard quartz glass substrate. This can lead to strains while scanning. Hence, thinner layers are assumed.

Another possibility is cross section SEM prepared with a focused ion beam (FIB). To protect the organic layer from ion bombardment, a platinum coating is used. Platinum (Pt) was used as it is equipped to the FIB tool. The cross section of a approx 100 nm thick ZnPc layer on quartz (Fig. A.3 b) were investigated in detail. The pure organic layer (dark region) is covered with an interlayer (homogeneous grey) before the pure Pt (grey and white clusters) is connected. The interlayer may stem from inclusions of Pt atoms into the organic material. Again no accurate film thickness will be detected.
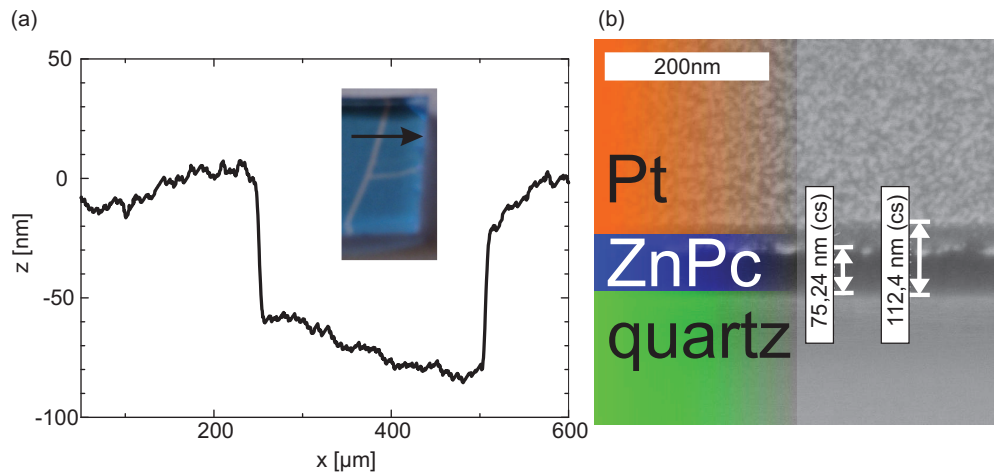
Fig. A.3: *(a) Profile recorded with an profilometer of a 50 nm thick ZnPc layer on quartz which can be seen in the inset. (b) SEM crossection of a 100 nm thick ZnPc layer on quartz glass coated with approx. 1 μm platinum.*

A.4 Nanowire Growth and Quality

ZnO-NW were synthesized by the vapor-liquid-solid (VLS) growth mode [54]. The ZnO source material was mixed with carbon to perform carbon assisted growth [55] which reduces the required growth temperature. Hence, substrates with lower melting temperature, such as glasses, can be used. Another advantage is the decrease of defects, which can be observed in cathodoluminescence (CL) spectra (see Fig. A.4 b). The main peak at approx. 3.4 eV corresponds to the bandgap while the broad green band is connected to defects. The
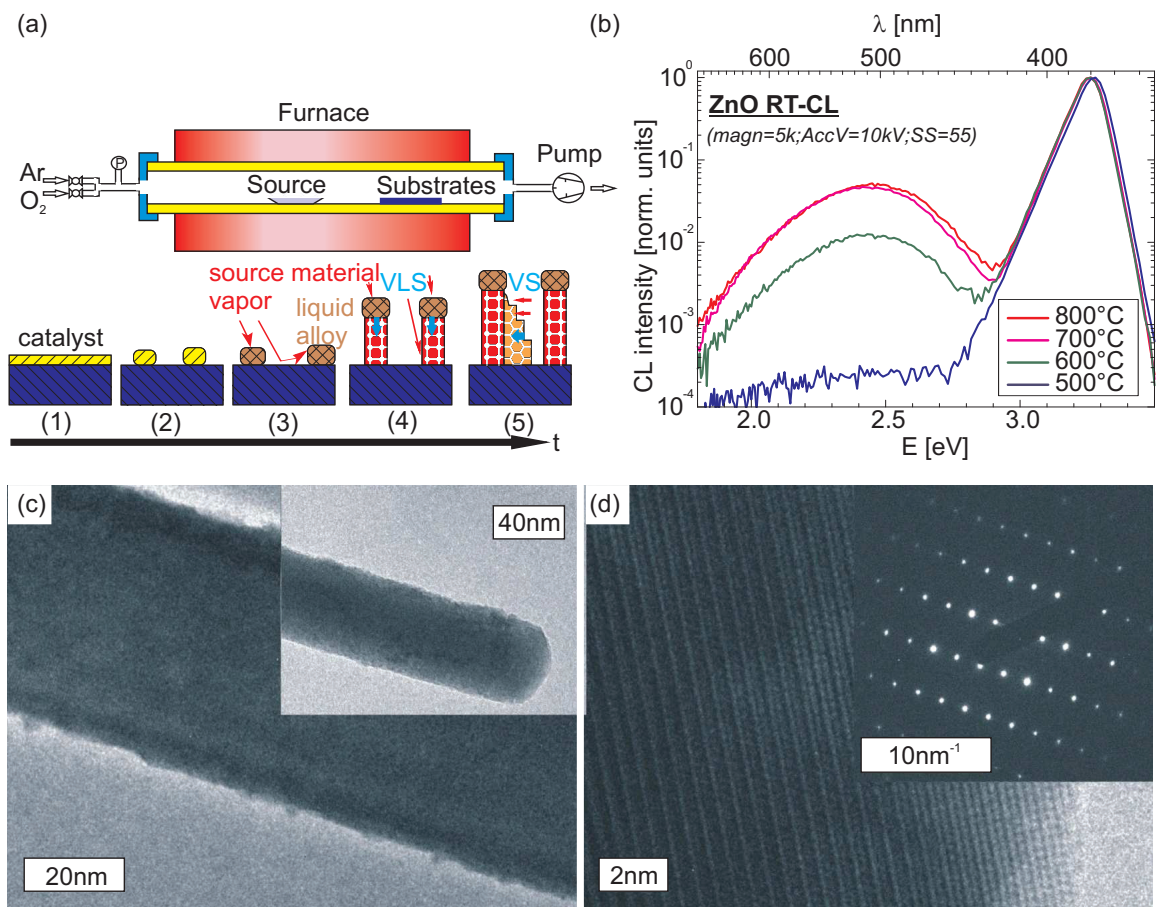
Fig. A.4: *(a) Sketch of the growth reactor and the growth mechanism in principle. (b) Decreasing the growth temperature to synthesize ZnO-NW on glass substrates leads also to decrease of defects, detected as green band in CL. (c, d) High crystalline quality is achieved as can be seen in TEM with the electron diffraction pattern.*

growth mode allows the atoms to self-assemple. For this reason high crystallinity can be achieved (see Fig. A.4 d). Tuning the growth conditions and varying the substrate leads to

different nanowire orientation and density. Aligned nanowires can be synthesized by substrates matching the lattice constant of ZnO (see Fig. A.5 b). Different pressure and gas flow leads to different nanowire densities (see Fig. A.5 c and d).
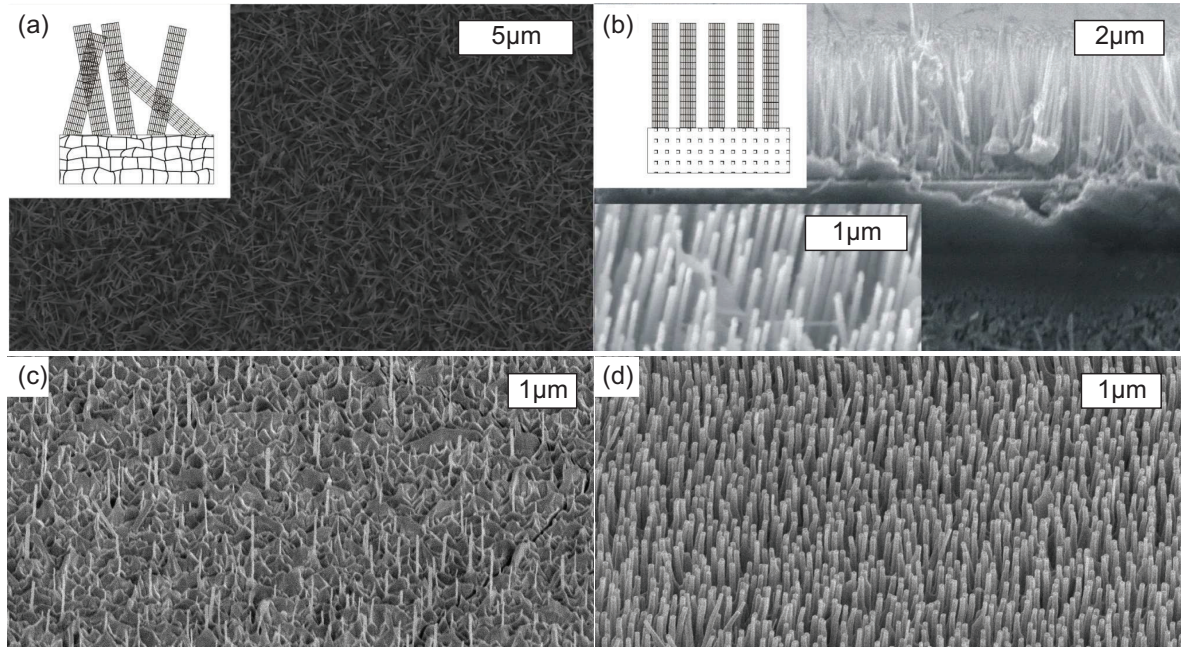
Fig. A.5: *The SEM images of various samples show the dependency on the growth conditions.*

BIBLIOGRAPHY

[1] W. Smith: *Effect of light on selenium during the passage of an electric current.* Nature **7**, 303 (1873).

[2] W. Shockley: *The Theory of p-n Junctions in Semiconductors and p-n Junction Transistors.* Bell Labs Tech. J. **28**, 435–489 (1949).

[3] M. A. Green: *Third Generation Photovoltaics: Advanced Solar Energy Conversion.* Springer-Verlag, Heidelberg (2003).

[4] W. Shockley and H. J. Queisser: *Detailed Balance Limit of Efficiency of p-n Junction Solar Cells.* J. Appl. Phys. **32**, 510–519 (1961).

[5] H. Ishii, K. Sugiyama, E. Ito, and K. Seki: *Energy Level Alignment and Interfacial Electronic Structures at Organic/Metal and Organic/Organic Interfaces.* Adv. Mater. **11**, 605–625 (1999).

[6] H. Vázquez Melis: *Energy level alignment at organic semiconductor interfaces.* Ph.D. thesis, Universidad Autónoma de Madrid (2006).

[7] P. Hohenberg and W. Kohn: *Inhomogeneous Electron Gas.* Phys. Rev. **136**, B864–B871 (1964).

[8] W. Kohn and L. J. Sham: *Self-Consistent Equations Including Exchange and Correlation Effects.* Phys. Rev. **140**, A1133–A1138 (1965).

[9] T. Koopmans: *Über die Zuordnung von Wellenfunktionen und Eigenwerten zu den Einzelnen Elektronen Eines Atoms.* Physica **1**, 104–113 (1934).

[10] S.-i. Machida, Y. Nakayama, S. Duhm, Q. Xin, A. Funakoshi, N. Ogawa, S. Kera, N. Ueno, and H. Ishii: *Highest-Occupied-Molecular-Orbital Band Dispersion of Rubrene Single Crystals as Observed by Angle-Resolved Ultraviolet Photoelectron Spectroscopy.* Phys. Rev. Lett. **104**, 156401 (2010).

[11] J.-L. Bredas: *Mind the gap!* Mater. Horiz. **1**, 17–19 (2014).

[12] R. Forker: *Electronic Coupling Effects and Charge Transfer between Organic Molecules and Metal Surfaces.* Ph.D. thesis, Technische Universität Dresden (2010).

[13] N. Karl: *Festkörperprobleme.* Springer-Verlag, Heidelberg (1974).

[14] A. Zangwill: *Physics at Surfaces.* Cambridge University Press, Cambridge (1988).

[15] M. Kasha, H. R. Rawls, and M. A. El-Bayoumi: *The Exciton Model in Molecular Spectroscopy.* Pure Appl. Chem. **11**, 371–392 (1965).

[16] A. F. Diaz, K. K. Kanazawa, and G. P. Gardini: *Electrochemical polymerization of pyrrole.* J. Chem. Soc., Chem. Commun. 635–636 (1979).

[17] I. G. Hill, A. Rajagopal, A. Kahn, and Y. Hu: *Molecular level alignment at organic semiconductor-metal interfaces.* Appl. Phys. Lett. **73**, 662–664 (1998).

[18] H. Vázquez, R. Oszwaldowski, P. Pou, J. Ortega, R. Pérez, F. Flores, and A. Kahn: *Dipole formation at metal/PTCDA interfaces: Role of the Charge Neutrality Level.* Europhys. Lett. **65**, 802–808 (2004).

[19] H. Vázquez, F. Flores, O. R., J. Ortega, R. Perez, and K. A.: *Barrier formation at metal-organic interfaces: dipole formation and the charge neutrality level.* Appl. Surf. Sci. **234**, 107–112 (2004).

[20] H. Vázquez, W. Gao, F. Flores, and A. Kahn: *Energy level alignment at organic heterojunctions: Role of the charge neutrality level.* Phys. Rev. B: Condens. Matter **71**, 0410306 (2005).

[21] H. Vázquez, Y. Dappe, J. Ortega, and F. Flores: *A unified model for metal/organic interfaces: IDIS, "pillow" effect and molecular permanent dipoles.* Appl. Surf. Sci. **254**, 378–382 (2007).

[22] H. Vázquez, Y. J. Dappe, J. Ortega, and F. Flores: *Energy level alignment at metal/organic semiconductor interfaces: "Pillow" effect, induced density of interface states, and charge neutrality level.* J. Chem. Phys. **126**, 144703 (2007).

[23] H. Vázquez, F. Flores, and A. Kahn: *Induced Density of States model for weakly-interacting organic semiconductor interfaces.* Org. Electron. **8**, 241–248 (2007).

[24] A. Kahn, N. Koch, and W. Gao: *Electronic structure and electrical properties of interfaces between metals and pi-conjugated molecular films.* J. Polym. Sci. Pol. Phys. **41**, 2529–2548 (2003).

[25] A. Adikaari, D. Dissanayake, and S. Silva: *Organic-Inorganic Solar Cells: Recent Developments and Outlook.* IEEE J. Sel. Top. Quant. **16**, 1595–1606 (2010).

[26] G. W. Ludwig and R. L. Watters: *Drift and Conductivity Mobility in Silicon.* Phys. Rev. **101**, 1699–1701 (1956).

[27] R. Santbergen and R. van Zolingen: *The absorption factor of crystalline silicon PV cells: A numerical and experimental study.* Sol. Energ. Mat. Sol. C. **92**, 432–444 (2008).

[28] S. M. Sze: *Physics of Semiconductor Devices.* John Wiley & Sons, New Jersey (1981).

[29] L. Ward: *Cadmium Sulphide (CdS).* In: E. D. Palik (Ed.), *Handbook of Optical Constants of Solids*, 579–595. Academic Press, Burlington (1997).

[30] A. Elschner, S. Kirchmeyer, W. Lovenich, U. Merker, and K. Reuter: *PEDOT: Principles and Applications of an Intrinsically Conductive Polymer.* Taylor & Francis, Boca Raton (2010).

[31] J.-W. Park, M. Ullah, S. Park, and C.-S. Ha: *Organic electroluminescent devices using quantum-size silver nanoparticles.* J. Mater. Sci.: Mater. Electron. **18**, 393–397 (2007).

[32] K. Itaka, M. Yamashiro, J. Yamaguchi, M. Haemori, S. Yaginuma, Y. Matsumoto, M. Kondo, and H. Koinuma: *High-Mobility C60 Field-Effect Transistors Fabricated on Molecular- Wetting Controlled Substrates.* Adv. Mater. **18**, 1713–1716 (2006).

[33] D. E. Motaung, G. F. Malgas, and C. J. Arendse: *Correlation between the morphology and photo-physical properties of P3HT:fullerene blends.* J. Mater. Sci. **45**, 3276–3283 (2010).

[34] A. J. Mozer, N. S. Sariciftci, A. Pivrikas, R. Österbacka, G. Juška, L. Brassat, and H. Bässler: *Charge carrier mobility in regioregular poly(3-hexylthiophene) probed by*

transient conductivity techniques: A comparative study. Phys. Rev. B: Condens. Matter **71**, 035214 (2005).

[35] B. Maennig, M. Pfeiffer, A. Nollau, X. Zhou, K. Leo, and P. Simon: *Controlled p-type doping of polycrystalline and amorphous organic layers: Self-consistent description of conductivity and field-effect mobility by a microscopic percolation model.* Phys. Rev. B: Condens. Matter **64**, 195208 (2001).

[36] M. Kozlik, S. Paulke, M. Gruenewald, R. Forker, and T. Fritz: *Determination of the optical constants of a- and b-zinc (II)-phthalocyanine films.* Org. Electron. **13**, 3291–3295 (2012).

[37] N. S. Sariciftci, L. Smilowitz, A. J. Heeger, and F. Wudl: *Photoinduced Electron Transfer from a Conducting Polymer to Buckminsterfullerene.* Science **27**, 1474–1476 (1992).

[38] F. S. Goucher, G. L. Pearson, M. Sparks, G. K. Teal, and W. Shockley: *Theory and Experiment for a Germanium p-n Junction.* Phys. Rev. **81**, 637–638 (1951).

[39] B. A. Gregg and M. C. Hanna: *Comparing organic to inorganic photovoltaic cells: Theory, experiment, and simulation.* J. Appl. Phys. **93**, 3605–3614 (2003).

[40] P. Würfel: *Physics of Solar Cells: From Basic Principles to Advanced Concepts.* Wiley-VCH Verlag, New Jersey (2009).

[41] K. Tennakone, G. R. R. A. Kumara, I. R. M. Kottegoda, and V. P. S. Perera: *An efficient dye-sensitized photoelectrochemical solar cell made from oxides of tin and zinc.* Chem. Commun. 15–16 (1999).

[42] K. Ramanathan, M. A. Contreras, C. L. Perkins, S. Asher, F. S. Hasoon, J. Keane, D. Young, M. Romero, W. Metzger, R. Noufi, J. Ward, and A. Duda: *Properties of 19.2% efficiency ZnO/CdS/CuInGaSe2 thin-film solar cells.* Prog. Photovoltaics Res. Appl. **11**, 225–230 (2003).

[43] I. Repins, M. A. Contreras, B. Egaas, C. DeHart, J. Scharf, C. L. Perkins, B. To, and R. Noufi: *19·9%-efficient ZnO/CdS/CuInGaSe2 solar cell with 81·2% fill factor.* Prog. Photovoltaics Res. Appl. **16**, 235–239 (2008).

[44] S. Pfuetzner, J. Meiss, A. Petrich, M. Riede, and K. Leo: *Thick C60:ZnPc bulk hetero-junction solar cells with improved performance by film deposition on heated substrates.* Appl. Phys. Lett. **94**, 253303 (2009).

[45] H. Hoppe and N. S. Sariciftci: *Organic solar cells: An overview.* J. Mater. Res. **19**, 1924–1945 (2004).

[46] L. Burtone, J. Fischer, K. Leo, and M. Riede: *Trap states in ZnPc:C60 small-molecule organic solar cells.* Phys. Rev. B: Condens. Matter **87**, 045432 (2013).

[47] U. Özgür, Y. I. Alivov, C. Liu, A. Teke, M. A. Reshchikov, S. Dogan, V. Avrutin, S.-J. Cho, and H. Morkoç: *A comprehensive review of ZnO materials and devices.* J. Appl. Phys. **98**, 041301 (2005).

[48] C. H. Peters, A. R. Guichard, A. C. Hryciw, M. L. Brongersma, and M. D. McGehee: *Energy transfer in nanowire solar cells with photon-harvesting shells.* J. Appl. Phys. **105**, 124509 (2009).

[49] A. I. Hochbaum and P. Yang: *Semiconductor Nanowires for Energy Conversion.* Chem. Rev. **110**, 527–546 (2010).

[50] S.-G. Ihn, J.-I. Song, Y.-H. Kim, J. Young Lee, and I.-H. Ahn: *Growth of GaAs Nanowires on Si Substrates Using a Molecular Beam Epitaxy.* IEEE T. Nanotechnol. **6**, 384–389 (2007).

[51] A. Mikkelsen, N. Sköld, L. Ouattara, M. Borgström, J. N. Andersen, L. Samuelson, W. Seifert, and E. Lundgren: *Direct imaging of the atomic structure inside a nanowire by scanning tunnelling microscopy.* Nat. Mater. **3**, 519–523 (2004).

[52] J. H. Zhan, X. G. Yang, S. D. Li, D. W. Wang, Y. Xie, and Y. T. Qian: *A chemical solution transport mechanism for one-dimensional growth of CdS nanowires.* J. Cryst. Growth **220**, 231–234 (2000).

[53] C. Borchers, S. Müller, D. Stichtenoth, D. Schwen, and C. Ronning: *Catalyst Nanostructure Interaction in the Growth of 1-D ZnO Nanostructures.* J. Phys. Chem. B **110**, 1656–1660 (2006).

[54] R. S. Wagner and W. C. Ellis: *Vapor-Liquid-Solid Mechanism of Single Crystal Growth.* Appl. Phys. Lett. **4**, 89–90 (1964).

[55] J. Wang, J. Sha, Q. Yang, X. Ma, H. Zhang, J. Yu, and D. Yang: *Carbon-assisted synthesis of aligned ZnO nanowires.* Mater. Lett. **59**, 2710–2714 (2005).

[56] H. Park, Y. Shi, and J. Kong: *Application of solvent modified PEDOT:PSS to graphene electrodes in organic solar cells.* Nanoscale **5**, 8934–9 (2013).

[57] S. Shao, J. Liu, J. Bergqvist, S. Shi, C. Veit, U. Würfel, Z. Xie, and F. Zhang: *In Situ Formation of MoO3 in PEDOT:PSS Matrix: A Facile Way to Produce a Smooth and Less Hygroscopic Hole Transport Layer for Highly Stable Polymer Bulk Heterojunction Solar Cells.* Adv. Energy Mater. **3**, 349–355 (2013).

[58] F. J. Lim, K. Ananthanarayanan, J. Luther, and G. W. Ho: *Influence of a novel fluorosurfactant modified PEDOT:PSS hole transport layer on the performance of inverted organic solar cells.* J. Mater. Chem. **22**, 25057–25064 (2012).

[59] L. Reimer: *Scanning Electron Microscopy: Physics of Image Formation and Microanalysis.* Springer-Verlag, Heidelberg (1998).

[60] S. Amelinckx, D. van Dyck, J. van Landuyt, and G. van Tendeloo (Eds.): *Electron Microscopy: Principles and Fundamentals.* VCH Verlagsgesellschaft mbH, Weinheim (1997).

[61] J. Bardeen: *Tunneling from a many-particle point of view.* Phys. Rev. Lett. **6**, 57–59 (1961).

[62] J. Tersoff and D. R. Hamann: *Theory and Application for the Scanning Tunneling Microscope.* Phys. Rev. Lett. **50**, 1998–2001 (1983).

[63] V. A. Ukraintsev: *Data evaluation technique for electron-tunneling spectroscopy.* Phys. Rev. B: Condens. Matter **53**, 11176–11185 (1996).

[64] R. Feenstra, J. A. Stroscio, and A. Fein: *Tunneling spectroscopy of the Si(111)2 x 1 surface.* Surf. Sci. **181**, 295–306 (1987).

[65] G. Binnig, C. F. Quate, and C. h. Gerber: *Atomic Force Microscope.* Phys. Rev. Lett. **56**, 930–933 (1986).

[66] S. Hüfner: *Photoelectron Spectroscopy.* Springer-Verlag, Heidelberg (2003).

[67] M. Schädel, J. Isenberg, J. Suthues, C. Ballif, and G. Gobsch: *Improving Quantum Efficiency Measurement In Large Area Solar Cells By Using Appropriate Bias Illumination.*

[68] D. J. Wehenkel, K. H. Hendriks, M. M. Wienk, and R. A. Janssen: *The effect of bias light on the spectral responsivity of organic solar cells.* Org. Electron. **13**, 3284 – 3290 (2012).

[69] A. Ogunsipe and T. Nyokong: *Effects of substituents and solvents on the photochemical properties of zinc phthalocyanine complexes and their protonated derivatives.* J. Mol. Struct. **689**, 89–97 (2004).

[70] N. L. Tran, F. I. Bohrer, W. C. Trogler, and A. C. Kummel: *A density functional theory study of the correlation between analyte basicity, ZnPc adsorption strength, and sensor response.* J. Chem. Phys. **130**, 204307 (2009).

[71] C. Ingrosso, A. Petrella, M. L. Curri, M. Striccoli, P. Cosma, C. P. D., and A. Agostiano: *Photoelectrochemical properties of hybrid junctions based on zinc phthalocyanine and semiconducting colloidal nanocrystals.* Electrochim. Acta **51**, 5120–5124 (2006).

[72] Y. A. Mikheev, L. N. Guseva, and Y. A. Ershov: *Vibronic Spectra of Solutions and Sols of Copper Phthalocyanine.* Russ. J. Phys. Chem. A **81**, 617–625 (2007).

[73] G. A. Kumar, J. Thomas, N. V. Unnikrishnan, V. P. N. Nampoori, and C. P. G. Vallabhan: *Optical absorption and emission spectral studies of phthalocyanine molecules in DMF.* J. Porphyr. Phthalocya. **5**, 456–459 (2001).

[74] M. Wojdyla, B. Derkowska, Z. Lukasiak, and W. Bala: *Absorption and photoreflectance spectroscopy of zinc phthalocyanine (ZnPc) thin films grown by thermal evaporation.* Mater. Lett. **60**, 3441–3446 (2006).

[75] R. Hiesgen, M. Räbisch, H. Böttcher, and D. Meissner: *STM investigation of the growth structure of Cu-phthalocyanine films with submolecular resolution.* Sol. Energ. Mat. Sol. C. **61**, 73–85 (2000).

[76] K. Wihksne and A. E. Newkirk: *Electrical Conductivities of alpha- and beta-Phthalocyanine.* J. Chem. Phys. **34**, 2184–2185 (1961).

[77] S. Kment, P. Kluson, M. Drobek, R. Kuzel, I. Gregora, M. Kohout, and Z. Hubicka: *Preparation of thin phthalocyanine layers and their structural and absorption properties.* Thin Solid Films **517**, 5274–5279 (2009).

[78] V. Coropceanu, J. Cornil, D. A. da Silva Filho, Y. Olivier, R. Silbey, and J.-L. Brédas: *Charge Transport in Organic Semiconductors.* Chem. Rev. **107**, 926–952 (2007).

[79] M. El-Nahass, H. Zeyada, M. Aziz, and N. El-Ghamaz: *Structural and optical properties of thermally evaporated zinc phthalocyanine thin films.* Opt. Mater. **27**, 491–498 (2004).

[80] S. Senthilarasu, R. Sathyamoorthy, S. Lalitha, A. Subbarayan, and N. K.: *Thermally evaporated ZnPc thin filmsband gap dependence on thickness.* Sol. Energ. Mat. Sol. C. **82**, 179–186 (2004).

[81] F. W. Karasek and J. C. Decius: *Observations Concerning Polymorphic Crystalline Modifications of the Phthalocyanines1.* J. Am. Chem. Soc. **74**, 4716–4717 (1952).

[82] H. L. Schläfer and O. Kling: *Bedeutung isosbestischer Punkte für die spektrophotometrische Untersuchung chemischer Zeitreaktionen und Gleichgewichte.* Angew. Chem. **68**, 667–670 (1956).

[83] M. Kozlik, S. Paulke, M. Gruenewald, R. Forker, and T. Fritz: *Optical Constants of α-and β-Zinc(II)-Phthalocyanine Films.* Dataset Papers in Physics **2013**, 926470 (2013).

[84] C. C. Katsidis and D. I. Siapkas: *General Transfer-Matrix Method for Optical Multilayer Systems with Coherent, Partially Coherent, and Incoherent Interference.* Appl. Opt. **41**, 3978–3987 (2002).

[85] H. Proehl, R. Nitsche, T. Dienel, K. Leo, and T. Fritz: *In situ differential reflectance spectroscopy of thin crystalline films of PTCDA on different substrates.* Phys. Rev. B: Condens. Matter **71**, 165207 (2005).

[86] R. Forker and T. Fritz: *Optical differential reflectance spectroscopy of ultrathin epitaxial organic films.* Phys. Chem. Chem. Phys. **11**, 2142–2155 (2009).

[87] R. Forker, M. Gruenewald, and T. Fritz: *Optical differential reflectance spectroscopy on thin molecular films.* Annu. Rep. Prog. Chem., Sect. C: Phys. Chem. **108**, 34–68 (2012).

[88] E. Centurioni: *Generalized matrix method for calculation of internal light energy flux in mixed coherent and incoherent multilayers.* Appl. Opt. **44**, 7532–7539 (2005).

[89] T. Fritz, J. Hahn, and H. Böttcher: *Determination of the optical constants of evaporated dye layers.* Thin Solid Films **170**, 249–257 (1989).

[90] R. Nitsche and T. Fritz: *Precise Determination of the Complex Optical Constant of Mica.* Appl. Opt. **43**, 3263–3270 (2004).

[91] C. Schuenemann, C. Elschner, A. Levin, M. Levichkova, K. Leo, and M. Riede: *Zinc phthalocyanine - Influence of substrate temperature, film thickness, and kind of substrate on the morphology.* Thin Solid Films **519**, 3939–3945 (2011).

[92] R. Nitsche and T. Fritz: *Determination of model-free Kramers-Kronig consistent optical constants of thin absorbing films from just one spectral measurement: Application to organic semiconductors.* Phys. Rev. B: Condens. Matter **70**, 195432 (2004).

[93] S. Senthilarasu and R. Sathyamoorthy: *Effect of substrate temperature on the optical constants of zincphthalocyanine thin films.* Cryst. Res. Technol. **41**, 1136–1141 (2006).

[94] A. B. Djurisic, C. Y. Kwong, T. W. Lau, W. L. Guo, E. H. Li, Z. T. Liu, H. S. Kwok, L. S. M. Lam, and W. K. Chan: *Optical properties of copper phthalocyanine.* Opt. Commun. **205**, 155–162 (2002).

[95] C. Gueymard: *SMARTS2, A Simple Model of the Atmospheric Radiative Transfer of Sunshine.* Florida Solar energy Center, Cocoa (1995).

[96] H. R. Kerp and E. E. van Faassen: *Oxygen doping in zinc phthalocyanine layers for photovoltaic applications.* Proc. SPIE **4108**, 62–75 (2001).

[97] A. Janotti and C. G. Van de Walle: *Fundamentals of zinc oxide as a semiconductor.* Rep. Prog. Phys. **72**, 126501 (2009).

[98] V. Coropceanu, H. Li, P. Winget, L. Zhu, and J.-L. Brédas: *Electronic-Structure Theory of Organic Semiconductors: Charge-Transport Parameters and Metal/Organic Interfaces.* Annu. Rev. Mater. Res. **43**, 63–87 (2013).

[99] M. G. Harrison, J. Gruener, and G. C. W. Spencer: *Analysis of the photocurrent action spectra of MEH-PPV polymer photodiodes.* Phys. Rev. B: Condens. Matter **55**, 7831–7849 (1997).

[100] J. Wagner, T. Fritz, and H. Boettcher: *Computer Modelling of Organic Thin Film Solar Cells. I. Exciton Model of Photocurrent Generation.* Phys. Status Solidi A **136**, 423–432 (1993).

[101] Y. Terao, H. Sasabe, and C. Adachi: *Correlation of hole mobility, exciton diffusion length, and solar cell characteristics in phthalocyanine/fullerene organic solar cells.* Appl. Phys. Lett. **90**, 103515 (2007).

[102] D. Ray, E. Furno, Mauroand Siebert-Henze, K. Leo, and M. Riede: *Quantitative estimation of electronic quality of zinc phthalocyanine thin films.* Phys. Rev. B: Condens. Matter **84**, 075214 (2011).

[103] H. R. Kerp, H. Donker, R. B. M. Koehorst, T. J. Schaafsma, and E. E. van Faassen: *Exciton transport in organic dye layers for photovoltaic applications.* Chem. Phys. Lett. **298**, 302–308 (1998).

[104] S. Athanasopoulos, E. V. Emelianova, A. B. Walker, and D. Beljonne: *Exciton diffusion in energetically disordered organic materials.* Phys. Rev. B: Condens. Matter **80**, 195209 (2009).

[105] C. Wagner, R. Franke, and T. Fritz: *Evaluation of $I(V)$ curves in scanning tunneling spectroscopy of organic nanolayers.* Phys. Rev. B: Condens. Matter **75**, 235432 (2007).

[106] J. Hillbrand and R. D. Gold: *Determination of the impurity distribution in junction diodes from capacitance-voltage measurements.* RCA Rev. **21**, 245–52 (1960).

[107] W. C. Johnson and P. T. Panousis: *The Influence of Debye Length on the C-v Measurement of Doping Profiles.* IEEE T. Electron. Dev. **18**, 965–973 (1971).

[108] G. H. Glover: *Determination of Deep Levels in Semiconductors from C-V Measurements.* IEEE T. Electron. Dev. **19**, 138–143 (1972).

[109] J. Hwang, A. Wan, and A. Kahn: *Energetics of metal-organic interfaces: New experiments and assessment of the field.* Mater. Sci. Eng., R **64**, 1–31 (2009).

[110] K. Ihm, H.-E. Heo, S. Chung, J.-R. Ahn, J. H. Kim, and T.-H. Kang: *Odd characteristics of Au film on pentacene.* Appl. Phys. Lett. **90**, 242111 (2007).

[111] B. Jaeckel, J. B. Sambur, and B. A. Parkinson: *Ubiquitous Pentacene Monolayer on Metals Deposited onto Pentacene Films.* Langmuir **23**, 11366–11368 (2007).

[112] S. Scholz, Q. Huang, M. Thomschke, S. Olthof, P. Sebastian, K. Walzer, K. Leo, S. Oswald, C. Corten, and D. Kuckling: *Self-doping and partial oxidation of metal-on-organic interfaces for organic semiconductor devices studied by chemical analysis techniques.* J. Appl. Phys. **104**, 104502 (2008).

[113] G. Chiarotti (Ed.): *Electronic and Vibrational Properties.* Springer-Verlag, Heidelberg (1994).

[114] J. Blochwitz, T. Fritz, M. Pfeiffer, K. Leo, D. M. Alloway, P. A. Lee, and N. R. Armstrong: *Doped organic semiconductors: Physics and application in light emitting diodes.* Org. Electron. **2**, 97–104 (2001).

[115] W. Gao and A. Kahn: *Electronic structure and current injection in zinc phthalocyanine doped with tetrafluorotetracyanoquinodimethane: Interface versus bulk effects.* Org. Electron. **3**, 53–63 (2002).

[116] G. Ricciardi, A. Rosa, and E. J. Baerends: *Ground and Excited States of Zinc Phthalocyanine Studied by Density Functional Methods.* J. Phys. Chem. A **105**, 5242–5254 (2001).

[117] G. Garcia-Belmonte and J. Bisquert: *Open-circuit voltage limit caused by recombination through tail states in bulk heterojunction polymer-fullerene solar cells.* Appl. Phys. Lett. **96**, 113301 (2010).

[118] D. Veldman, S. C. J. Meskers, and R. A. J. Janssen: *The Energy of Charge-Transfer States in Electron Donor-Acceptor Blends: Insight into the Energy Losses in Organic Solar Cells.* Adv. Funct. Mater. **19**, 1939–1948 (2009).

[119] H. Vazquez and A. Troisi: *Calculation of rates of exciton dissociation into hot charge-transfer states in model organic photovoltaic interfaces.* Phys. Rev. B: Condens. Matter **88**, 205304 (2013).

[120] X.-Y. Zhu, Q. Yang, and M. Muntwiler: *Charge-Transfer Excitons at Organic Semiconductor Surfaces and Interfaces.* Acc. Chem. Res. **42**, 1779–1787 (2009).

[121] H. Tamura and I. Burghardt: *Ultrafast Charge Separation in Organic Photovoltaics Enhanced by Charge Delocalization and Vibronically Hot Exciton Dissociation.* J. Am. Chem. Soc. **135**, 16364–13637 (2013).

[122] H. Tamura, I. Burghardt, and M. Tsukada: *Exciton Dissociation at Thiophene/Fullerene Interfaces: The Electronic Structures and Quantum Dynamics.* J. Phys. Chem. C **115**, 10205–10210 (2011).

[123] A. Petersen, A. Ojala, T. Kirchartz, T. A. Wagner, F. Würthner, and U. Rau: *Field-dependent exciton dissociation in organic heterojunction solar cells.* Phys. Rev. B: Condens. Matter **85**, 245208 (2012).

[124] K. Feron, W. J. Belcher, C. J. Fell, and P. C. Dastoor: *Organic Solar Cells: Understanding the Role of Förster Resonance Energy Transfer.* Int. J. Mol. Sci. **13**, 17019–17047 (2012).

[125] A. A. Bakulin, A. Rao, V. G. Pavelyev, P. H. M. van Loosdrecht, M. S. Pshenichnikov, D. Niedzialek, J. Cornil, D. Beljonne, and R. H. Friend: *The Role of Driving Energy and Delocalized States for Charge Separation in Organic Semiconductors.* Science **335**, 1340–1344 (2012).

[126] M. Pfeiffer, A. Beyer, B. Plönnigs, A. Nollau, T. Fritz, K. Leo, D. Schlettwein, S. Hiller, and D. Wöhrle: *Controlled p-doping of pigment layers by cosublimation: Basic mechanisms and implications for their use in organic photovoltaic cells.* Sol. Energ. Mat. Sol. C. **63**, 83–99 (2000).

[127] M. Pfeiffer, K. Leo, X. Zhou, J. Huang, M. Hofmann, A. Werner, and J. Blochwitz-Nimoth: *Doped organic semiconductors: Physics and application in light emitting diodes.* Org. Electron. **4**, 89–103 (2003).

[128] D. A. Shirley: *High-Resolution X-Ray Photoemission Spectrum of the Valence Bands of Gold.* Phys. Rev. B: Condens. Matter **5**, 4709–4714 (1972).

[129] C. D. Wagner: *Handbook of x-ray photoelectron spectroscopy: a reference book of standard data for use in x-ray photoelectron spectroscopy.* Physical Electronics Division, Perkin-Elmer Corp., Eden Prairie (1979).

[130] R. A. Serway: *Principles of Physics.* Saunders College Publishing, London (1998).

[131] T. K. Roy, D. Sanyal, D. Bhowmick, and A. Chakrabarti: *Temperature dependent resistivity study on zinc oxide and the role of defects.* Mater. Sci. Semicond. Process. **16**, 332–336 (2013).

[132] A. F. i Morral: *Semiconductor nanowires: single photon emission and next generation photovoltaics.* talk at the seminar of the Institute of Solid State Physics (2013).

LIST OF FIGURES

LIST OF TABLES

PUBLICATIONS

Many substantial aspects of this dissertation have been published in peer-reviewed scientific journals and/or presented at international conferences. In the following, all hitherto realized contributions are listed chronologically.

Articles

A1 M. Kozlik, S. Paulke, M. Gruenewald, R. Forker, and T. Fritz : *Determination of the optical constants of α- and β-zinc (II)-phthalocyanine films.* Org. Electron. **13**, 3291-3295 (2012).
DOI:10.1016/j.orgel.2012.09.030

A2 M. Kozlik, S. Paulke, M. Gruenewald, R. Forker, and T. Fritz : *Optical Constants of α- and β-Zinc(II)-Phthalocyanine Films.* Dataset Papers in Physics **2013**, Article ID 926470, 5 pages (2013).
DOI:10.1155/2013/926470

A3 M. Gruenewald, K. Wachter, M. Meissner, M. Kozlik, R. Forker, and T. Fritz : *Optical and electronic interaction at metal-organic and organic-organic interfaces of ultra-thin layers of PTCDA and SnPc on noble metal surfaces.* Org. Electron. **14**, 2177-2183 (2013).
DOI:10.1016/j.orgel.2013.05.010

Talks

T1 M. Kozlik*, R. Forker, S. Paulke, C. Ronning, and T. Fritz : *Combination of Zinc Phthalocyanines and Zinc Oxide for Hybrid Solar Cells.* DPG Frühjahrstagung, 26–31 March 2012 in Berlin, Germany.

T2 M. Kozlik*, S. Paulke, M. Gruenewald, R. Forker, and T. Fritz : *Optoelectronic Properties Of Zinc(II)-Phthalocyanine.* DPG Frühjahrstagung, 10–15 March 2013 in Regensburg, Germany.

T3 M. Kozlik*, M. Gruenewald, S. Paulke, R. Forker, C. Ronning, and T. Fritz : *Hybrid Solar Cells made of Phthalocyanines and Zinc Oxide Nanowires.* Hybrid-Photovoltaics, 15–17 May 2013 in Berlin, Germany.

T4 M. Kozlik*, S. Paulke, M. Gruenewald, R. Forker, and T. Fritz : *Optoelectronic Properties Of Zinc(II)-Phthalocyanine.* IVC-19, 9–13 September 2013 in Paris, Germany.

Posters

P1 M. Kozlik*, S. Milz, S. Möller, C. Ronning, and T. Fritz : *Combination of Zinc-Phthalocyanine and Zinc Oxide for Functional Hybrid Materials.* Second International Conference on Multifunctional, Hybrid and Nanomaterials, 06–10 March 2011 in Strasbourg, France.

P2 M. Kozlik*, S. Milz, S. Möller, C. Ronning, and T. Fritz : *Hybrid Solar Cells made of Zinc Phthalocyanine and Zinc Oxide Nanowires.* DPG Frühjahrstagung, 13–18 March 2011 in Dresden, Germany.

P3 M. Kozlik*, R. Forker, A. Donat, S. Paulke, C. Ronning, and T. Fritz : *Zinc Phthalocyanine in Hybrid Solar Cells with Zinc Oxide Nanowires.* Next Generation Solar Energy, 12–14 December 2011 in Erlangen, Germany.

DANKSAGUNG

CURRICULUM VITAE

Name	Michael Kozlik
Geburtsdatum	10.08.1984
Geburtsort	Gera

Bildungsweg

1991 − 1995	Staatl. Grundschule 12 Gera
1995 − 2003	Osterlandgymnasium Gera
2003	Abitur
2004 − 2010	Studium der Physik an der Friedrich-Schiller-Universität Jena
2007 − 2008	Auslandsstudium an der Linköping Universität, Schweden
2008 − 2009	Diplomarbeit zum Thema Halbleiternanodrähte für die Photonik
2009	Abschluss des Studiums an der Friedrich-Schiller-Universität Jena als Diplom-Physiker
2010 − 2014	Wissenschaftlicher Mitarbeiter am Institut für Festkörperphysik der Friedrich-Schiller-Universität Jena mit dem Ziel der Promotion

Jena, den 23.07.2014

_____
Michael Kozlik

ERKLÄRUNG

Ich erkläre hiermit ehrenwörtlich, dass ich die vorliegende Arbeit selbstständig, ohne unzulässige Hilfe Dritter und ohne Benutzung anderer als der angegebenen Hilfsmittel und Literatur angefertigt habe. Die aus anderen Quellen direkt oder indirekt übernommenen Daten und Konzepte sind unter Angabe der Quelle gekennzeichnet

Bei der Auswahl und Auswertung folgenden Materials habeen mir die nachstehend aufgeführten Personen in der jeweils beschriebenen Weise unentgeltlich geholfen:

1. Einige der ZnO-NW Proben wurden von Matthias Ogrisek und Andreas Johannes synthetisiert.

2. Einige planare Proben mit ZnPc Schichten wurden von Sören Paulke, Joseph Olson, Alexwy Gavrik, Martin Gebhardt und Alexander Kusch präpariert.

3. Die Löslichkeit von ZnPc in verschiedenen Lösungsmitteln wurde in Zusammenarbeit mit Sören Paulke und Martin Hager bestimmt.

4. Photoluminescence Spektren wurden von Sebastian Geburt und Robert Röder gemessen.

5. Die Leitfähigkeit der Gläser mit TCO wurde im Rahmen der Bachelorarbeit von Sven Möller ermittelt.

6. Zur Bestimmung der optischen Konstanten trugen maßgeblich Marco Grünewald und Sören Paulke bei.

7. Raumtemperatur-AFM Aufnahmen wurden von Marco Grünewald und Silke Frunzke gemessen.

8. Die Photoelektronenspektren wurden mit Helga Rudolph gemessen.

9. Die Anlage zum Aufdampfen von ZnPc Schcihten, B30, wurde mit Stefan Prass, Uwe Eberhardt und Martin Gebhardt umgebaut.

10. Untersuchungen zum Benetzungsverhalten von PEDOT mit Netzmittel wurden im Rahmen einer Bachelorarbeit von Martin Heilemann durchgeführt.

11. Der Teilchenbeschleuniger $JULIA$, welcher für RBS-Messungen genutzt wurde, wird betrieben von Ulrich Barth.

12. Dektak Höhenprofile wurden mit Carmen Voigt aufgenommen.

13. Im Übrigen waren jeweils die Koautoren der angeführten Veröffentlichungen (siehe Anhang Publications) an der Interpretation der Ergebnisse beteiligt.

Weitere Personen waren an der inhaltlich-materiellen Erstellung der vorliegenden Arbeiut nicht beteiligt. Insbesondere habe ich hierfür nicht die entgeltliche Hilfe von Vermittlungs- bzw. Beratungsdiensten (Promotionsberater oder andere Personen) in Anspruch genommen. Niemand hat von mir unmittelbar oder mittelbar geldwerte Leistungen für Arbeiten erhalten, die im Zusammenhang mit dem Inhalt der vorgelegten Dissertation stehen.

Die Arbeit wurde bisher weder im In- noch im Ausland in gleicher oder ähnlicher Form einer anderen Prüfungsbehörde vorgelegt.

Die geltende Promotionsordnung der Physikalisch-Astronomischen Fakultät ist mir bekannt.

Ich versicher ehrenwörtlich, dass ich nach bestem Wissen die reine Wahrheit gesagt und nichts verschwiegen habe.

Jena, den 23.07.2014

_____

Michael Kozlik